

4000110477/14/NL/FF/lf

Technical Support for the 2014 SMOSice Campaign in SE Svalbard



SMOSice 2014

Final Report

[Alfred-Wegener-Institut](#)

Stefan Hendricks
Daniel Steinhage
Veit Helm
Gerit Birnbaum

[DTU Space](#)

Niels Skou
Steen Savstrup Kristensen
Sten Schmidl Søbjærg

[Norwegian Polar Institute](#)

Sebastian Gerland
Gunnar Spreen
Marius Bratrein
Jennifer King

[Universität Hamburg](#)

Lars Kaleschke

Project: Technical Support for the 2014 SMOSice Campaign in SE Svalbard

ESA Contract Number: 4000110477/14/NL/FF/If

Final Report, 2015

Authors

S. Hendricks¹, D. Steinhage¹, V. Helm¹, G. Birnbaum¹, N. Skou², S. S. Kristensen²,
S. S. Søbjærg², S. Gerland³, G. Spreen³, M. Bratrein³, J. King³, L Kaleschke⁴

¹ Alfred Wegener Institute, Bremerhaven, Germany

² Technical University of Denmark, Danish National Space Center, Copenhagen, Denmark

³ Norwegian Polar Institute, Tromsoe, Norway

⁴ Universität Hamburg, Hamburg, Germany

Contact

Stefan Hendricks

Alfred Wegener Institute für Polar und Meeresforschung

Bussestr. 24, 27570 Bremerhaven

Germany

+49 471 4831 1874

Stefan.Hendricks@awi.de

DISTRIBUTION LIST

Name	Organization	Issue	Date
Tânia Casal	ESA		
Stefan Hendricks	AWI		
Lars Kaleschke	Universität Hamburg		
Gunnar Spreen	NPI		
Sebastian Gerland	NPI		
Niels Skou	DTU-Space		
Steen Savstrup Kristensen	DTU-Space		
Jan Balling	DTU-Space		
Sten Schmidl Søbjærg	DTU-Space		

DOCUMENT CONTROL DATA

Issue	Revision	Date	Description
1	0	2015/05/18	Submitted version

Table of Contents

1	Introduction	6
2	Campaign Overview	8
2.1	Polar-5 Instrumentation	13
	EMIRAD	13
	Airborne Laserscanner	14
	Snow Radar	14
	Radiation and Surface temperature	14
	Aerial Photography.....	15
2.2	Helicopter EM-Bird	15
3	Data Processing Steps.....	16
3.1	EMIRAD	16
	Calibration theory and procedure	16
	Internal calibration	19
	External calibration, microwave cables.....	21
	External calibration, antenna system	22
	Attitude parameter determination and corrections	24
	Statistical RFI analysis and mitigation	25
	Data integration	28
	Mitigation of special on-board CW type RFI.....	28
	Data validation using internal ACL and wing wags	31
	Liquid Nitrogen calibrations	32
	Presentation of delivered data set	32
3.2	Airborne Laser Scanner	37
	Instrument mounting position	37
	Ellipsoidal surface height.....	38
	Sea Surface Height Classification	38
	Laser Freeboard.....	40
3.3	Snow Radar	43
	Runway Calibration	43
	Sea Ice Example	45
3.4	Airborne EM	46
3.5	Auxiliary Aircraft Sensors	50
	KT19 surface temperature.....	50
	Radiation Sensors	50
	Aerial Photography.....	50

4	Preliminary Results	51
4.1	ALS and SMOS thickness	51
4.2	ALS and EMIRAD thickness.....	53
4.3	EMIRAD and SMOS brightness temperatures.....	56
5	Summary.....	57
6	Acknowledgements	57
7	References.....	58
8	Data Inventory.....	60
8.1	Data Structure	60
8.2	EMIRAD	60
	Data format	61
8.3	Laser Scanner.....	62
	Swath files.....	62
	Software.....	63
	Resampled data	63
8.4	KT19	64
8.5	Radiometer	64
8.6	EM-Bird	65
8.7	Aerial Nadir Images.....	65
9	EMIRAD Instrument validation flights	66
9.1	Instrument validation flight, Svalbard.....	66
9.2	Navigation data	68
10	ALS Freeboard Profiles	69
11	File Inventory.....	80
11.1	Flight ID 20140323_01	80
11.2	Flight ID 20140324_01	81
11.3	Flight ID 20140326_01	82
11.4	Flight ID 20140326_02	83

1 Introduction

The ESA SMOSice study (Contract number: 4000101476/10/NL/CT) has demonstrated for the first time the potential to retrieve sea ice thickness from SMOS data. It was therefore the aim of the 2014 SMOSice campaign to improve the SMOS sea-ice thickness retrieval algorithm by assembling a comprehensive data set of high resolution L-Band radiometer data, auxiliary sea ice conditions and sea-ice thickness validation data. The surveys were centered on newly formed thin sea ice regimes in the Barents Sea south-east of the Svalbard in spring 2014.

The objectives for the analysis of the campaign data are the assessment of biases and uncertainties of the low resolution L-Band brightness temperatures of SMOS with high resolution information and the validation and optimization of sea-ice thickness retrieval algorithms with coincident direct measurements of sea-ice thickness. It was therefore the goal of the SMOSice 2014 field campaign to collect the following datasets:

1. High resolution, polarized L-Band brightness temperatures at different incident angles to assess spatial variability
2. Estimations of snow-depth to estimate the effect of the snow layer on brightness temperatures
3. Independent sea-ice thickness measurements for the validation of retrieval algorithms.
4. Auxiliary datasets as input for retrieval algorithms and characterization of surface properties (surface temperature, longwave and shortwave radiative fluxes and freeboard/surface roughness)

To obtain coincident datasets of these parameters, two sensor platforms were used. The polar research aircraft "Polar-5" of the Alfred Wegener Institute operated from the airport in Longyearbyen, Spitsbergen and a helicopter surveyed the sea ice from the Norwegian research vessel Lance. The voyage of RV Lance was funded and organized by the University of Hamburg in the framework of the German Ice Route Optimization Project (IRO-2), led by the Hamburg Ship Model Basin (HSVA) and funded by the German Federal Ministry for Economic Affairs and Energy (BMWi).

The combination and coordination of the two sensor platforms at different flight levels allowed the acquisition of a unique datasets consisting of coincident measurements of all relevant parameters for thin-ice thickness retrieval with SMOS. Polar-5 was equipped with EMIRAD-2, an airborne L-Band radiometer from DTU-Space, a radar system dedicated for snow depth estimation, a linear-swath type laser scanner, infrared pyrometer to estimate sea ice surface temperatures and radiation sensors. The helicopter towed an EM-Bird, operated by personnel of the Norwegian Polar Institute (NPI), to measure the sum of ice and snow thickness.

The data qualities of the collected datasets were checked and with the exception of the radar, geophysical data products were generated from all sensors as described in this report. The preliminary analysis of the campaign data allowed the analysis of the skill of L-Band sea-ice thickness retrieval by investigating

- the variability of sea-ice thickness at high resolution with collocated aircraft EMIRAD radiometer data and sea-ice thickness estimated from laser scanner freeboard
- the regional distribution at 100 km scale by using SMOS radiometer data and sea-ice thickness data from the EM-Bird
- potential biases between EMIRAD-2 and SMOS radiometer data

The purpose of this document is therefore description of the data processing steps that have led to the preliminary data analysis and the listing of the final data products that have been generated from the SMOSice 2014 campaign data. The document is built on the Data Acquisition Report, but gives redundant information where necessary for the benefit of the reader.

The content of the document is therefore structured in the following parts:

1. Brief overview of the field campaign
2. Description of instrumentation
3. Data processing and validation
4. Preliminary Analysis of EMIRAD, SMOS and ALS data
5. Technical data description of final products
6. Summary

The appendix contains over a listing of the files of the final data delivery as well as overview maps of the ALS freeboard data.

2 Campaign Overview



Figure 1: Left: Polar-5 research aircraft at the airport in Longyearbyen, Spitsbergen, Right: RV Lance with Survey Helicopter

The following tables and figures give a short overview of the

- sensor inventory of the research platforms (Table 1, Paragraphs 2.1 and 2.2)
- the timeline of the surveys and their naming conventions (Table 2)
- the location of the surveys (Figure 2 - Figure 6)

For a full description please refer to the data acquisition report (Hendricks et al., 2014)

Table 1: Overview of observables during the 2014 SMOSice field campaign

Platform	Sensor	Observable
Polar-5	EMIRAD-2	L-Band brightness temperatures <ul style="list-style-type: none"> • horizontal and vertical polarizations • Nadir and higher incidence angles
Lance Helicopter	Airborne EM (EM-Bird)	Sea-Ice Thickness
Polar-5	Airborne Laserscanner	Freeboard, Surface Roughness
Polar-5	Airborne Snow Radar	Snow Depth (experimental, no geophysical product)
Polar-5	KT19	Surface Temperature
Polar-5	Pyrgeometer/Pyranometer	Up/Downwelling longwave/shortwave radiation
Polar-5	Photo Camera	Visual impression of sea-ice conditions
Lance	Ship EM	Sea-Ice Thickness (data courtesy of IRO-2 project, L. Kaleschke)

Table 2: Activities of 2014 SMOSice field campaign

Date	Activity	Flight Objective	Flight ID
17.03.2014	Start of RV Lance cruise		
19.03.2014	Helicopter Science Flight	Science Flight	20149319_f1
20.03.2014	Helicopter Science Flight	Science Flight	20149320_f2
	Helicopter Science Flight	Science Flight	20149320_f3
21.03.2014	LYR Team Arrival		
22.03.2014	Polar-5 Integration		
	Helicopter Science Flight	Science Flight	20140322_f4
	Helicopter Science Flight	Science Flight	20140322_f5
23.03.2014	Polar-5 Science Flight	Instrument verification	20140323_01
	Helicopter Science Flight	Science Flight	20140323_f6
24.03.2014	Polar-5 Science Flight	Polar-5 – Helicopter	20140324_01
	Helicopter Science Flight	Helicopter – Polar-5	20140324_f7
25.03.2014	Weather Day		
26.03.2014	Polar-5 Science Flight	Polar-5 – Helicopter	20140326_01
	Helicopter Science Flight	Helicopter – Polar-5	20140326_f8
	Polar-5 Science Flight	CryoSat-2 Track	20140326_02
27.03.2014	Weather Day		
28.03.2014	LYR Team Departure		
29.03.2014	End of RV Lance Cruise		

SMOSice2014 - 2014/03/23 - Instrument Test

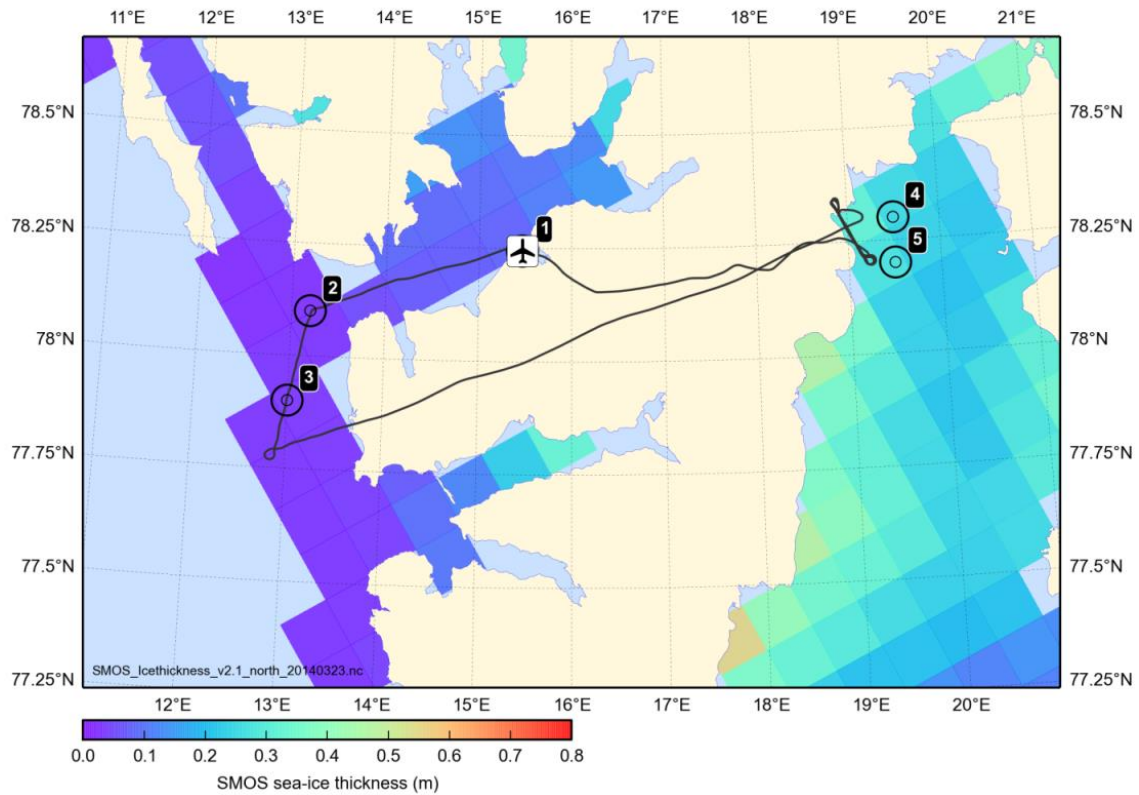


Figure 2: Waypoints and flight track of survey 20140323_01

SMOSice2014 - 2014/03/24 - Science Mission - Lance Helicopter #1

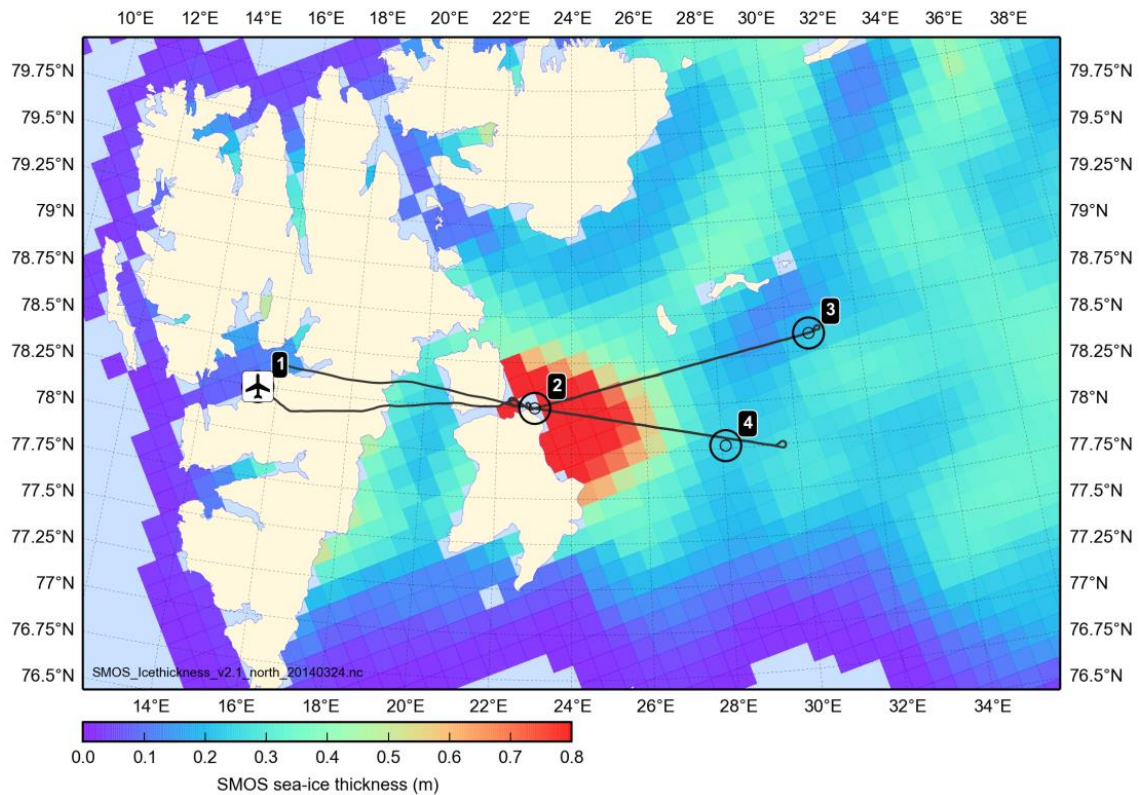


Figure 3: Waypoints and flight track of survey 20140324_01

SMOSice2014 - 2014/03/26 - Science Mission - Lance Helicopter #2

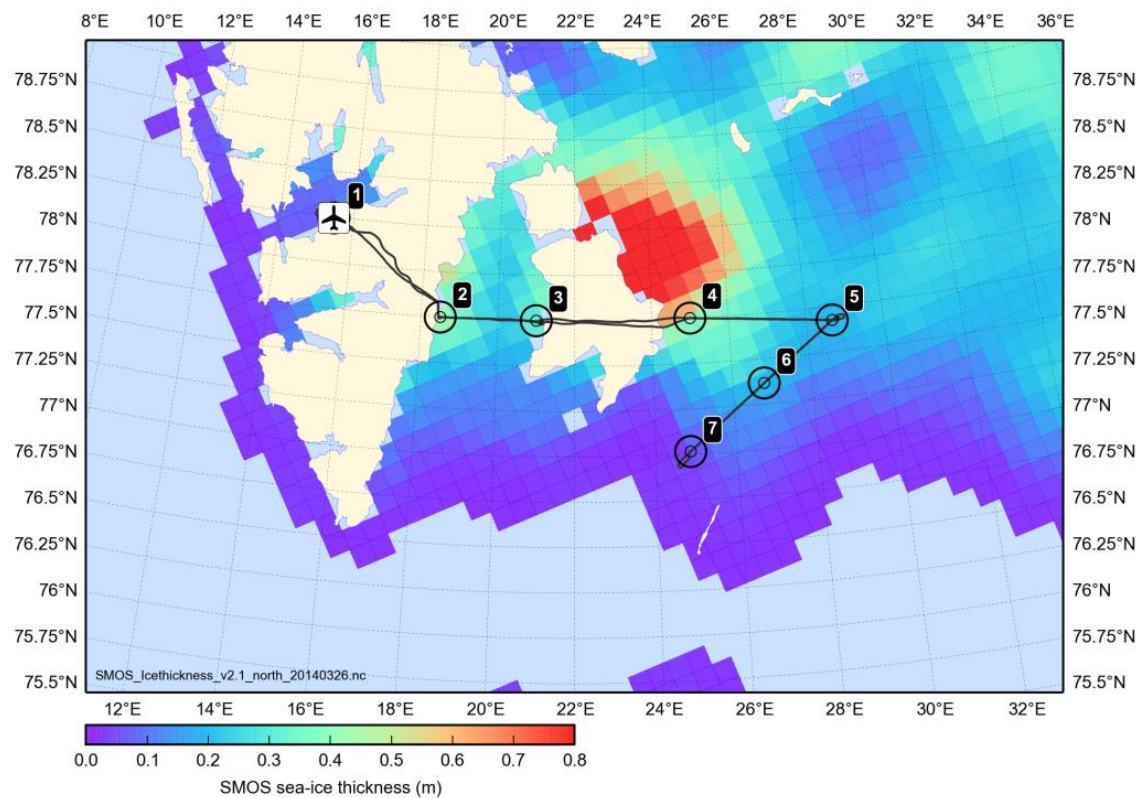


Figure 4: Waypoints and flight track of survey 20140326_01

SMOSice2014 - 2014/03/26 - Science Mission - CryoSat-2 #1

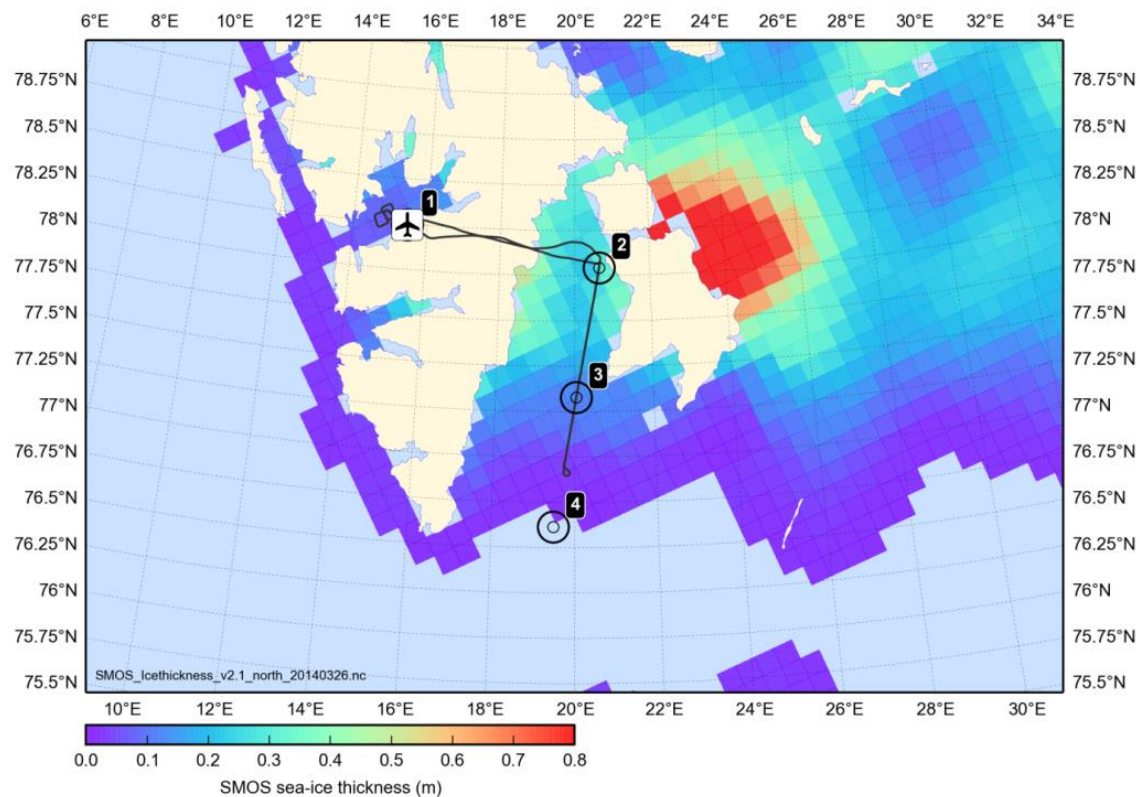


Figure 5: Waypoints and flight track of survey 20140326_02

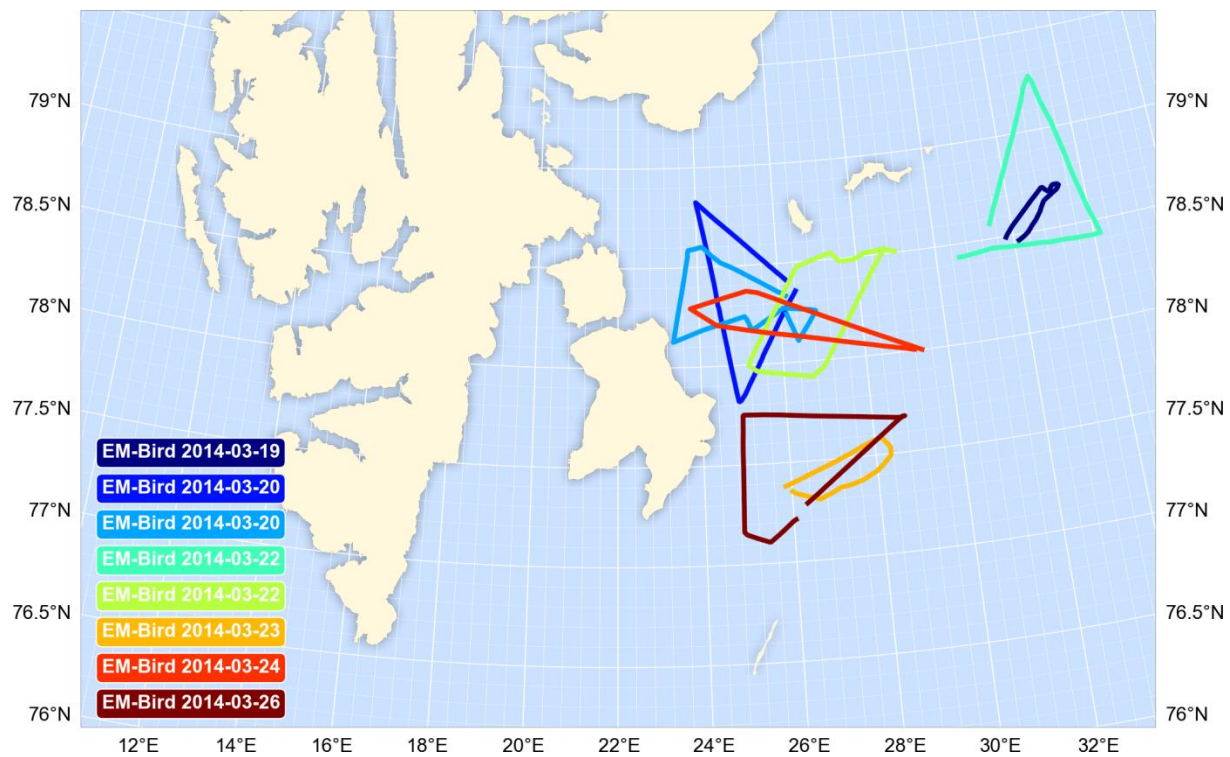


Figure 6: Overview of all helicopter AEM sea-ice thickness surveys

2.1 Polar-5 Instrumentation

This section gives a brief overview of the instrumentation installed on the polar research aircraft “Polar-5” of the Alfred Wegener Institute.



EMIRAD

The EMIRAD-2 L-band radiometer system has been developed by DTU-Space, and operated in a range of campaigns, known as the CoSMOS campaigns, in support of SMOS. It is a fully polarimetric (4 Stokes parameters) system with advanced RFI detection features (kurtosis and polarimetry). The system has operated successfully on different aircraft (Aero Commander and Skyvan) in Denmark, Norway, Finland, Germany, France, Spain, and Australia, and 2013 it was operated on the AWI Basler BT-67 (Polar-6) in Antarctica for the DOMECAir campaign. The main features of the system are:

- Correlation radiometer with direct sampling
- Fully polarimetric (i.e. 4 Stokes parameters)
- Frequency: 1400.5 – 1426.5 MHz (-3 dB BW)
1392 - 1433 (-60 dB BW)
- Digital radiometer with 139.4 MHz sampling
- Digital I/Q demodulation and correlation for accurate estimation of 3rd and 4th Stokes
- Advanced analog filter for RFI suppression.
- Additional digital filter bank: 4 sub-bands.
- RFI flagging by kurtosis and polarimetry.
- Data integrated to 1 ms recorded on primary storage PC.
- “Fast data” pre-integrated to 14.4 µs. recorded on dedicated PC.
- Sensitivity: 0.1 K for 1 s. integration time
- Stability: better than 0.1 K over 15 min. before internal calibration.
- Calibration: matched load (ML), noise diode (ND), and active cold load (ACL).

- 2 antennas - one nadir pointing, one side looking at 45 deg. incidence angle
- Antennas are Potter horns with 37.6 deg & 30.6 deg HPBW
- Nadir horn has 210 m footprint from 1000 ft flight altitude
- Tilted horn has 245 m by 320 m footprint, again from 1000 ft flight altitude.
- Each data package time stamped using GPS 1PPS signal with 100 ns accuracy.
- Minimum operating altitude: 250 m above terrain @ 140 knots
- Integrated with Honeywell H-764 GPS/INS unit (EGI) for navigation and attitude data

The installation and functionality of the radiometer system on-board the aircraft was tested during a test flight off Bremerhaven carried out February 19, 2014. The results from the test flight are presented in the data validation section, section 4.9.

Airborne Laserscanner

The laser scanner model used on the Polar-5 was a Riegl VQ-580. The scanner yield linear scans and operates in near infrared with an accuracy and precision of 25 mm over snow and ice.

Manufacturer/Type	Riegl VQ580
Orientation	Nadir
Swath width	+30° - -30° perpendicular to direction of flight
Wavelength	Near Infrared
PRF	50.000 Hz
Ground Resolution	approx. 30 cm @ 200 feet altitude

Snow Radar

The snow-radar was developed by the Technical University Hamburg-Harburg (TUHH) and has been optimized for low-level surveys to comply with the sea-ice thickness sensor (EM-Bird), which is optional for Polar-5.

Frequency Range	8 – 12 GHz
Transmit Power	35 dBm = 3,2 W
Theoretical Resolution	2,5 cm (vsnow = 200 m/μs)
Sample Time	20 ms
Sample Frequency	10 Hz
Antenna (Transmitter/Receiver) Gain	20 dB
Aircraft altitude Range	200 – 300 ft

Radiation and Surface temperature

Polar-5 is equipped with two Kipp&Zonen pyrgeometers of type CGR 4 for measuring broadband hemispheric down- and upwelling thermal (longwave) radiation as well as with two Kipp&Zonen pyranometers of type CMP 22 for measuring broadband hemispheric down- and upwelling solar (shortwave) radiation.

Surface temperature is measured with a Heitronics Kt19.85 II at a rate of 10 Hz with an accuracy of 0.1°C (Manufacturer specifications).

Aerial Photography

Polar-5 is equipped with a nadir-mounted digital camera (Canon EOS 1D Mark III). Photos are taken every ten seconds over sea ice. The resolution of the images is 3888 x 2592 pixels. Due to technical limitations of the internal data acquisition system, the internal timestamp of the camera is only available with full second resolution.

2.2 Helicopter EM-Bird



Figure 7 : EM-Bird operation on the helicopter deck of R/V Lance (Photo: M. Drusch, ESA)

The helicopter stationed on R/V Lance was used to operate an EM-Bird built by Ferra Dynamics Inc., Ontario, Canada. The HEM system is operated at a height of approximately 15 m above the sea ice surface. With a nominal flying speed of 70 knots (36 m/s), the sea ice thickness is measured every 3 to 4 m within a footprint of about 50 m. The HEM system measures the ice thickness by making use of the difference in conductivity between sea ice and sea water. The distance between the HEM system and the snow or ice surface is measured by a Riegl LD90-3 laser altimeter. On flat, homogenous sea ice the accuracy is better than 0.1 m [Haas et al., 2009].

3 Data Processing Steps

3.1 EMIRAD

This chapter describes the calibration of the radiometer data, validation of this calibration and processing for detection and mitigation of RFI.

Calibration theory and procedure

The EMIRAD radiometer data is calibrated in several steps, which will be discussed in the following sections. The overall procedure is illustrated in Figure 8.

The procedure includes the following steps:

- 1) Internal calibrations are used to characterise internal system gain and noise, including the effects of internal physical temperature variations.
- 2) LN2 measurements have been carried out during the campaign. These are used to characterise the losses in the antenna cables and validate the internal calibrations.
- 3) Laboratory measured (and field verified during Bremerhaven validation flight) characteristics of the EMIRAD-2 antennas and OMTs have been taken into account. This is considered sufficient as these are robust passive components, which have remained installed in the aircraft from the validation flight until the campaign start. Measurements during nose and wing wags over ocean are used to validate the calibration, but any effect of the actual installation on the antenna pattern has not been assessed.
- 4) The antenna frame rotation relative to Earth horizontal and vertical polarizations has been computed from EGI data, and the inverse rotation has been applied to the data in order to ensure polarization purity.

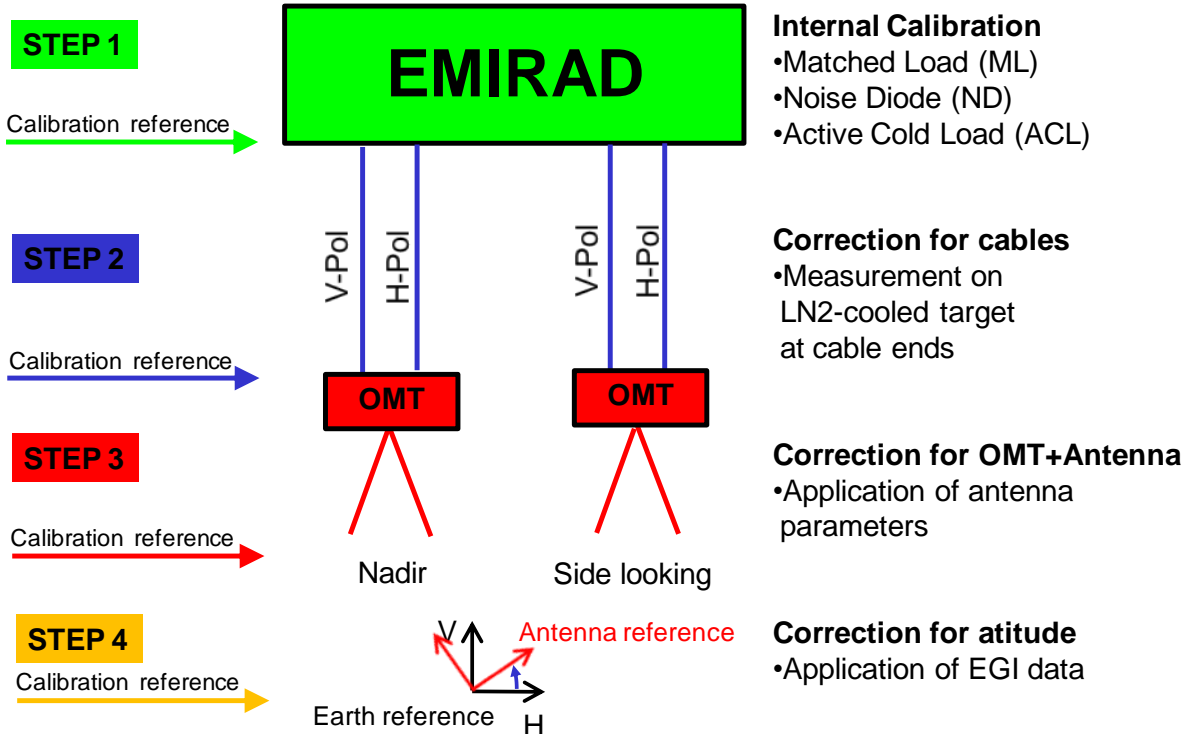


Figure 8: EMIRAD-2 processing procedure

The basic output from the radiometer is a set of files, containing only binary numbers. Data is collected through two analog-to-digital converters (ADC), which follow directly after the analog radiometer section. The analog section amplifies and filters the data. Data from the two converters represent the two linearly polarized channels, V-Pol and H-pol, and samples represent $E_{XM} = A_x(E_x + E_{xN})$, where E_{XM} is the measured data, E_x is the incident electric field to the antenna, E_{xN} is the receiver noise contribution, and A_x is the receiver voltage gain, and where X is replaced by either V or H for each of the two polarizations.

The digital section calculates the four basic outputs, $\langle E_{VM} E_{VM}^* \rangle$, $\langle E_{HM} E_{HM}^* \rangle$, $\langle \text{Re}(E_{VM} E_{HM}^*) \rangle$, $\langle \text{Im}(E_{VM} E_{HM}^*) \rangle$, where $\langle \rangle$ represents integration to 1 ms, and $*$ represents complex conjugation. Furthermore the digital section provides output products for kurtosis estimation as well as housekeeping data, such as temperature measurements at 16 different points within the receiver, and power supply voltages. For the calibration procedure, temperature measurements are the only important parameters, and hence no further detailed discussion about the internal data format will be made.

From the output products, the four modified stokes parameters, (T_V , T_H , U , V), can be derived. The relation between the incident electric field and the brightness temperatures is shown in the left side of equations 1a-1d, where λ is the wavelength, k is Boltzmann's constant and z is the impedance of the medium of wave propagation. The second equal sign follows, as the incident electric field and the receiver noise contributions are statistically independent. The right most equal sign is a simple variable substitution, showing how the desired parameters may be derived from a Gain factor, G_x , and an offset term, representing the receiver noise temperature, T_{Nx} , for each of the two polarizations, respectively.

$$T_V = \frac{\lambda^2}{kz} \langle E_V^2 \rangle = \frac{\lambda^2}{kz} \left(\frac{1}{A_V^2} \langle E_{VM} E_{VM}^* \rangle - \langle E_{VN} E_{VN}^* \rangle \right) = \frac{1}{G_V} \langle E_{VM} E_{VM}^* \rangle - T_{NV} \quad (1a)$$

$$T_H = \frac{\lambda^2}{kz} \langle E_H^2 \rangle = \frac{\lambda^2}{kz} \left(\frac{1}{A_H^2} \langle E_{HM} E_{HM}^* \rangle - \langle E_{HN} E_{HN}^* \rangle \right) = \frac{1}{G_H} \langle E_{HM} E_{HM}^* \rangle - T_{NH} \quad (1b)$$

$$U = \frac{\lambda^2}{kz} \langle 2 \operatorname{Re}(E_V E_H^*) \rangle = 2 \frac{\lambda^2}{kz} \left(\frac{1}{A_V A_H} \operatorname{Re} \langle E_{HM} E_{HM}^* \rangle \right) = 2 \frac{1}{\sqrt{G_V G_H}} \operatorname{Re} \langle E_{HM} E_{HM}^* \rangle \quad (1c)$$

$$V = \frac{\lambda^2}{kz} \langle 2 \operatorname{Im}(E_V E_H^*) \rangle = 2 \frac{\lambda^2}{kz} \left(\frac{1}{A_V A_H} \operatorname{Im} \langle E_{HM} E_{HM}^* \rangle \right) = 2 \frac{1}{\sqrt{G_V G_H}} \operatorname{Im} \langle E_{HM} E_{HM}^* \rangle \quad (1d)$$

In total, the equations demonstrate how the binary output product is directly transferred into **all four desired Stokes parameters**, using only two gain factors and two offset terms G_V , G_H , T_{NV} , and T_{NH} like in a traditional dual polarized radiometer.

If a component is present in front of the receiver, the incident brightness temperature is modified. For a lossy component , equation 2a describes the relation between the incident antenna brightness temperature, T_A , and the actually measured brightness temperature, T_M , where T_P is the physical temperature of the component, and S_{21} is the transmission coefficient (loss expressed as a gain, smaller than 1). For loss less reflective components (mismatched microwave components) equation 2b gives the relation. S_{22} is the reflection coefficient, and T_R is the radiated noise temperature from the receiver, and for this component type the relation $S_{21}=(1-S_{22})$ may be used. For the EMIRAD radiometer configuration, T_R equals the physical temperature of the input circulator, measured within the housekeeping data package. S_{21} and S_{22} can be determined using a VNA (Vector Network Analyser) as well as through external calibration.

$$T_M = S_{21} T_A + (1 - S_{21}) T_P \quad (2a)$$

$$T_M = S_{21} T_A + S_{22} T_R \quad (2b)$$

For components, which are both lossy and reflective, the equations must be combined, and very special care shall be taken, that S_{21} is split up, so that the $(1-S_{21})$ factor in equation 2a ONLY accounts for the Ohmic loss.

For correct measurements of the third and fourth Stokes parameters, U and V, respectively, both receiver channels must have equal phase length. For a small phase difference, ϕ (like in EMIRAD, where fringe washing effects may be neglected), the actually measured parameter set, T_B' , relative to the true parameter set, is found from equation 3. Knowing the actual phase imbalance from calibration, the measured data can easily be corrected through simple matrix inversion of the equation.

$$\overline{T_B}' = \begin{bmatrix} T_V' \\ T_H' \\ U' \\ V' \end{bmatrix} = \begin{bmatrix} T_V \\ T_H \\ U * \cos(\varphi) + V \sin(\varphi) \\ -U * \sin(\varphi) + V \cos(\varphi) \end{bmatrix} = \begin{bmatrix} T_V \\ T_H \\ U \\ V \end{bmatrix} \begin{bmatrix} 1 & 0 & 0 & 0 \\ 0 & 1 & 0 & 0 \\ 0 & 0 & \cos(\varphi) & \sin(\varphi) \\ 0 & 0 & -\sin(\varphi) & \cos(\varphi) \end{bmatrix} \quad (3)$$

Internal calibration

The first calibration step is internal calibration of the radiometer receiver itself, based on equations 1a-1d. In each channel the receiver has a low-loss switch at the input, which selects one of the four input sources: Antenna A (nadir looking horn), Antenna B (side looking horn), Matched load (ML), or Active cold load (ACL). Furthermore a common noise diode (ND) is coupled to the two receiver channels, enabling addition of a known amount of noise on top of the selected source. The feeding network for the noise from the noise diode, which is a purely passive network, is phase matched to better than 1 degree, hence enabling calibration of the phase coherence of the two receiver channels as described above. All three calibration sources are temperature monitored, and the ACL as well as the ND have been carefully characterized with respect to repeatability and temperature sensitivity. Both exhibit an extremely high repeatability, and no measurable changes are observed, even for longer storage or use times.

Figure 9 gives an overview of the setup. It shall be noticed, that the figure only shows one antenna in front of the switch as well as only one polarization in order to keep the illustration simple.

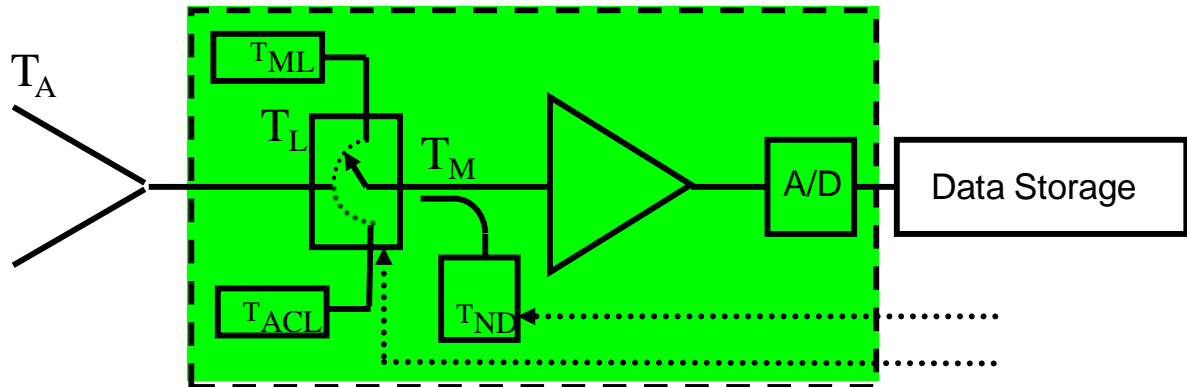


Figure 9: EMIRAD-2 internal calibration sources.

Table 3 gives a survey of the sources in terms of expected brightness temperatures and temperature sensitivity coefficients. Although the ND is common to the two channels, losses are different through the two signal paths, and hence the sensitivities are not exactly equal.

Table 3: Calibration sources, expected output, and temperature sensitivity.

Type	Brightness Temperature	Sensitivity
ML, H-Pol	Physical temperature, 318-323 K (individually measured)	+1.000 K/K
ML, V-Pol		+1.000 K/K
ND, H-Pol	Input source + 141.02 @ $T_{\text{physical}} = 318.33 \text{ K}$	Input source + 0.144 K/K
ND, V-POL	Input source + 132.23 @ $T_{\text{physical}} = 318.33 \text{ K}$	Input source + 0.127 K/K
ACL, H-Pol	60.58 K @ $T_{\text{physical}} = 323.00 \text{ K}$	+0.712 K/K
ACL, V-Pol	60.53 K @ $T_{\text{physical}} = 323.00 \text{ K}$	+0.629 K/K

For each channel, only two calibration points are required, and the main scheme is either ML/ACL or ML/ML+ND. For both schemes, the third calibration source is used for data validation. For this campaign, ML/ML+ND has been chosen, hence with ACL and ACL+ND as validation points. The ND is pulsed every second with a duty cycle of 20%, independent from the input switch position, and theoretically the gain calibration could be continuously adjusted. However, due to the risk of gain estimation errors caused by RFI, this option is not used, and ND observations are uniquely used during calibration events, when the input switch is set to either ML or ACL. For each calibration period, the calibration constants, G and T_N , can be determined, but for correct calibration at all observation times, calibration data is linearly interpolated between calibration events, and an individual set of G and T_N is determined for each data point.

The time interval between calibration events depends upon the stability of the radiometer receiver, which again is strongly dependent upon the temperature stabilization. A good impression of the receiver stability is obtained from estimation of the Allan deviation, i.e. the sample-to-sample variation, ΔT , for different integration times, τ . The radiometer is connected to a stable (internal) target, and is left without calibration events throughout the whole test. For an ideal radiometer, ΔT will decrease by the square-root of N , when the integration period length is increased by a factor of N , but for very long integration times, a non-ideal radiometer adds a term to ΔT based on the internal drifts, and eventually this term will become dominant. For the EMIRAD H-channel, ΔT as a function of the integration time τ is seen in Figure 10, where the dotted line is the behaviour of an ideal instrument. The non-linearity between 10 s and 500 s is mainly caused by the period of the temperature regulation system, while the increase from 500 s and beyond is caused by long-term component drifts. It is seen, that the radiometer stays around $\Delta T=100$ mK for a wide interval of observation times, and there is no indication, that drifts are significantly compromising data, when the receiver is only calibrated every 500-1000 s (8-16 minutes).

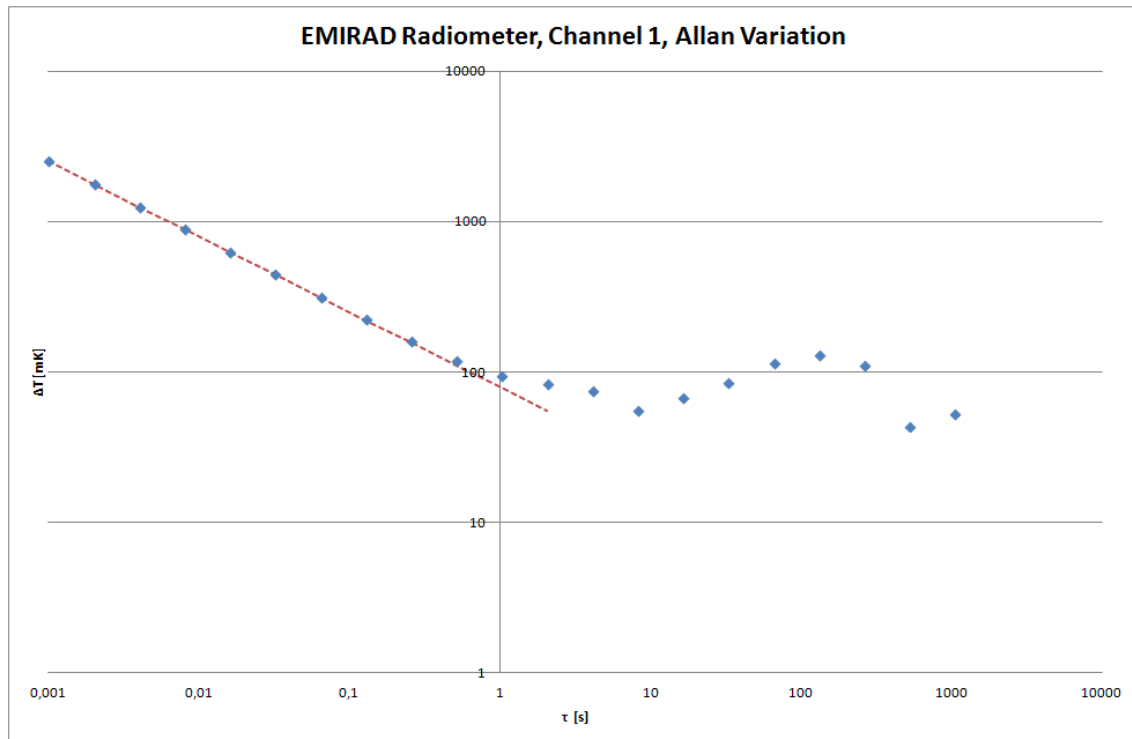


Figure 10: Allan Variation for EMIRAD H-channel.

Both receiver channels, i.e. the V-pol and the H-pol, are calibrated according to the same calibration procedure, and both channels exhibit similar sensitivities and drifts. The third and fourth Stokes parameters are calibrated according to equations 1c and 1d, using the gain, G, values determined for each of the main channels. Using the ML+ND observations, the actual phase imbalance between the two channels can be found, and through matrix inversion of equation 3, possible influence from imbalance can be removed down to errors of 1 degree. With the internal calibration, the radiometric observations are calibrated to the input connector of the instrument.

External calibration, microwave cables

The next calibration step (step 2) takes the calibration reference from the instrument input connector to the end of the RF-cables, connecting the instrument to the antenna. RF-cables are very high quality Sucoflex 106 type cables, and typical S_{21} values are in the range of 0.1 dB to 0.3 dB, depending on the cable length. S_{21} is factory measured, and VNA-measurements verify the factory values. However, for radiometric applications, even higher accuracy is desired, and for this purpose, observation of a liquid Nitrogen cooled target is applicable. An Ailtech 7009 Standard Noise Generator, see Figure 11, which is a cryostat with a broadband matched load ($S_{11} < -34$ dB), is used for the calibration procedure. Filling the cryostat with liquid Nitrogen yields a brightness temperature equal to the boiling point of the nitrogen, $T_{LN2}=77.25-0.00825*(1013.25 \text{ HPa} - p)$, where p is the air pressure. Finally inversion of equation 2a yields S_{21} for the cable.

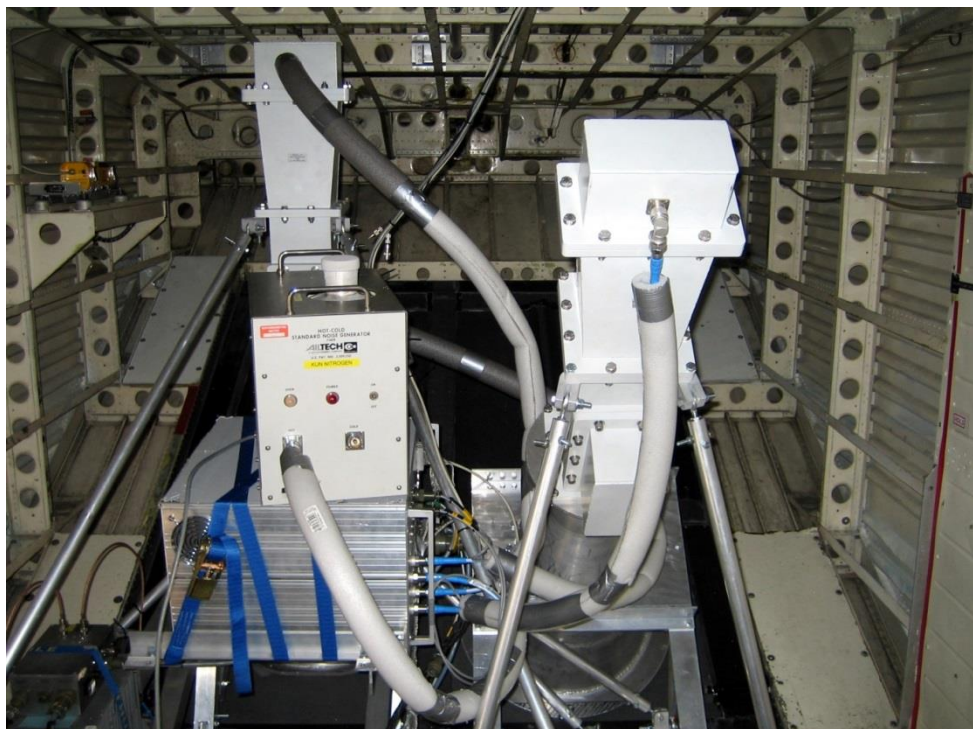


Figure 11: Ailtech 7009 Standard Noise Generator used for EMIRAD calibration.

Theoretically this procedure should only be necessary once, as the cables are passive components, but the observations provide a good system check, and it ensures repeatability and comparability for data sets, taken over longer time intervals, e.g. the actual campaign. Furthermore it also removes any possible uncertainties within the instrument input switch, as

the liquid nitrogen observations are made through the exact same signal path as the antenna measurements. Hence all four input cables (V-Pol and H-Pol for each of the two antennas) shall be connected to the liquid Nitrogen cooled matched load at least once for each science flight, either prior to take-off or after landing, and a total of 3 (see **Table 3.4**) liquid Nitrogen calibration events took place during the campaign. Cables were left mounted on the radiometer box through the whole campaign, and only the connector at the antenna/OMT was unmounted/remounted.

For each calibration event, the four S_{21} values were calculated, and for almost all calibration events, the measurements were very consistent within ± 0.01 dB (equivalent to 0.5 K measurement uncertainties). This consistency could not justify individual settings for each flight, as the deviations were of the level of measurement accuracy, and in this case individual settings could introduce artificial measurement deviations. The estimates of the S_{21} parameters have been averaged for each cable, see Table 4, and results were found to be consistent with the numbers, provided by the manufacturer, and the numbers found during earlier campaigns. It is noted, that horn B numbers are slightly higher than horn A numbers. This is simply explained by the length of the cables, as Horn B cables are 1.5 m long compared to the 1.0 m horn A cables. Also it is seen, that V-Pol numbers are lower than H-Pol numbers. This is a result of slightly different input switch performances, and again it is well in line with component parameters. Hence the numbers in Table 4.2 were used to adjust all measured data according to equation 2a.

Table 4: Estimated cable losses.

Cable	S_{21}
Horn A, H-Pol	-0.2017 dB
Horn A, V-Pol	-0.1685 dB
Horn B, H-Pol	-0.2771 dB
Horn B, V-Pol	-0.2303 dB

External calibration, antenna system

The third calibration step is to move the calibration reference from the RF-cable connectors to the antenna aperture, i.e. correcting for the influence from the antennas and the Orthomode Transducers (OMTs) using equation 2a and 2b. Prior to the campaign, measurements of S_{21} and S_{22} were made on a VNA, and results are seen in Table 5. The values have been validated through measurements of the cold sky, using exactly the setup to be installed in the aircraft.

Table 5: Estimated S-parameters for the antenna system.

Port	S_{21}	S_{22}
Horn A, V-Pol	-0.10 dB	-33.6 dB
Horn A, H-Pol	-0.08 dB	-21.0 dB
Horn B, V-Pol	-0.10 dB	-29.4 dB
Horn B, H-Pol	-0.08 dB	-20.1 dB

The values may be affected by the antenna installation into the aircraft frame, and hence it is important to verify the numbers during the first validation test flight (from Bremerhaven). A portable VNA, Agilent Technologies N9918A, was used, and an example measurement is seen in Figure 12, illustrating S_{22} for the H-port on antenna A. The measured data must be averaged over the whole band of interest, 1400 MHz-1427 MHz, and results show very similar results to the values, found in the laboratory. For the example shown, the average value equals -20.2 dB, which is within the VNA accuracy. As all deviations are within the expected measurement accuracy, and as the laboratory VNA has a more accurate calibration kit, the numbers in Table 5 are applied to the data set unchanged.

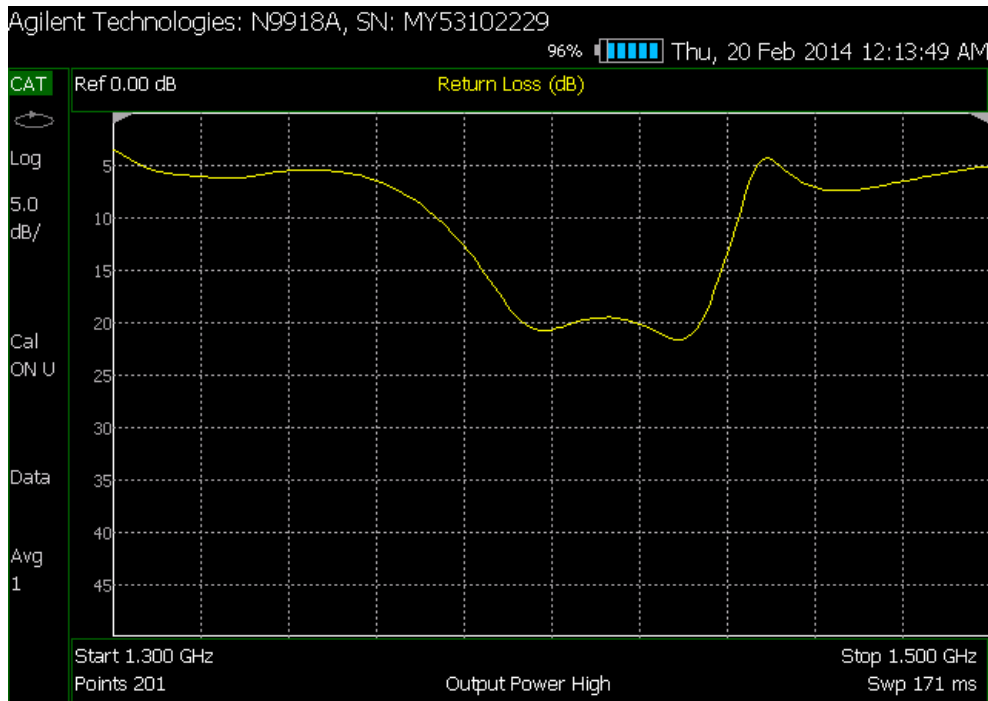


Figure 12: VNA measurement of S_{11} for the V-port of antenna A (Nadir).

Radiometer data is adjusted according to the equations, and values were assumed to be constant throughout the campaign – a fair assumption as the antenna system consists only of bulky metal structures.

The OMT has a known phase imbalance between the two polarization ports equal to $\phi = -12.4$ degrees, which causes the third and fourth Stokes parameters to mix as described by equation 3. Using matrix inversion of the equation, the effect is removed.

Any antenna will cause a coupling between orthogonal channels, known as cross polarization. As the cross polarization level is relatively low for the Potter horn antenna type, the effect is not significant for the pure T_V and T_H measurements at most targets and incidence angles. Only for very high incidence angles over the ocean, where the channels yield very different measurement values, some deviation can be seen. For a polarimetric radiometer, however, cross polarization will cause a false signal in the 3rd (or 4th) Stokes parameter, equal to the signal, which would be caused by cross talk between channels. Unlike cross talk, the magnitude and sign of the false signal will vary over the footprint (different sign on opposite sides of boresight), and thus for a completely homogeneously illuminated foot print (e.g. nadir looking at a homogeneous target), the effect will fully cancel. For non-homogeneous target types, and/or when the incidence angle is large, i.e. when the

two half-planes of the foot print are relatively different, the cross polarization effect may cause the 3rd Stokes parameter to shift several K. This effect is not corrected for, as it requires a forward model to predict the brightness temperatures of the target, but as it affects only the 3rd Stokes parameter for some special cases (during wing wags), it is not considered a problem.

Attitude parameter determination and corrections

During all flight operations navigation data is collected, using the Honeywell H-764 Embedded GPS/INS (EGI). The unit provides information about position (Latitude, Longitude, and Altitude), and it also provides attitude data, i.e. pitch, roll and true heading, with an accuracy of 0.05 degrees and with an update rate of 50 Hz. For scientific purposes, this data must be transformed into traditional remote sensing parameters, such as incidence angle with respect to nadir, observation direction with respect to Earth North, and rotation of the antenna reference frame (Horizontal and Vertical linear polarizations) with respect to the true Earth Vertical and Horizontal directions.

This transformation requires detailed knowledge about the actual installation of the antennas in the aircraft, and during the installation process, each antenna probe (V-Pol and H-Pol) orientation is measured using the EGI, and finally the EGI itself is fixed and again readings are made. The EGI readings are used to specify the aircraft reference frame, and using the probe measurements, each antenna probe orientation can be expressed uniquely in this reference frame. For each scientific measurement point, the EGI readings are used to specify, how the aircraft reference frame is oriented within the Earth reference frame, and the actual co-ordinate transformation matrix can be generated. Using standard linear algebra, each antenna probe can be expressed in the Earth reference frame, and finally the desired parameters can be derived. As an example, the measurement of the H-pol probe of the nadir horn is illustrated in Figure 13.



Figure 13: Orientation measurement for the nadir H-pol probe.

In the final EMIRAD data set, measured navigation data is provided along with the derived remote sensing parameters for easy data processing and application.

Knowing the actual rotation of the aircraft reference frame with respect to the Earth reference frame, Θ , the influence on the measured data can be calculated. Using the definitions of the true Stokes parameters, $I=T_V+T_H$, and $Q=T_V-T_H$, the actually measured parameters, T_B' , are given by equation 4.

$$\bar{T}_B' = \begin{bmatrix} I' \\ Q' \\ U' \\ V' \end{bmatrix} = \begin{bmatrix} I \\ Q^* \cos(2\theta) + U \sin(2\theta) \\ -Q^* \sin(2\theta) + U \cos(2\theta) \\ V \end{bmatrix} = \begin{bmatrix} 1 & 0 & 0 & 0 \\ 0 & \cos(2\theta) & \sin(2\theta) & 0 \\ 0 & -\sin(2\theta) & \cos(2\theta) & 0 \\ 0 & 0 & 0 & 1 \end{bmatrix} \begin{bmatrix} I \\ Q \\ U \\ V \end{bmatrix} \quad (4)$$

Inversion of the matrix can be used to remove the effect, and this correction has been applied to all data from the campaign. While some applications prefer this correction, other applications prefer access to the raw, measured data from each channel. Hence the final data set is delivered in both versions (See chapter 5 for details).

Statistical RFI analysis and mitigation

In the data set, analyzed in this report and delivered to the end users, data has been screened for RFI by evaluating kurtosis, polarimetric, and brightness temperatures anomalies as summarized in the steps listed below:

- Kurtosis ratios have been estimated for all data samples acquired when observing the antennas of the EMIRAD-2 system [3]. These have subsequently been compared to the kurtosis ratios derived from the data samples recorded during observations of the internal calibration loads of the system – the latter set of data samples is known to be free from RFI. All antenna-related data samples exhibiting kurtosis ratios deviating more than ± 4 standard deviations from the mean of the clean kurtosis ratios have been flagged as RFI contaminated.
- Elevated values of the 3rd and 4th Stokes parameters have been shown to be a powerful indicator of RFI, hence all data samples with 3rd or 4th Stokes parameters greater than ± 10 K have been marked as contaminated by RFI as well. The threshold of ± 10 K has been established during analyses of data from previous EMIRAD-2 campaigns as providing a reasonable level of RFI detection capability whilst keeping the number of false alarms at a minimum [3]. During the test flight and the first two campaign flights from Longyearbyen, a special continuous wave (CW) RFI (see section 4.8 for details) from a video camera was present, which added a constant offset to three of the four channels from the nadir antenna, including the 3rd and 4th Stokes parameters. To avoid flagging practically all data, the threshold limits were adjusted to ± 10 K symmetrically around the mean value for the contaminated part of the data set.
- Finally, all occurrences of unnaturally elevated brightness temperatures have been marked as affected by RFI. In the present data set, all brightness temperatures above 320 K have been characterized as unnaturally elevated.

All data samples flagged by any combination of the three steps above have been removed from the data set. This, however, does not guarantee that *all* data samples still contained within the cleaned data set are indeed free from RFI: special cases might go un-noticed by the detection methods used.

Most (more than 90%) of the flagged samples have been caught by the polarimetric detection. Samples contaminated by the CW source, described in section 4.8, have not been flagged due to the detection threshold adjustment, and as kurtosis is also practically blind to CW type of RFI, the influence from this particular source has not been mitigated by the statistical methods. Table 6 gives a survey of the complete presence of RFI (apart from the CW source).

Table 6: Percentage of RFI flagged samples.

Flight	% Flagged Nadir looking	% Flagged Side looking
Science flight 1	16.3 %	11.2 %
Science flight 2	12.9 %	19.1 %
Science flight 3	20.6 %	28.7 %

When subtracting the mean value of the cleaned data from the mean value of the full, not-cleaned data, the following is noticed:

- Very little difference for the side looking horn, typically a few K. Although RFI is detected, it generally is of quite low intensity.
- For the nadir looking horn the difference is larger, typically 10 K, and especially for science flight 3, there is a difference of 25 K between raw and cleaned data.

In short: there is indeed RFI of significance around Svalbard (or the aircraft itself!), but apart from CW type RFI, it can be mitigated using statistical methods, and the loss of data does not influence final data quality (radiometric sensitivity).

The presence of RFI is not distributed evenly over the target area, as illustrated in Figure 14 and Figure 15 for the nadir looking and the side looking antenna, respectively. This indicates that the RFI either originated from sources on the ground (e.g. the airport or Longyearbyen), or that certain instrumentation on board the aircraft causes the interference, e.g. radio communication.

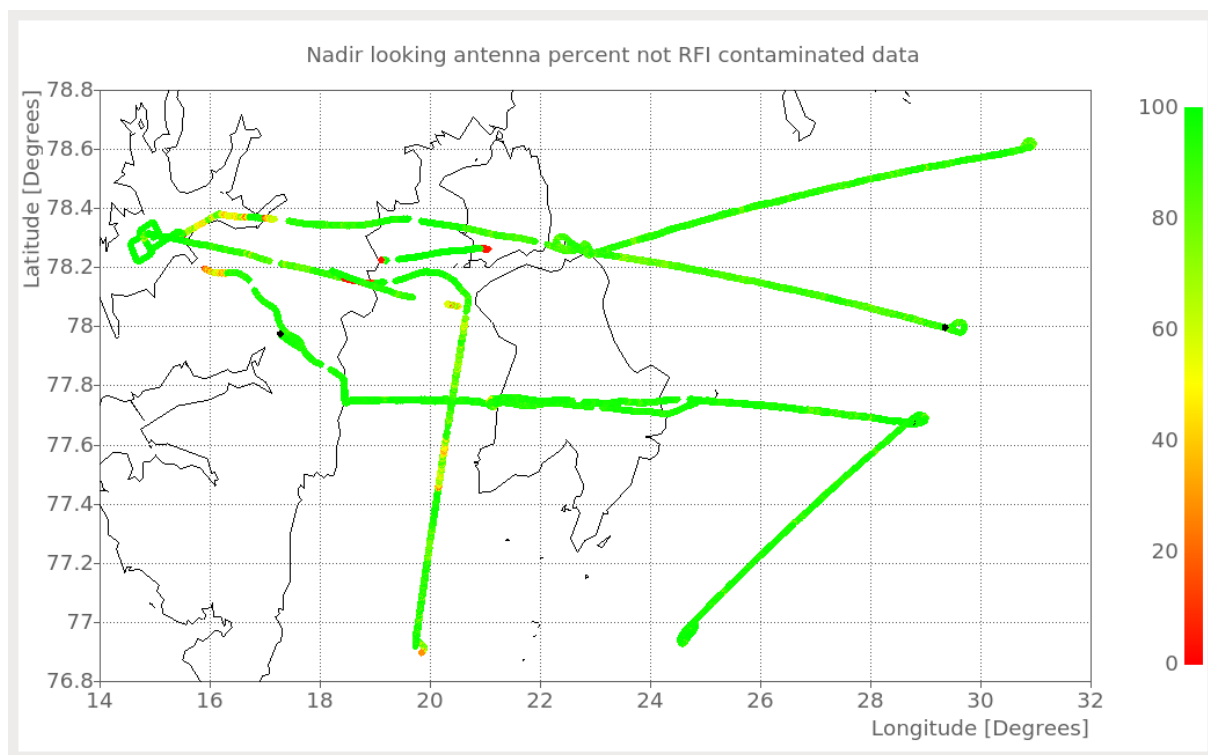


Figure 14: Geographical distribution of RFI for the nadir looking antenna.

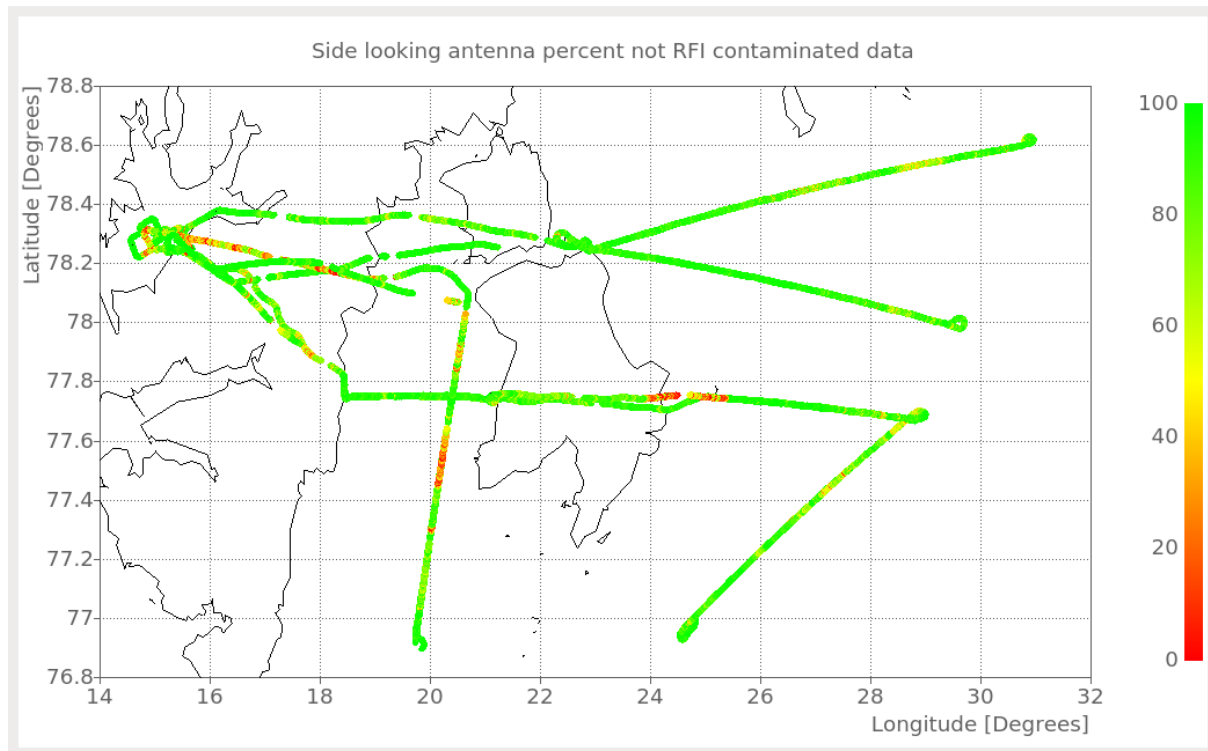


Figure 15: Geographical distribution of RFI for the side looking antenna.

Data integration

Following the sample-to-sample RFI evaluation, data samples, which are not flagged, may be integrated. All data samples found to be affected by RFI have been removed from the data set. The initial sampling to 1 ms observation periods is uniquely done with respect to mitigation of pulsed RFI, and this sampling rate represents an oversampling by more than a factor of 1000 at the expense of radiometric sensitivity. Hence data is integrated to 100 ms and to 1 s, which still both provide oversampling with respect to the antenna footprint size. The final full data set is delivered with both sampling rates.

Mitigation of special on-board CW type RFI

A special RFI situation applies to the nadir looking horn, especially the horizontal channel. During the Svalbard validation flight, a 20 K offset relative to the nadir vertical channel and to modelled, expected brightness temperatures, was detected. RFI was suggested as a possible reason, but the source was not revealed until survey 3, where a camera was not switched on during the first open ocean sections of the flight, causing no offset to be present. When the camera was later turned on, the 20 K offset reappeared. The camera produces a continuous wave type of RFI, and hence it is not detectable through the kurtosis method, being rather insensitive to this kind of signals. The original polarimetric detection algorithm would discard around 95% of all data from the nadir horn, and hence the detection limits for the algorithm have been modified according to the magnitude of the offset for all data except survey 3. Still 10% - 30% of data samples are discarded. The camera was not present during the Bremerhaven test flight, and hence it was not detected as a possible RFI source prior to the campaign.

In order to mitigate the RFI from the camera, first the nature of the contamination must be investigated. If the signal is pure continuous wave (CW) with a constant magnitude, it will add a constant offset to the measured brightness temperatures, and in this case, it may be subtracted, as the power from the RFI-signal and the power from the natural target are statistically independent signals. However, it must first be confirmed, that the RFI is pure CW (no pulsed nature), that the magnitude is constant over time, and that it is truly an additive process (not a multiplicative), which is independent from the actual underlying brightness temperature.

As the RFI- magnitude is close to 20 K, it is easy to make a flagging of samples with the camera on and off, respectively. For most practical measurements, the incidence angle for the nadir horn is less than 5 degrees, and for these incidence angles, there is typically only a few Kelvin difference between natural H-pol and V-pol signals. Hence calculation of the true second Stokes parameter, $Q=V\text{-Pol} - H\text{-pol}$, will yield a good indicator, and a threshold of $Q < -15$ K is set to flag the individual samples. The offset is clearly seen in the Figure 16 and Figure 17, which illustrate data for the two polarizations. For the 3rd survey flight (leg to the South), the offset is no longer present, as the RFI source was identified and switched off.

The statistical investigation of the RFI nature is then based on computation of mean values and standard deviations for sections of flagged and unflagged data for different target types, followed by comparison of the two cases. The analysis must be performed for the H-pol channel as well as the 3rd and 4th Stokes parameters, and the V-pol channel is likewise investigated for comparison and validation. The investigations show:

- The V-pol channel does not change its value over the ocean, when comparing flagged and unflagged data. The mean value is shifted by 0.1 K, which is in fact far below the standard deviation, and hence not statistically significant. On this background it is concluded, that the V-pol channel is not affected by the RFI.
- The standard deviation for neither the V-pol nor the H-pol channel changes between flagged and unflagged data series. Again deviations stay far below the statistical variation, and it may thus be concluded that the RFI is a CW type of signal, i.e. it adds a constant contribution to the brightness temperature (with a zero standard deviation). A pulsed signal or a signal with varying magnitude would change over time, and its statistical standard deviation from sample to sample would hence be non-zero, and it would add to the standard deviation of the natural brightness temperature signal.
- For low brightness temperatures (≈ 100 K), observed over the ocean, the second Stokes parameter yields $Q = -21.02$ K for flagged data, while $Q = +1.51$ K for unflagged data (non-zero due to aircraft pitch, and confirmed through the Klein-Swift model for ocean brightness temperatures).
- Almost identical values, deviating less than 5%, observed for high brightness temperatures (> 200 K), observed over homogeneous snow covered land targets (transit from Longyearbyen to the east coast, without data from Storfjorden), which is again within the statistical uncertainty. From this result and the similar result for low brightness temperatures, it is concluded, that the RFI contribution is independent from the underlying brightness temperature, which characterizes an additive contribution (not multiplicative).
- The same analysis is applied to the 3rd and 4th Stokes parameters with identical conclusions.

The overall analysis outcome concludes, that it can be assumed, that offsets are purely additive, and the added contributions are estimated from the ocean observations. The following values are found:

$$\begin{aligned} \text{H-Pol} &= +22.53 \text{ K} \\ \text{3}^{\text{rd}} \text{ Stokes} &= -11.80 \text{ K} \\ \text{4}^{\text{th}} \text{ Stokes} &= +4.03 \text{ K} \end{aligned}$$

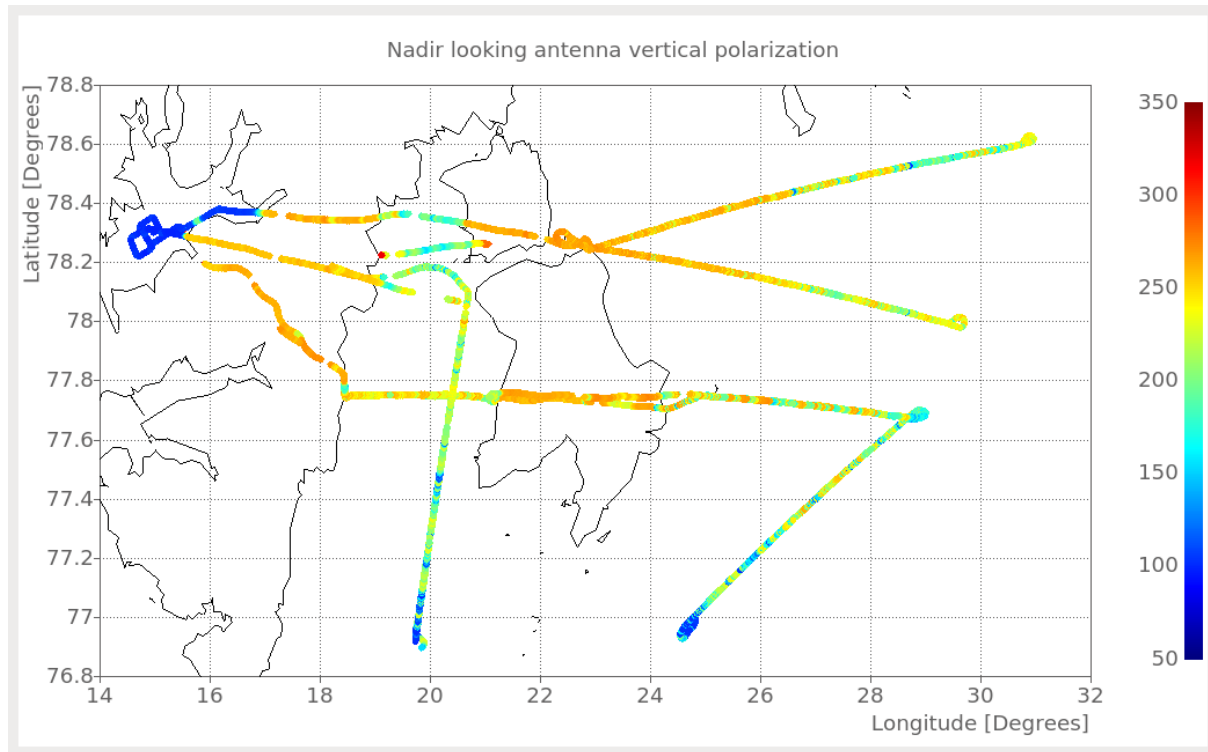


Figure 16: Brightness temperature data, V-pol, nadir looking.

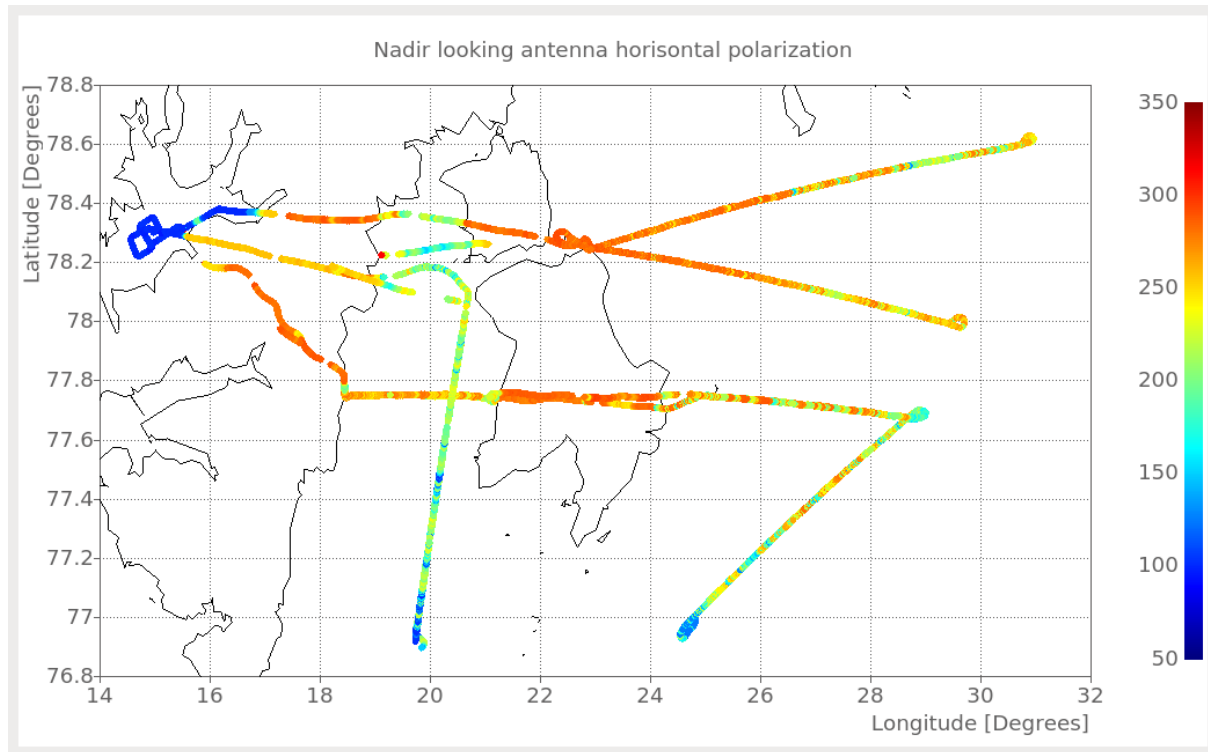


Figure 17: Brightness temperature data, H-pol, nadir looking. RFI present.

For the H-channel it is obvious, that the offset is a positive value, as the power from the RFI is added to the natural brightness temperature. However, for the 3rd and 4th Stokes

parameters, the sign depends upon the phase of the RFI signal, and hence negative values, like the value for the 3rd Stokes, may be found. The impact on the data quality is illustrated further in section 4.9.

The three estimated offset values are finally subtracted from the original data set, and a complete new data release is made on this background. All previous mentioned data deliveries (different integration times, and with/without correction for antenna frame rotation) are reprocessed with the new offsets, and they are thus included in the final delivery.

Data validation using internal ACL and wing wags

The main data validation sources are the internal calibration points and ocean wing wags, i.e. large scale variations of incidence angle and aircraft attitude.

The internal calibration provides validation information, as it is based upon three calibration points per channel instead of only the two, which are required from equation (1a-1d). If the data points deviate from the expected linearity, a warning flag may be set, and eventually data may be discarded, if the error cannot be addressed to one of the calibration points themselves.

For the SMOSice campaign, the only occurrence of a calibration point warning flag occurred at the end of survey flight 2, starting at $t = 1359833246$ s, and ending at landing. The housekeeping data revealed, that a voltage drop with a magnitude of 1 V occurred in a power supply unit, which nominally outputs +15 V, and which is the main supply for the analog front end. The error has neither been observed earlier nor later, and even a thorough laboratory test could not reproduce it. Hence it is difficult to verify the absolute impact on the data quality. Furthermore the typical response of the noise diode (ND) would be to decrease its output, while an active cold load (ACL) output would increase. This is exactly the observation made in the calibration data, but as the effect is very nonlinear relative to the actual supply voltage, it is difficult to assess the absolute impact on the data.

For the actual brightness, the impact can be as high as several Kelvin. However, a crossing with one flight leg of survey flight 3 (acquired few hours later the same day), exist in the data set, and mean values around the tie point indicate little differences. The main reservation regarding the tie point is that it is located over sea ice in Storfjorden, which has a dynamic nature, which may cause natural variations.

As the voltage drop occurred at the end of the flight, it is assumed, that the data loss is fairly limited, and a general warning is set up for the time interval [1359833246 s; 1395838865 s], covering the whole event.

General data validation is based on evaluation of wing wags, performed during test flights. Data from the wags are plotted against the incidence angle, which allows for comparison against modelled data. Figure 18 and Figure 19 show the original data from the Bremerhaven test flight and the test flight from Longyearbyen. For the Bremerhaven test flight, calibration step two, mentioned in section 4.3 could not be performed, as liquid Nitrogen was not available. Hence data is calibrated using information from laboratory measurements of the signal cables. A small offset is noticed between H-pol observations from the two horns, but the result does not raise any warning flags. It shall be noticed, that the camera, causing the RFI contamination, described in section 4.8, was not present during

this flight, and the H-pol offset has no correlation to the later observed offset in the same channel.

From Figure 19 the results from the test flight off Svalbard are seen, and in this figure it is very clearly seen, that there is a significant offset in the nadir H-pol channel – caused by the camera. After the analysis and correction procedures, described in section 4.8, data is plotted again, which is illustrated in Figure 20. In the figure it is seen, that the measured data follows the modelled data as expected, and evaluations of deviations from model data show that errors stay within the expected statistical variation.

The general impression of the test flight data set is, that calibration constants are estimated correctly, and that no further corrections or investigations must be performed.

Liquid Nitrogen calibrations

Table 7 provides a list of the liquid nitrogen calibrations preformed during the campaign. The EGI was not turned on during liquid nitrogen calibrations; hence these data sets are not time stamped.

Table 7: LN2 Calibrations at Svalbard.

Date	When	Special circumstances
20130323	After validation flight	Calibration done twice in succession to assess repeatability.
20140324	After survey 1	Calibration done twice in succession to assess repeatability.
20140326	Never	No LN2 calibration following survey 2 and survey 3 due to airport closing time restrictions.
20140327	In the morning	Calibration performed in order to compensate the missing calibration following survey 3. Calibration done twice in succession to assess repeatability.

Presentation of delivered data set

With the results and corrections described in this chapter, the final data set is ready for delivery in the different versions with respect to integration time, RFI corrections, and antenna frame rotation. Chapter 5 gives a complete description of file formats and data folder structure.

Overview plots have been made for all four channels, using data, which is integrated to 1 s, which has not been corrected for antenna frame rotation, and which has been offset adjusted according to the RFI removal, described in section 4.8. The four plots are found in Figure 21 through Figure 24.

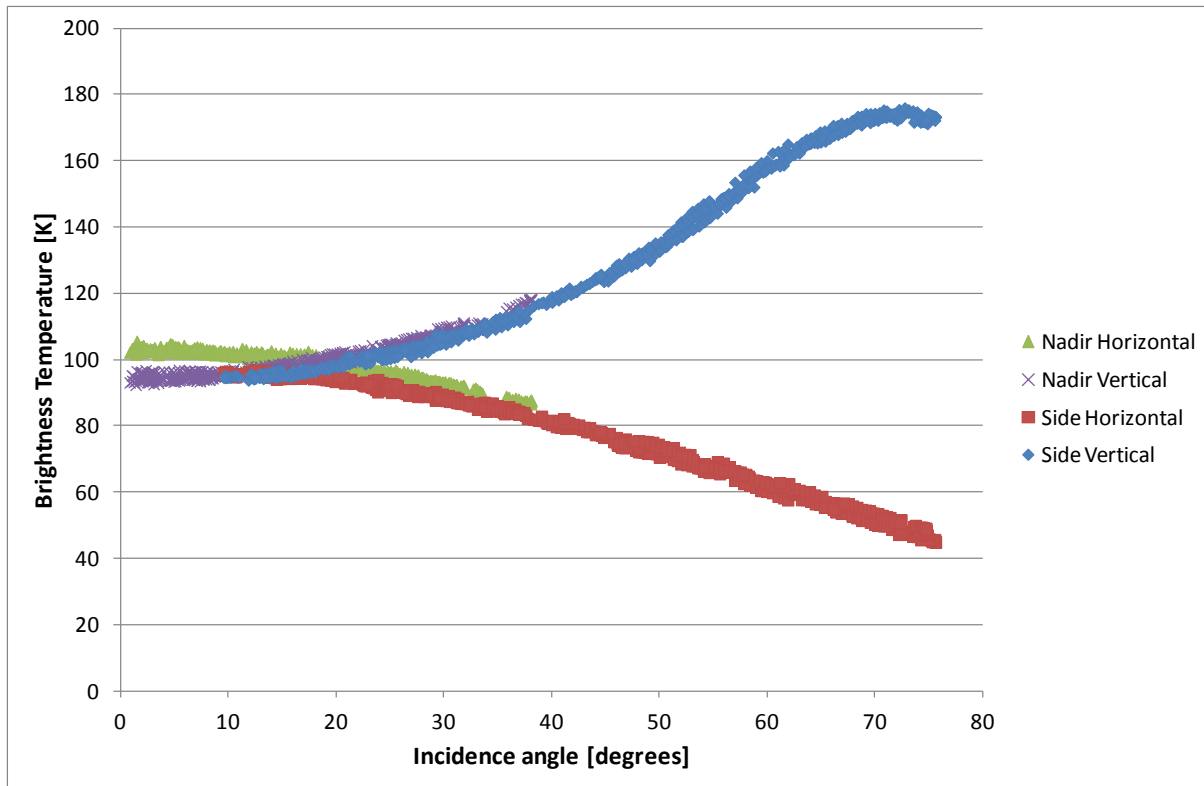


Figure 18: Brightness temperature data for wing wags, Bremerhaven test flight.

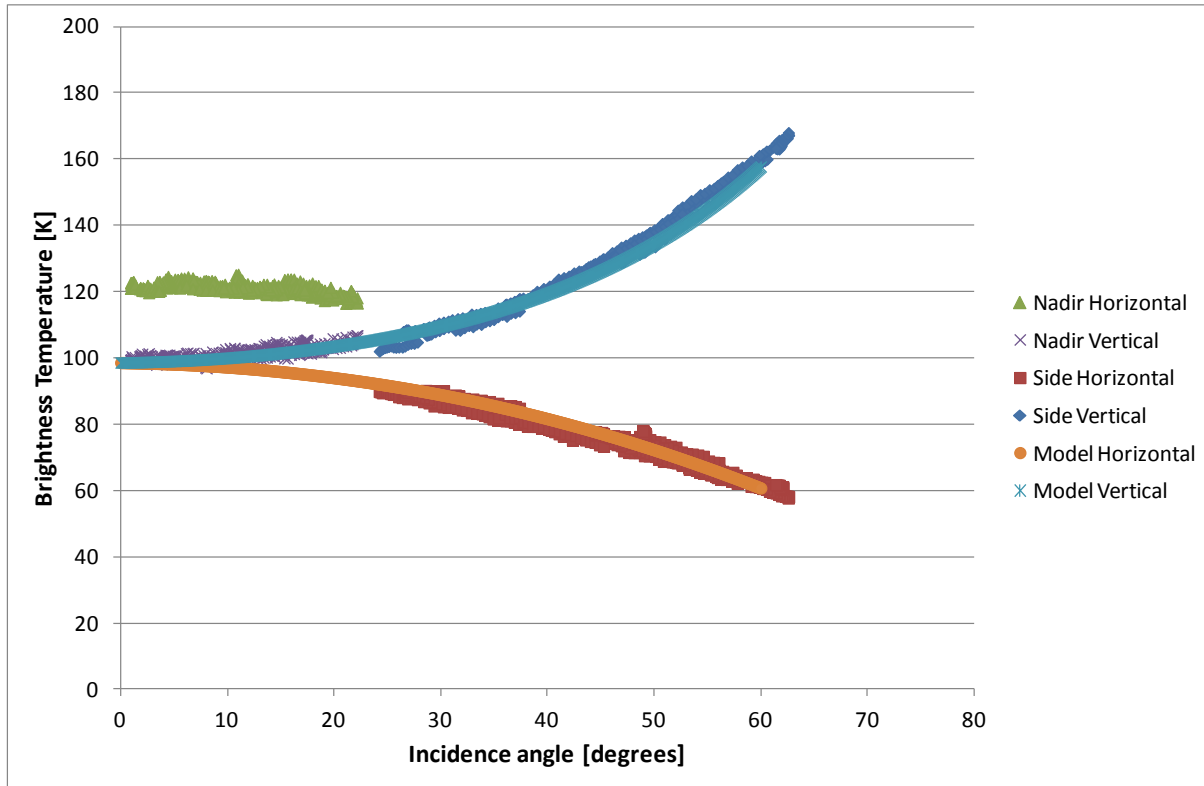


Figure 19: Brightness temperature data for wing wags, Svalbard test flight with camera RFI present.

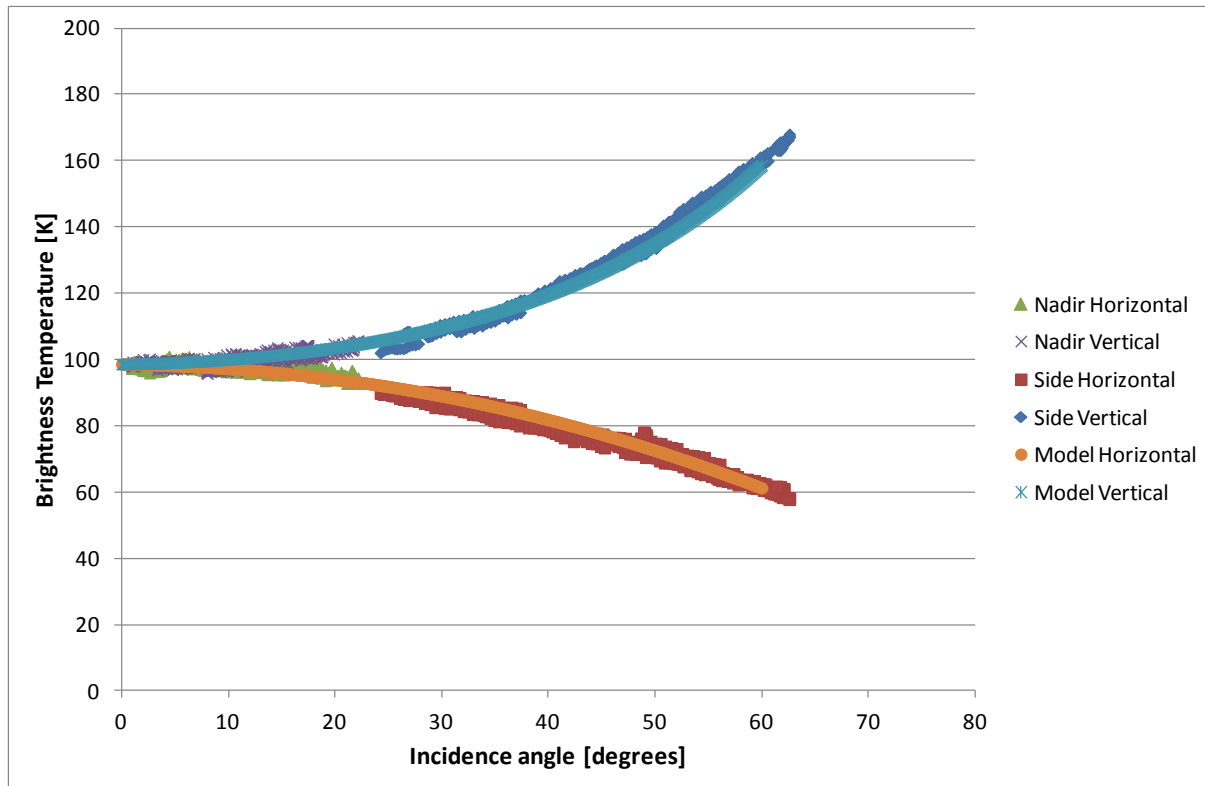


Figure 20: Brightness temperature data for wing wags, Svalbard test flight after removal of camera RFI.

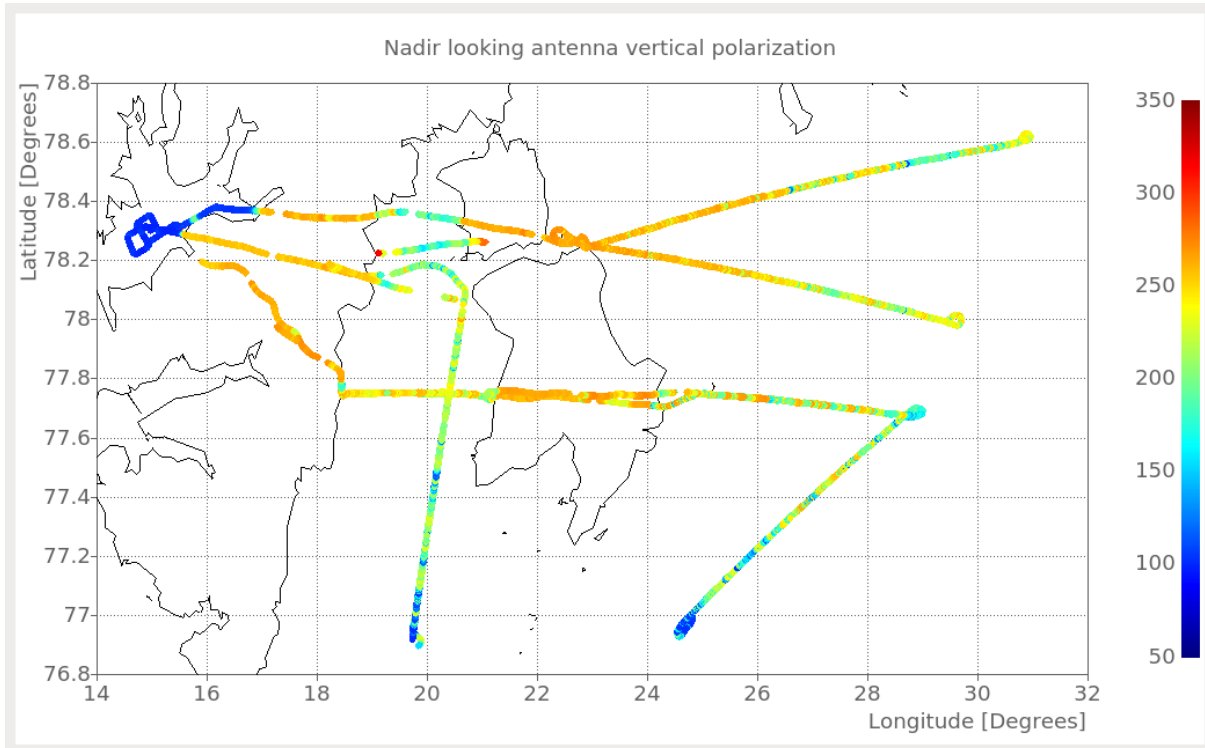


Figure 21: Brightness temperature data, V-pol, nadir looking.

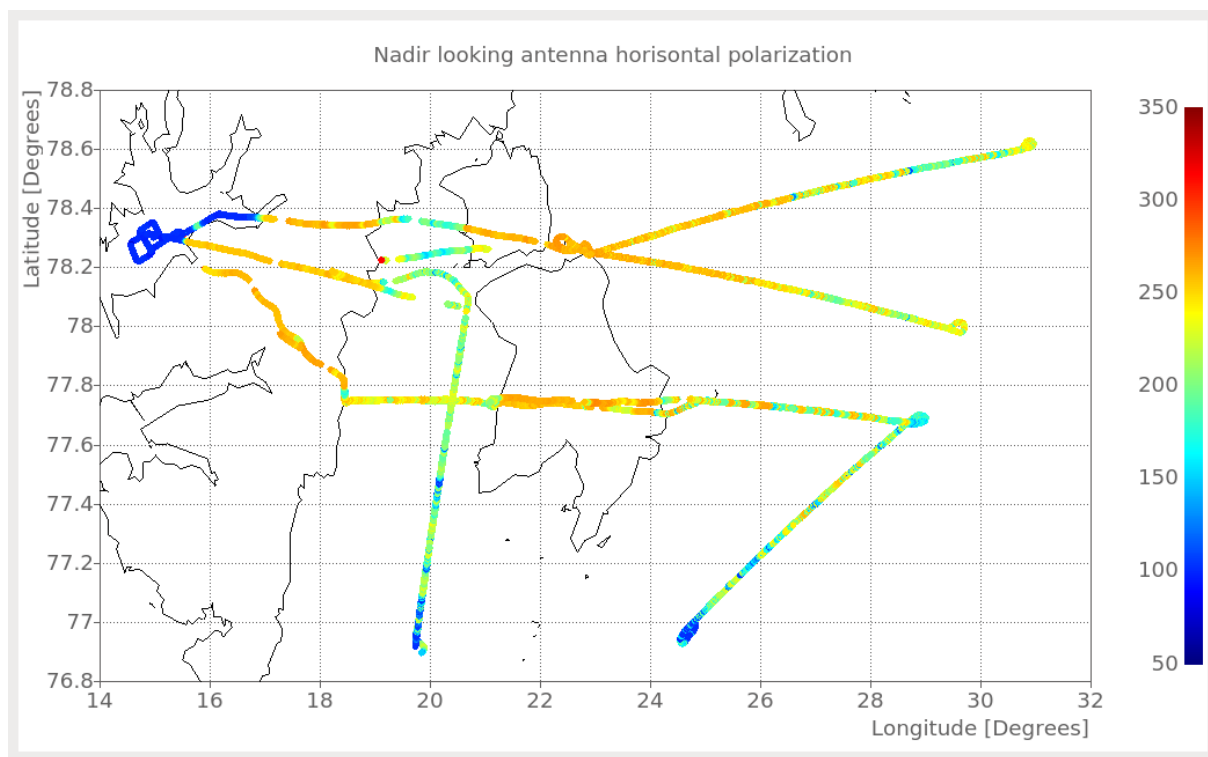


Figure 22: Brightness temperature data, H-pol, nadir looking.

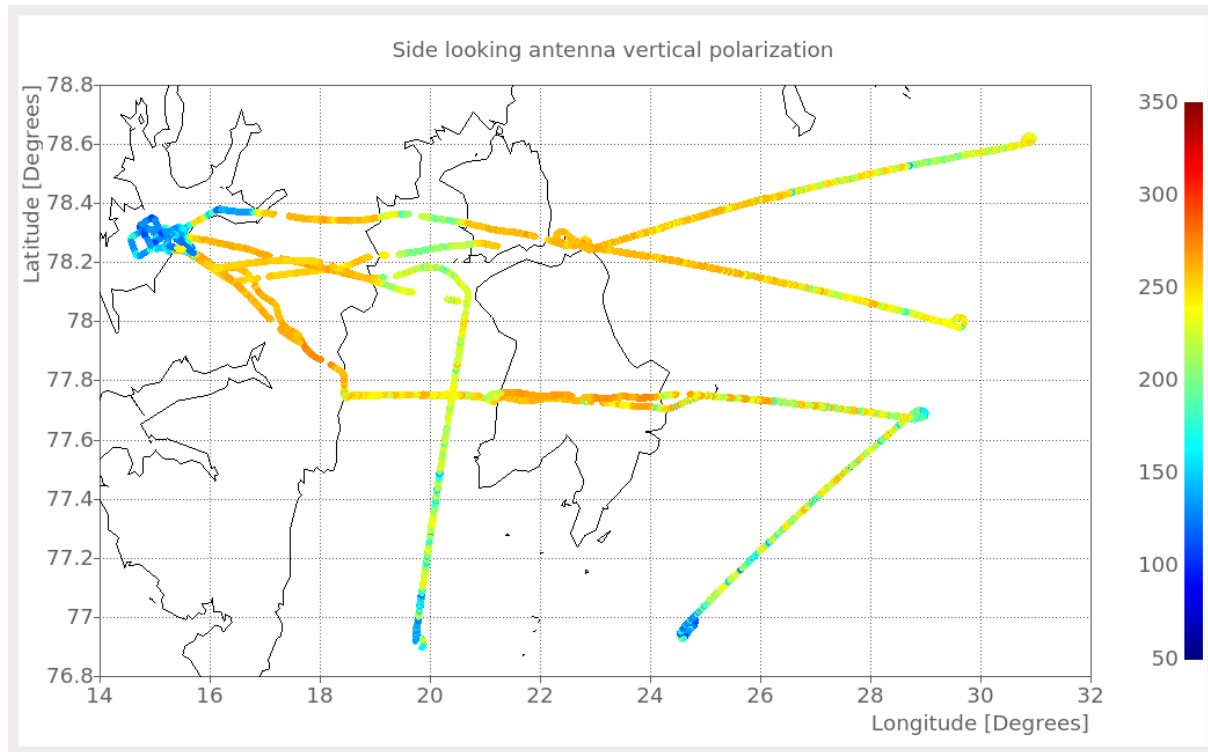


Figure 23: Brightness temperature data, V-pol, side looking.

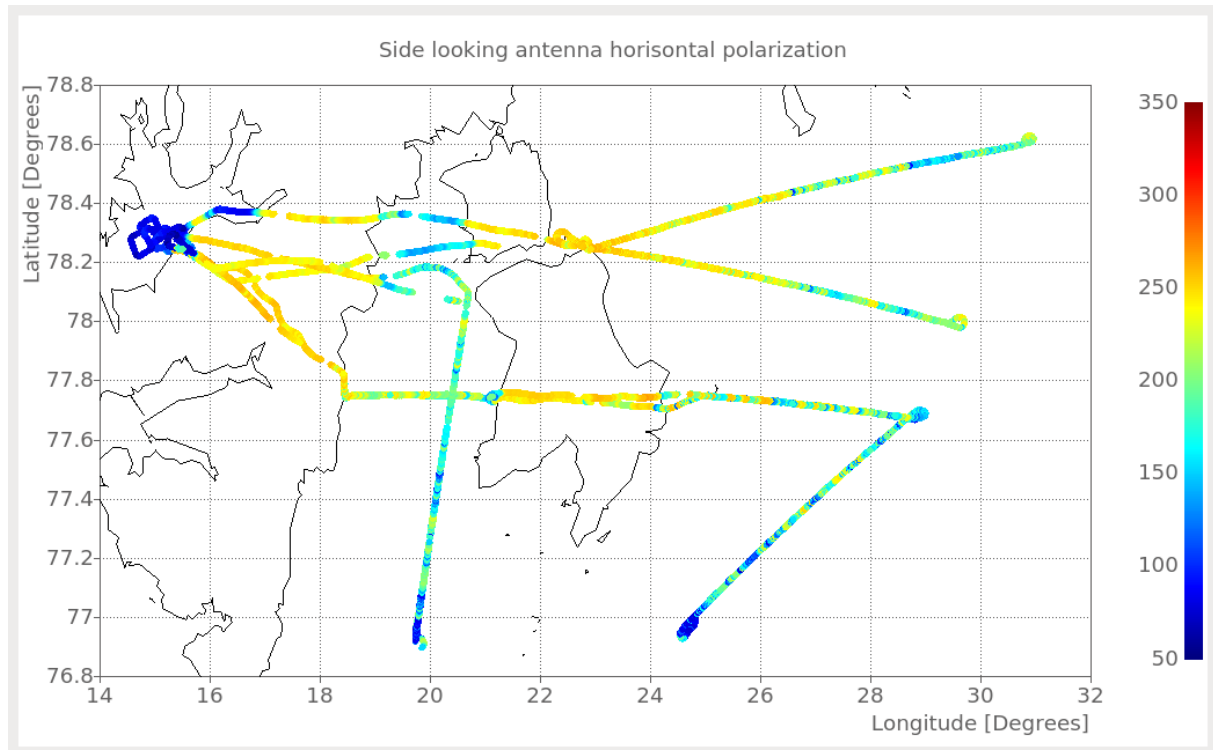


Figure 24: Brightness temperature data, H-pol, side looking

3.2 Airborne Laser Scanner

The derivation of freeboard with a laser scanner involves two processing steps

- 1) Calibration of the instrument mounting position and orientation in the aircraft reference frame using a fixed ground target (e.g. a building)
- 2) The derivation of ellipsoidal (WGS84) surface heights from laser range data and the aircraft attitude and instrument mounting position and orientation.
- 3) Referencing the surface heights to the local sea level by manual classification of sea surface height tie points in leads

Instrument mounting position

The calculation of geolocated ground points of the scanner requires the position of the scanner in the aircraft reference frame and the “squint” angles with respect to the pitch, roll and yaw (y, x, z) axes. All parameters are empirically obtained by minimizing the ground position of a target like a building (e.g. Figure 25) from two perpendicular overflights.

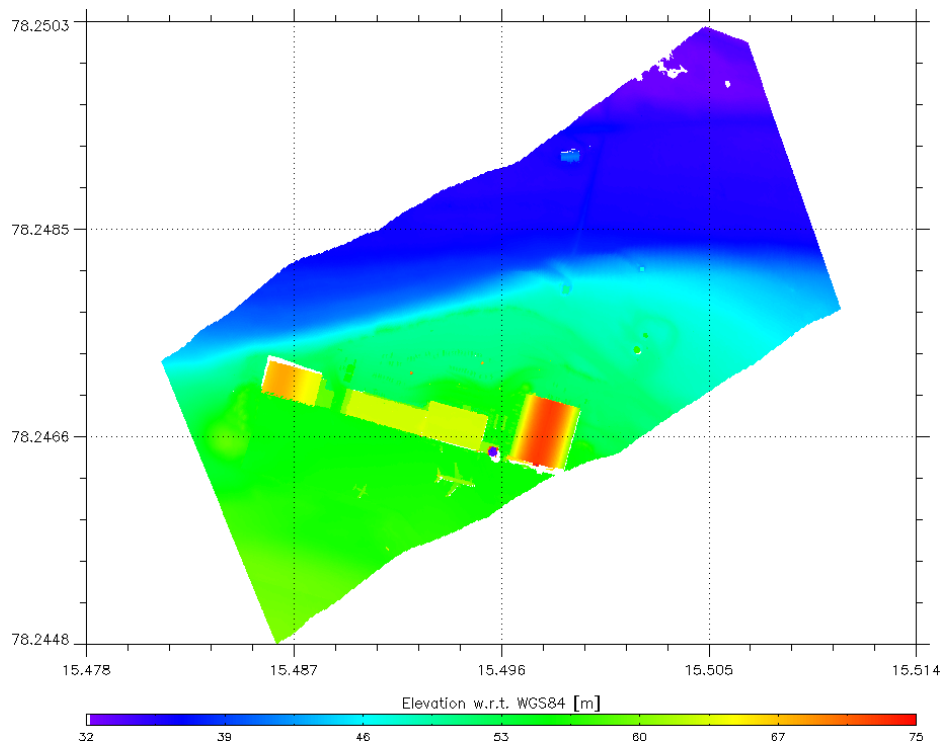


Figure 25: Digital Elevation Model obtained during a calibration cross-over at airport buildings in Longyearbyen

The corresponding mounting positions and angles are given in Table 8.

Table 8: ALS mounting positions and angles during the SMOSice2014 field campaign

ALS Squint X	0.215 deg
ALS Squint Y	0.25 deg
ALS Squint Z	-3.00 deg
ALS POS X	-9.30 m
ALS POS Y	0.44 m
ALS POS Z	0.24 m

Ellipsoidal surface height

The determination of the geographical position and surface height with respect to the WGS84 ellipsoid of the scattering location for each laser shot depend on the

- Location and orientation of the instrument within the aircraft reference frame
- The angle of the laser shot within the swath angular range
- Aircraft position and attitude

Thus a concatenation of several rotation and translation matrices has to be applied to calculate the longitude, latitude and elevation coordinate from the measured laser range.

A detailed overview of the mathematical formulation is given in Helm et al. 2006, (<http://epic.awi.de/21161/>)

Sea Surface Height Classification

The ellipsoidal elevations have to be referenced to the local sea level in order to obtain freeboard from the laser range measurements. The local sea surface height is measured by the scanner only by the elevation of open water or centimetre thin ice in leads between ice floes and has to be interpolated between the leads. In the ellipsoidal reference frame, the sea surface height is influenced by the gravitational pull of the Geoid and dynamic effects, e.g. ocean currents, tides and the inverse barometric effect of atmospheric pressure variations.

The major contribution to sea surface height (SSH) variation can be removed by using a mean dynamic sea surface height product from the ellipsoidal elevations, leaving a minor anomaly in the orders of 10th of centimetres instead if 10th of meters of height variations along a typical laser scanner profile. But due to the fact, that most of the surveys took place in near-coastal areas were a mean dynamic sea surface topography may not be a good approximation and the abundance of leads in the ice cover, a mean dynamic topography was not used as an intermediate processing step towards laser freeboard.

Instead, the leads were manually marked as SSH tie points using a dedicated IDL program (see Figure 26) for laser scanner data in AWI format and a spline interpolation was used to get the along track reconstruction of the SSH in ice-covered areas.

During this process it became clear, that a major part of the surveys took place in areas where ocean swell of variable wave length and magnitude had a significant impact on the surface elevations and thus the freeboard. On the farthest locations from the ice edge, the effect of surface waves was negligible and became more pronounced in magnitude and shorter in wavelength with decreasing distance to the open water. Wave penetration into the ice pack depends on wavelength, thus the first waves observed in the profiles had a period longer than the occurrence of leads and could be theoretically removed from the data by appropriate interpolation (see Figure 27). However, this approach became rapidly unfeasible closer to the ice edge with waves of significant shorter wavelength. Also the SSH classification and interpolation procedure does not allow an across track SSH gradient, therefore the tie points were set at a mean lead elevation throughout all profiles (see Figure 26 and Figure 29)

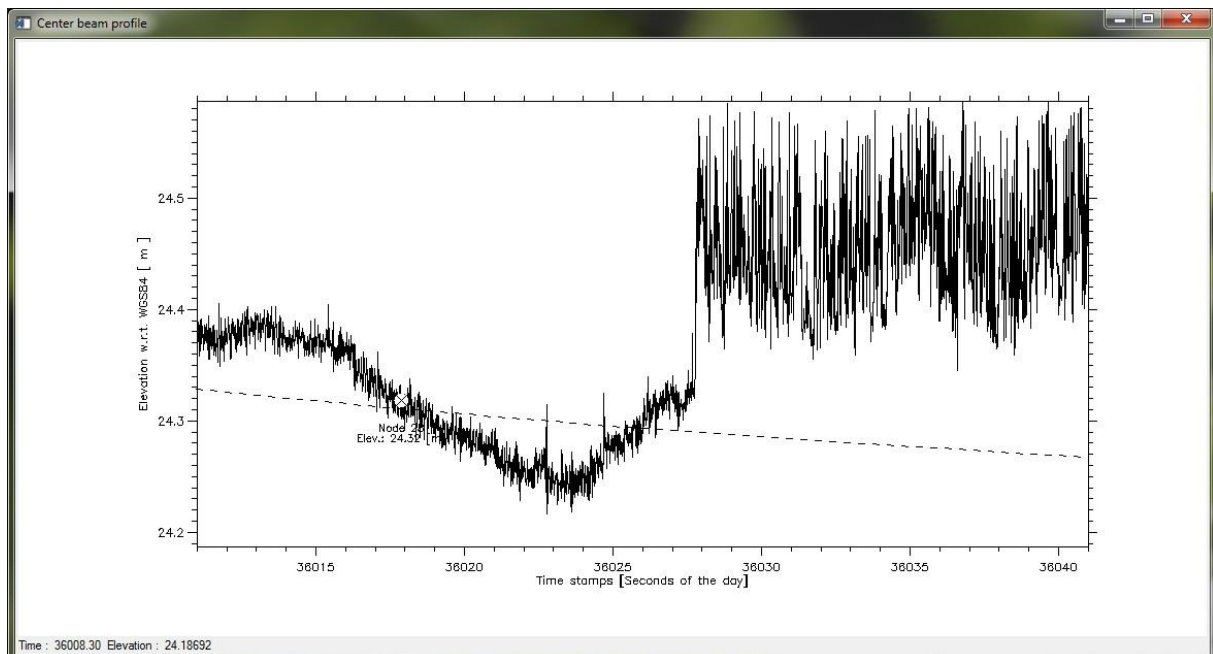


Figure 26: Manual selection of SSH tie points at the mean surface height of leads (screenshot of the manual SSH classification software)

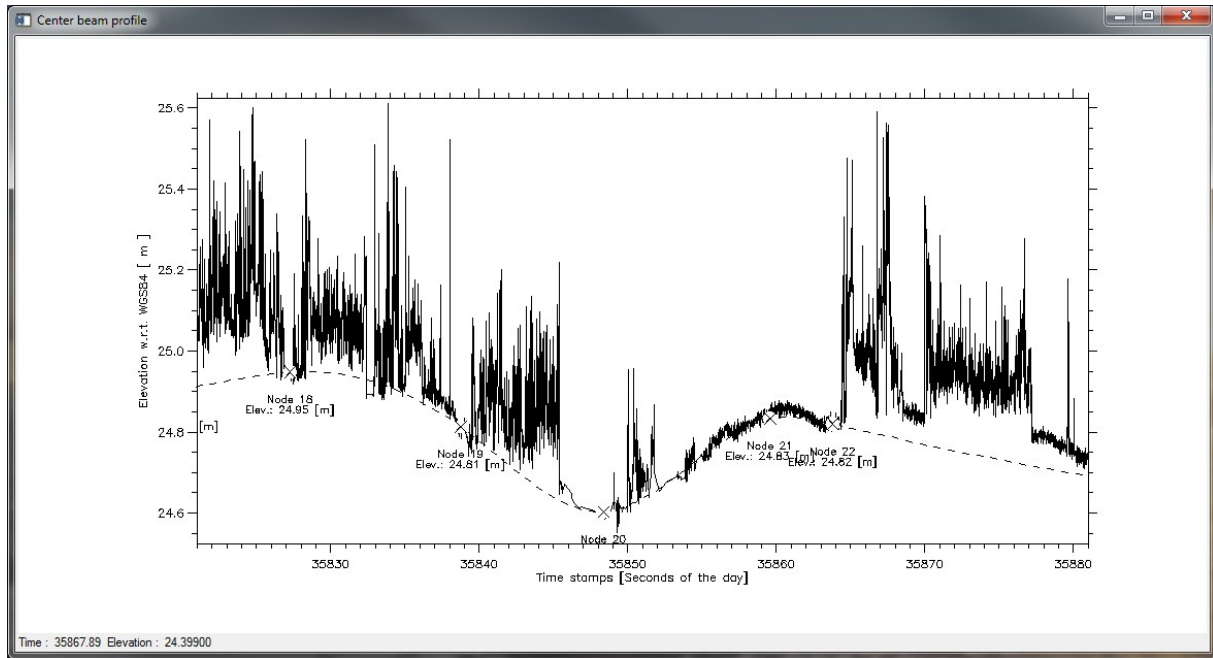


Figure 27: Removal of SSH variations by dense manual classification of SSH tie points. This approach was not used for the final data product.

Laser Freeboard

Substracting the along-track SSH from the WGS84 elevations of each points yields laser freeboard or by definition snow freeboard, as the main scattering horizon of near-infrared laser is given by the snow surface.

The swath freeboard data is delivered in different data products.

1. The raw irregular gridded point cloud of freeboard values, associated with position and timestamp. This dataset contains the full information, were the point spacing depends on the aircraft altitude: ~ 0.25-0.30 cm for 200 feet survey heights and ~ 1 m for 1000 feet survey heights. On demand, the data can be gridded to a regular point spacing. (Example Figure 28)
2. A resampled along-track data set with a resolution of 1 second. Here all data points are averaged, including time stamp and location. The standard deviation of the data within 1 second is included as roughness proxy information. This dataset was produced for the direct comparison with EMIRAD (Example Figure 30).
3. A data set containing only center beam measurements approximately nadir of the aircraft. The purpose of the data set is to serve as a quick look with the full resolution of the laser scanner, but only a fraction of the data volume. (Example Figure 31).

The corresponding data formats of the different laser scanner freeboard products are described in the data inventory section.

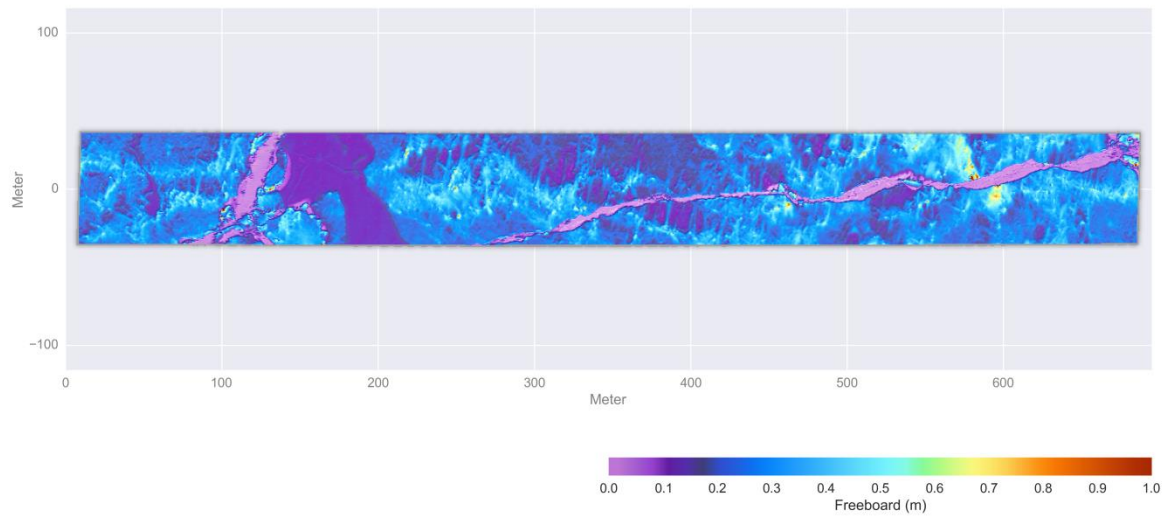


Figure 28: Typical ALS freeboard map at a resolution of 25 x 25 cm.

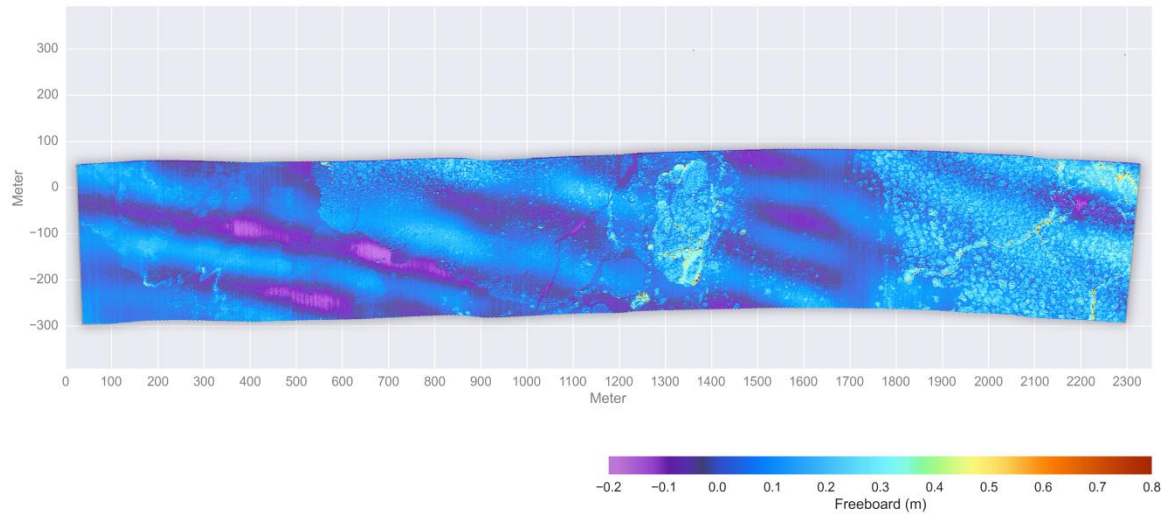


Figure 29: ALS freeboard in ice covered areas with ocean swell

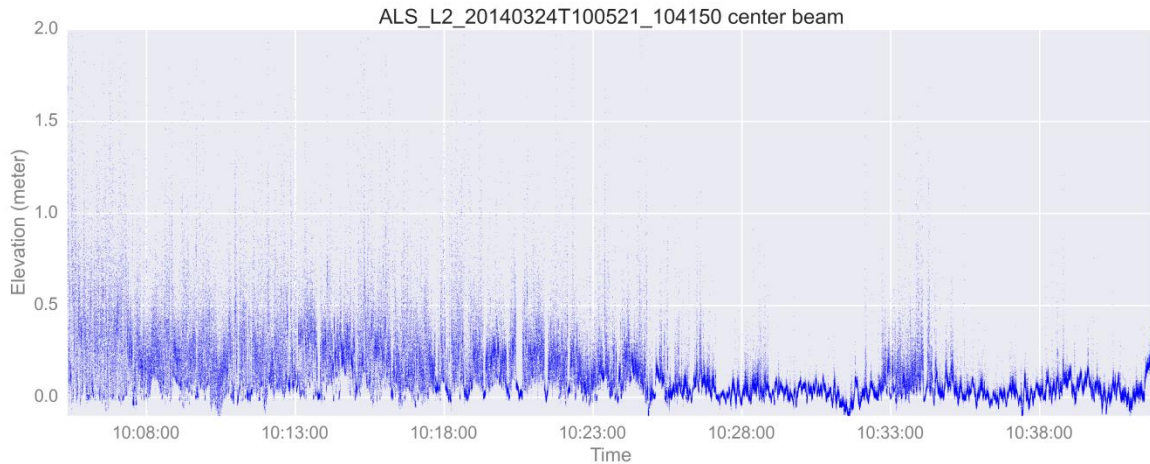


Figure 30: Example ALS freeboard data set derived from the center beam. The profile shows the gradient from thicker deformed sea ice (left) to the thin ice zone surface waves (right)

W

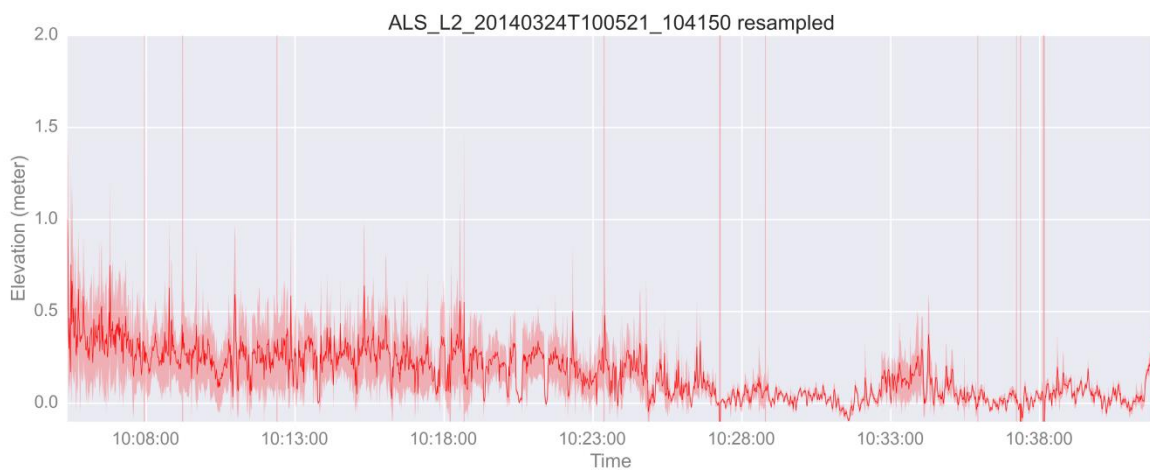


Figure 31: Same example as Figure 30, only with using 1 second mean values over the complete swath. The standard deviation of the 1 second subset is plotted as light red shading.

3.3 Snow Radar

Runway Calibration

For the calibration of cable length, potential datation offsets and the initial verification of the instruments operativeness we compared the range estimates of the snow radar over the runway in Longyearbyen to those of the laser scanner. This calibration target was chosen, due to its long and comparably smooth surface and due to the fact that the tarmac can safely be assumed to be the identical scattering horizon for the laser and the radar.

The first investigation was the estimation of a potential datation offset between the snow radar data acquisition unit and the INS/GPS system by cross correlations of aircraft altitude changes and radar range changes (Table 9). A datation offset was found with a value of 0.595 seconds.

With this offset applied, the range offset between laser scanner and snow radar can be obtained by comparing the corresponding elevations over the runway. For this comparison, the digital elevation model of the runway was regredded to the location of the radar footprint locations. Because the runway is a smooth surface, no exact footprint weighting was applied. The digital elevation model and the resulting comparison is shown in Figure 32 and the values are summarized in Table 9.

Table 9 : Summary of snow radar calibration of the runway in Longyearbyen

Range Correction Snow Radar	3.96 m
Datation Correction Snow Radar	0.595 sec
Post correction Laser-Radar Offset	0.03 m +/- 0.49 m (mean +/- standard deviation)

Using the calibration values shows a reasonable good agreement between the mean difference in elevation of the laser and the radar over the runway. However, the standard deviation is quite high, almost 0.5 m, already indicating smaller scale variability in radar range, which also can be seen in Figure 32.

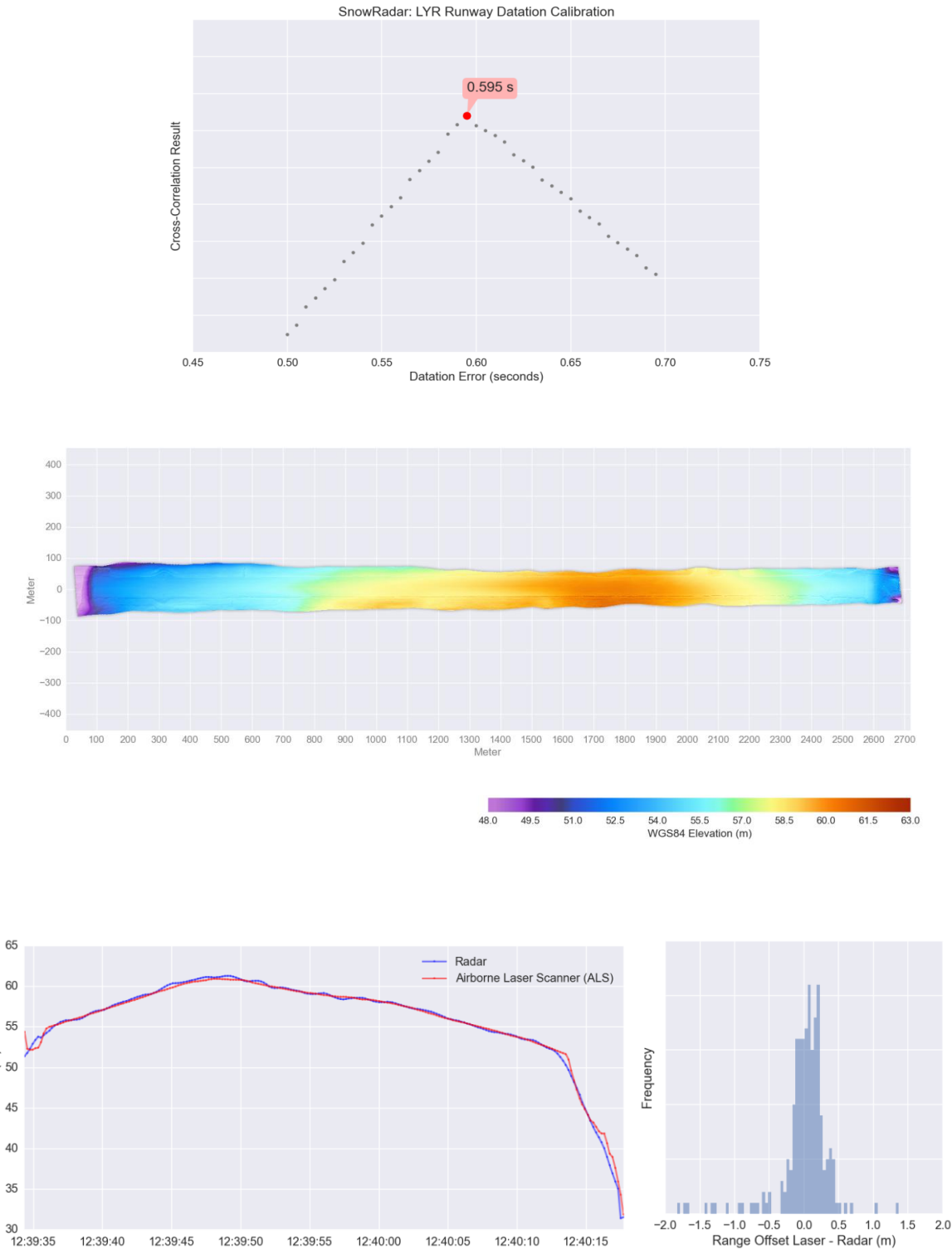


Figure 32:

top panel: Cross Correlation between changes in aircraft GPS altitude and snow radar range for the estimation of the datation offset of the snow radar data acquisition system

middle panel: Digital elevation model from the laser scanner

lower panel: Ellipsoidal altitude of laser scanner and snow radar for the radar footprint after correction of datation error and cable offset (left) and offset histogram between laser scanner and snow radar (right)

Sea Ice Example

Further analysis of the elevation obtained from the retracked snow radar data revealed an unrealistically high variability that could not be linked to any surface features in the laser digital elevation models. Figure 33 shows an example of surface elevations from the laser altimeter and the snow radar. The snow radar range data were corrected with the offset obtained from the runway calibration.

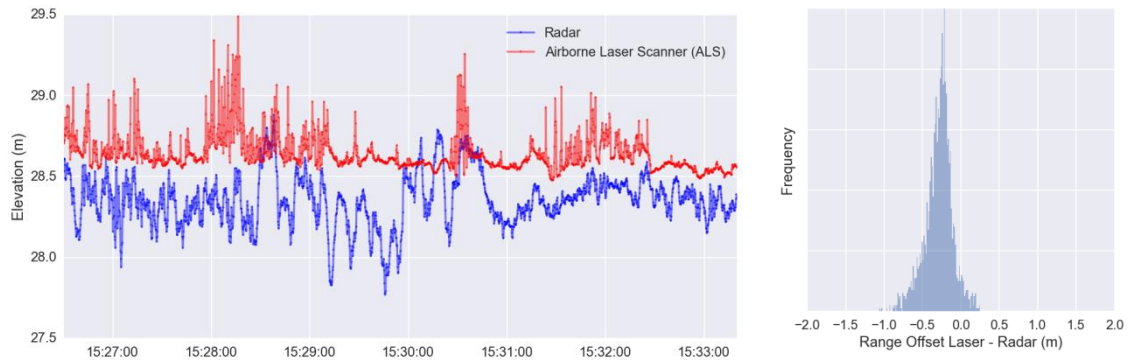


Figure 33: Example of snow radar data over sea ice. Comparison to ALS laser altimetry (left) and offset histogram (right)

The histogram of the offset (Figure 33) shows that the snow radar elevations were on average 0.28 m below the laser elevations with a median difference of 0.26 m and a standard deviation of 0.17 m for this particular example. The conversion of range difference into snow depth still requires a geometric correction for the lower wave propagation speed of the radar waves in snow by approximately a factor of 0.33. The result would yield a reasonable snow depth, however due to the visible variability in the snow radar range estimates it is assumed that the derived mean range differences do not represent the real snow situation.

The analysis of this poor behavior of the sensor will require work which cannot be completed in the timeline of the SMOSice 2014 project. It was therefore decided that a preliminary geophysical data product will not be part of the official data release. A continuation of the processing of the snow radar data at the Alfred Wegener Institute is nevertheless intended.

3.4 Airborne EM

In total eight EM-bird helicopter flights were performed from R/V Lance during the IRO-2 cruise between 19 and 26 March 2014. The table below lists some more details. Two flights on 20 March underflew Cryosat-2 tracks. Two of the flights, on 24th and 26th March, were done in conjunction with the Polar-5 overflights.

Table 10: List of EM-Bird flights during the IRO-2 cruise. Times are UTC.

Date	Start Time	Stop Time	Start lon/lat	Stop lon/lat	Comment
19/03/2014	14:50	15:42	31.90°/78.49°	31.75°/78.48°	
20/03/2014	08:52	11:03	26.40°/78.37°	26.45°/78.36°	CryoSat underflight
20/03/2014	14:23	16:28	26.28°/78.32°	26.16°/78.24°	CryoSat underflight
22/03/2014	08:32	10.52	31.13°/78.42°	30.55°/78.44°	
22/03/2014	13:51	15:55	29.14°/78.50°	28.69°/78.54°	
23/03/2014	12:45	13:56	25.73°/77.37°	26.03°/77.36°	
24/03/2014	10:39	13:16	29.32°/78.00°	29.37°/77.99°	With Polar-5
26/03/2014	11:06	13:17	26.30°/77.26°	26.05°/77.21°	With Polar-5

The raw EM-Bird measurements are processed using scripts (IGOR Pro and C) mainly developed at AWI. The processing contains some manual steps to remove the instrument drift during the measurements and define the zero ice thickness level. To avoid bad data the processing routine automatically removes data outside minimum & maximum thresholds in laser height, and data that coincide with a change in heading (to avoid roll events on change of direction). Other small gaps in the data occur due to GPS dropout and to the laser on our EM-Bird failing over open water. The nominal sea ice thickness (snow plus ice thickness) uncertainty for a single measurement is 10 cm for level ice [Haas et al., 2009]. For ridges significant larger errors can occur. Averaged over the EMIRAD footprint size uncertainties of less than 10 cm can be assumed.

All EM-Bird data has been processed and sea ice thickness measurements with collocated GPS positions are available. Table 11 contains the mean & mode thickness for each flight. Figure 34 shows an overview of EM-Bird ice thickness for all eight flights obtained during the IRO-2 cruise.

Figure 37 shows the ice thickness histograms for all flights combined and Figure 37 shows the ice thickness histograms for the all EM-Bird flights individually. There is a distinct gradient in ice thickness from thicker ice in the west, close to Svalbard, and thinner ice to the east. Figure 36 plots ice thickness against longitude to visualize the thickness gradient.

Table 11: Mean and modals thickness obtained from airborne EM flights F1 to F8 with the EM-Bird

	New mode (m)	New mean (m)
F1	0.5	0.4
F2	0.8	0.9
F3	1.1	1.1
F4	0.6	0.5
F5	0.3	0.6
F6	0.5	0.4
F7	0.6	0.8
F8	0.2	0.5
All	0.5	0.7

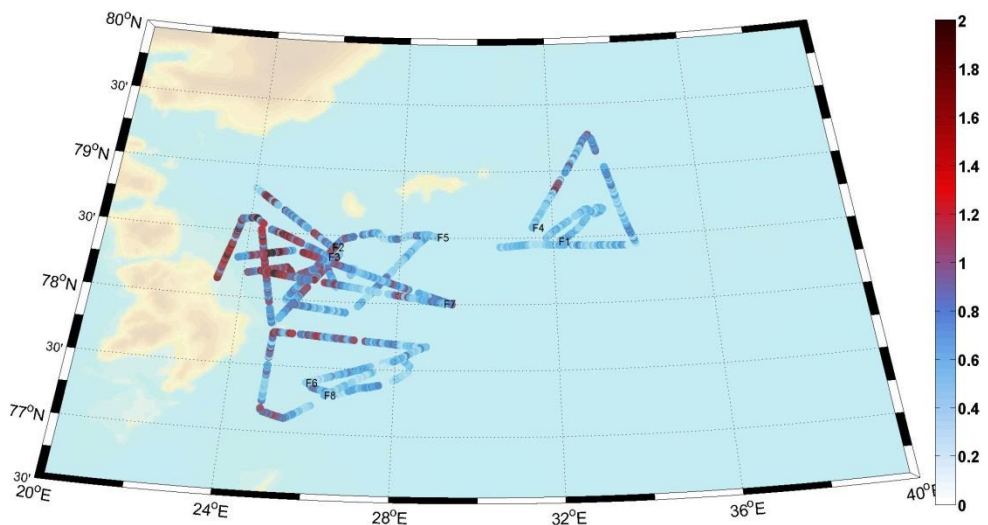


Figure 34: Map of ice thickness, 1km average, (m) for all EM-Bird flights from RV Lance.

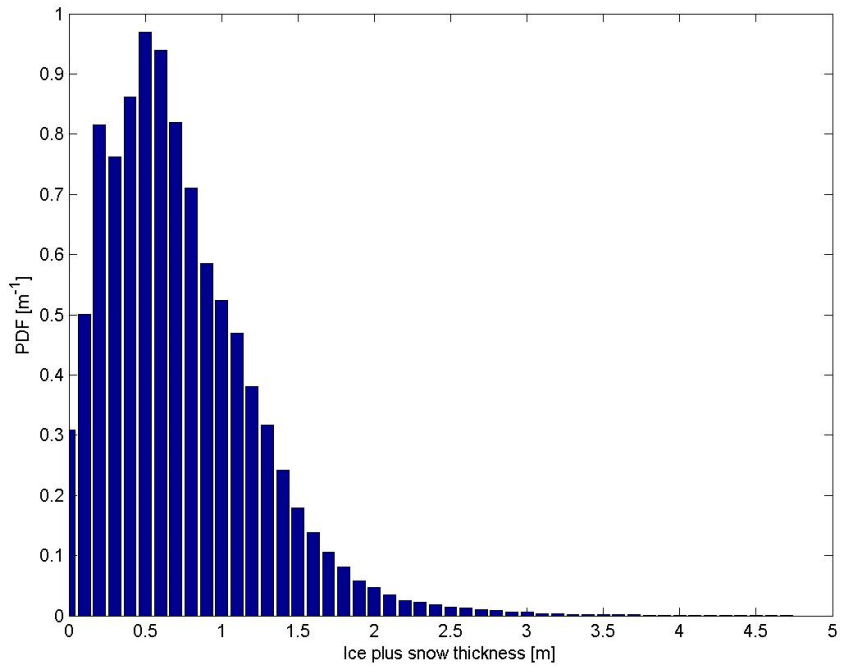


Figure 35: Ice thickness histogram for all flights combined.

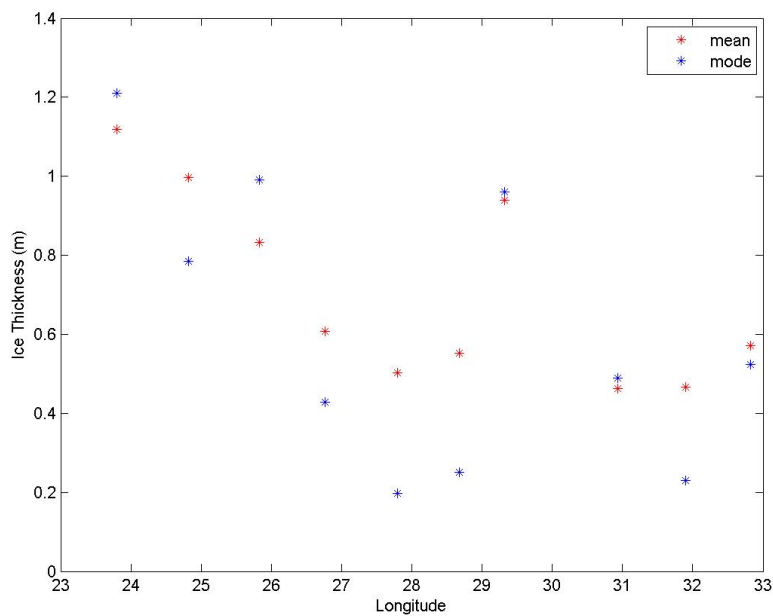


Figure 36: Scatter plot of thickness (mean and modal) vs. longitude

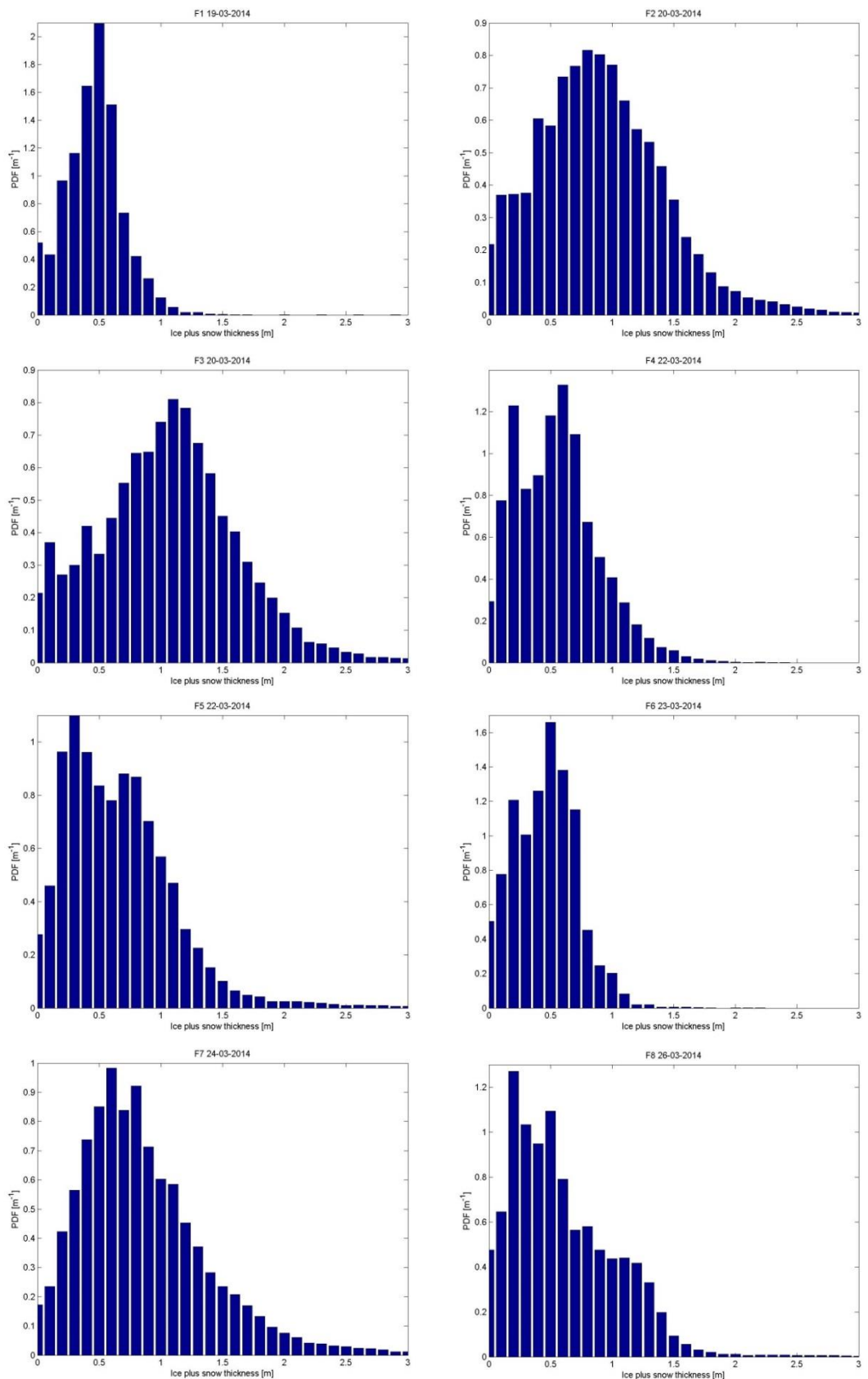


Figure 37: Individual thickness histograms from EM-Bird surveys F1 to F8

3.5 Auxiliary Aircraft Sensors

KT19 surface temperature

Polar-5 is equipped with a Heitronics radiation pyrometer of type KT19.85II. The digital output of the instrument is used as surface temperature, although measurements are performed under the assumption of a constant surface emissivity of 1.

Radiation Sensors

Raw data sets of the pyrgeometer and pyranometer are processed by applying calibrations of the sensitivity of the instruments. Calibrations are regularly performed at the Physikalisch-Meteorologisches Observatorium Davos, World Radiation Center. To calculate longwave radiation flux densities, the body temperature of the pyrgeometers has to be taken into account additionally.

As the radiation sensors are mounted at the aircraft in a fixed position, shortwave irradiances are only calculated for clear-sky conditions. Data of the upward facing pyranometer, which receives direct solar radiation, is corrected for the misalignment of the instrument as well as the roll and pitch angles of the aircraft to derive downwelling hemispheric radiation flux densities for horizontal exposition of the sensor.

Aerial Photography

The raw images of the photo camera are converted into jpeg files with corrections for lens distortion and vignetting. The geographical position and the GPS timestamp is stored in the EXIF tags of the images.

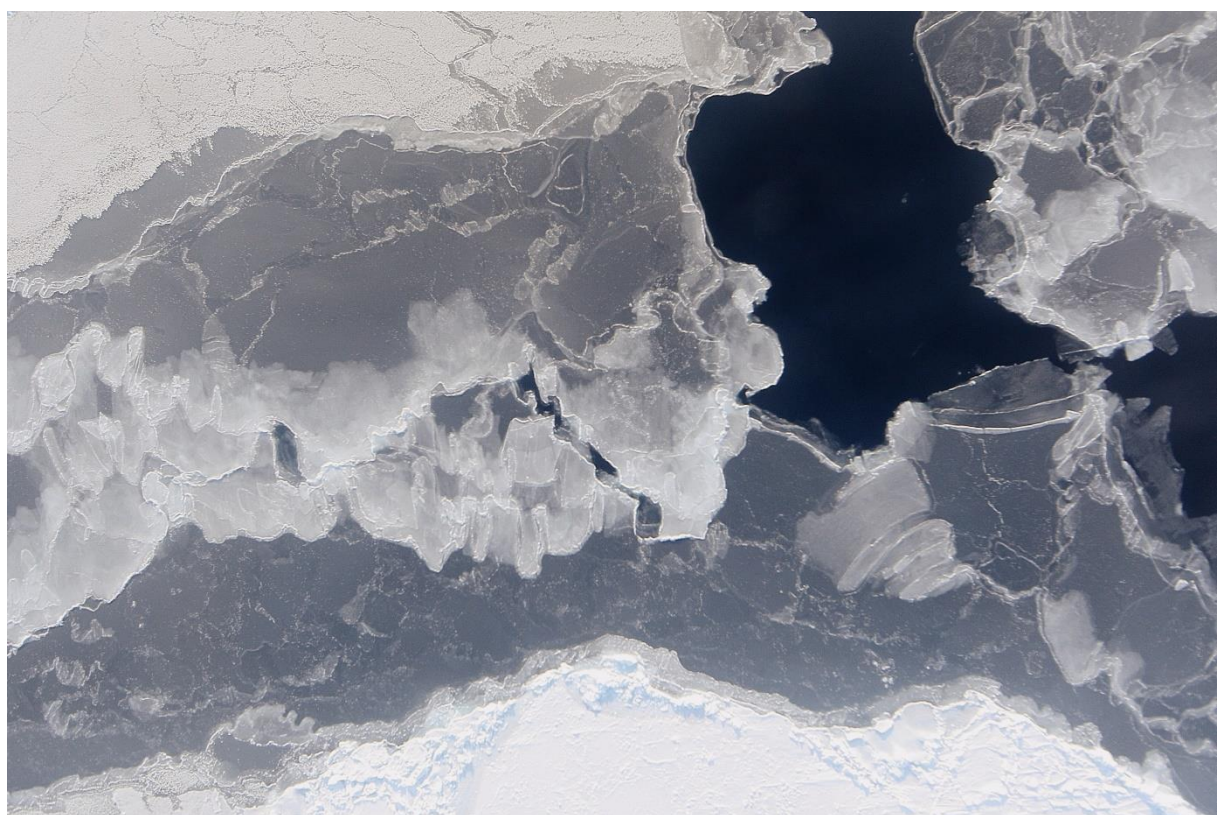


Figure 38 : Example image of the nadir photo camera in Polar-

4 Preliminary Results

In the following we compare ALS, EMIRAD and SMOS brightness temperature (TB) and sea ice thickness data. We here restrict the analysis on two tracks flown on 24 March 2014 (Figure 39). These cases include a strong gradient from thick deformed ice to thin ice and are thus suitable to assess the performance of the instruments and to verify the L-band retrieval of thickness.

A more detailed analysis is subject of the ongoing STSE SMOS+ Sea Ice project and beyond the scope of this campaign data report. In particular a comparison to Helicopter and ship-based measurements is more difficult because of the spatio-temporal difference, the different footprints, and the sea ice drift. A comparison of ALS and EMIRAD data has the major advantage that the measurements were performed simultaneously, and, in case of the nadir EMIRAD data, with the same field of view. Therefore, any L-band retrieval of sea ice thickness has first to pass the test with the now available coincident ALS data otherwise it could falsify the theory. It should be stressed that previous comparisons of airborne measurements of sea ice thickness and L-band TBs had strong limitations and yielded only relatively weak correlations for selected tracks.

The analysis is structured as the follows: at first we compare the ALS thickness against the two existing SMOS sea ice thickness products. Secondly, we derive the thickness from EMIRAD brightness temperature and compare this to the ALS thickness. Finally we look at the brightness temperatures from SMOS and EMIRAD.

4.1 ALS and SMOS thickness

In the following we use a Level 3 product derived from the ALS DEM, the averaged freeboard along the cross-track. The ALS freeboard data are resampled to one second and one minute by taking the arithmetic mean value.

To estimate the ice thickness from the freeboard one has to make some assumptions about the density of ice and snow and the snow thickness. Because no reliable information about the snow thickness is available we here use the simple parameterization $h_s = 0.1 * h_i$, with the snow thickness h_s and ice thickness h_i . We assume a snow density of 300 kg/m^3 and a typical density of first year ice as 910 kg/m^3 . This resulting factor of 5.5 is used to estimate the ice thickness from the ALS freeboard measurement. The assumption of a snow-free ice surface would result in a conversion factor of about 9. This calculation can be seen as a first rough error estimate of the ALS thickness retrieval: with the assumption of a snow free ice surface we obtain a maximum observed sea ice thickness of about 4m (one minute average). It reduces to about 2m with the assumption of the snow thickness as 10% of the ice thickness.

For the following comparison we use the two existing SMOS sea ice products of the University of Hamburg (UH) and University of Bremen (UB). Both products have been obtained from the according websites and no modifications have been applied. Thus, they represent the retrieval algorithms as described in Tian-Kunze et al. (2014) and Huntemann et al. (2014). Figure 39 shows the two tracks flown on 24 March 2014 with the UH SMOS sea ice product color-coded in the background. The UB product (map not shown) has similar patterns. Figure 40 shows the profiles of the two Polar 5 tracks with the ALS thickness data

interpolated on the 12.5 km grid of the SMOS products. It can be seen that the gradients of the thick ice region at the coast of Edgeøya is well captured in the UH product. The ice thickness of the UH product is underestimated by about 50% with respect to the ALS thickness. SMOS and ALS agree well within the range of their uncertainty. The UB product is limited to thickness values below half a meter and underestimates the thickness with respect to ALS and the UH product.

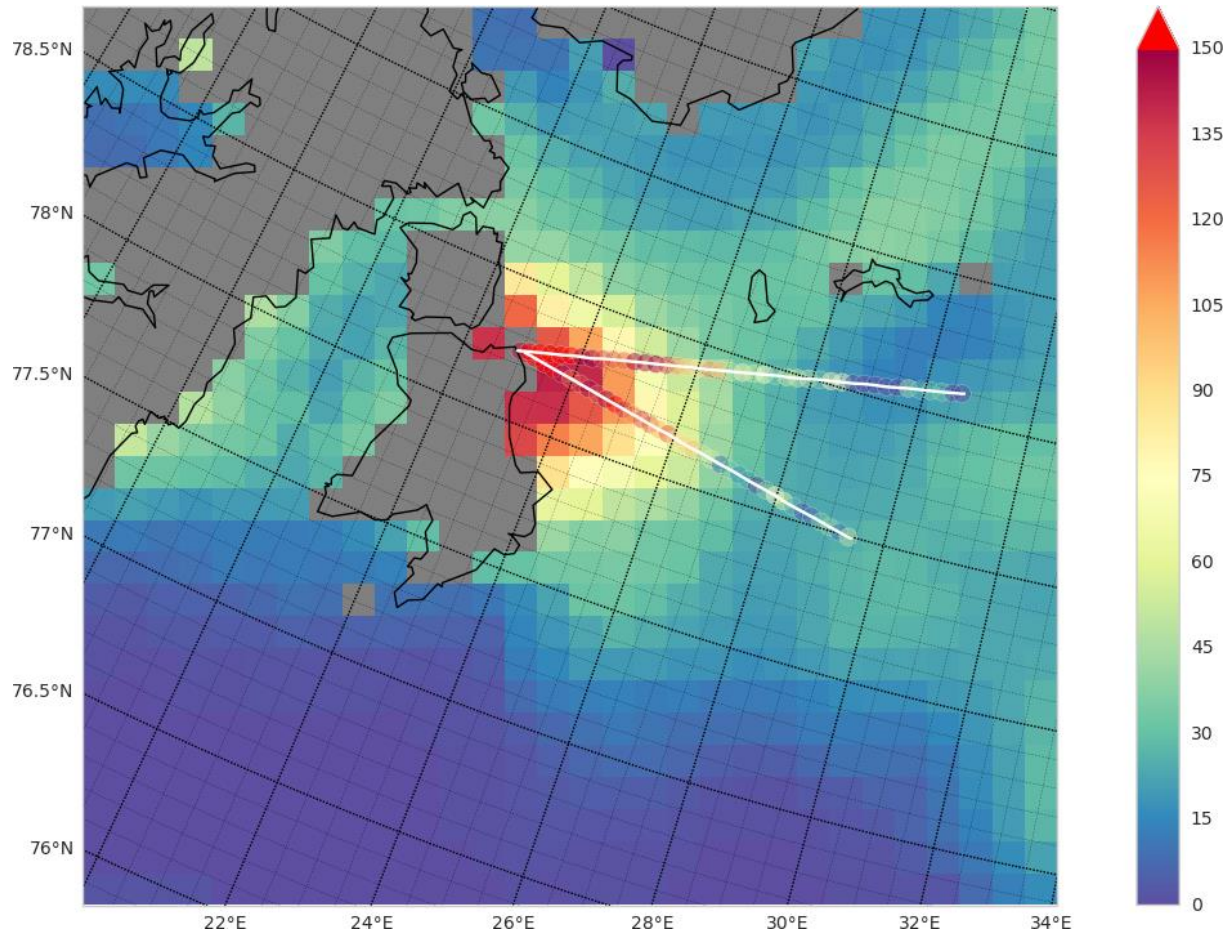


Figure 39 SMOS sea ice thickness (UH product) and ALS ice thickness on 24. March 2014.

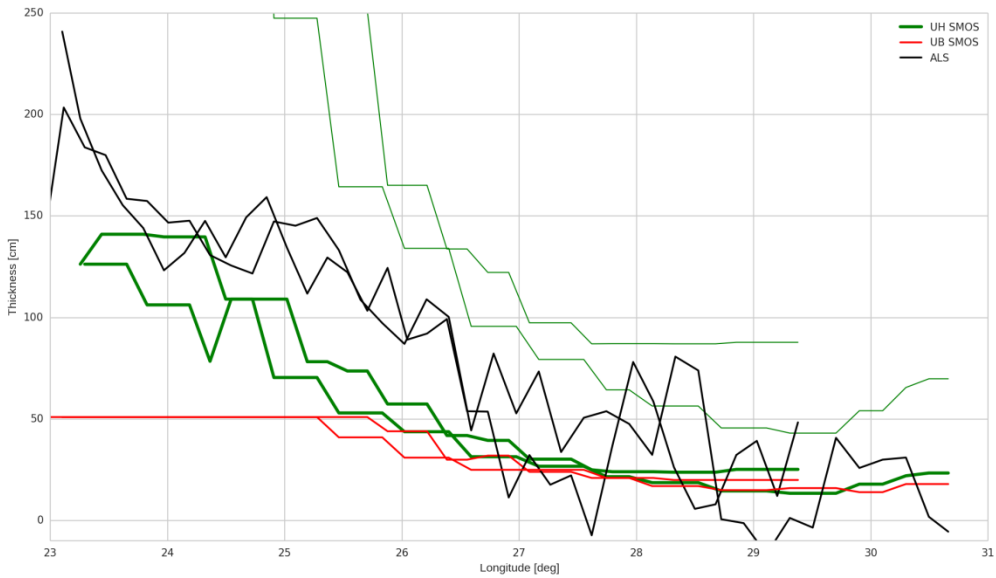


Figure 40 ALS and SMOS ice thickness along the track shown in Figure 39. Two different SMOS sea ice products are compared. The sea ice thickness uncertainty as provided in the UH product is shown with the thin green line. The UB product does not include an uncertainty.

4.2 ALS and EMIRAD thickness

In the following we use an empirical fit to estimate the ice thickness from the nadir look EMIRAD TBs. The retrieval fit equation $TB(x)=T_1-(T_1-T_0) \exp(-k x)+a x$ is inspired by the usual Beer-Lambert type of exponential relation plus a linear term which may reflect the thermal influence of a snow cover. Figure 41 shows the relation of ALS ice thickness and EMIRAD brightness temperature (one minute averages) compared to the more complex UH SMOS retrieval algorithm for this particular date and region. The empirical function is used in the following because of its simplicity and no further need of auxiliary data. The retrieval tie points T_0 , T_1 and parameters k and a have been selected by a visual fit to the EMIRAD data and are kept as constants for all flight tracks analyzed

Figure 42 and Figure 43 show time series of ALS and EMIRAD ice thickness and according brightness temperatures. A scatterplot of ALS and EMIRAD ice thicknesses is shown in Figure 44. The correlation coefficient $r=0.92$ confirms the empirical relation of ice thickness and L-band brightness temperature. When averaged to three minutes the correlation increases to $r=0.96$ (not shown). The other flight tracks (not shown) show similar results but with larger differences in the marginal ice zone due to the effect of waves.

With this strong empirical evidence we can conclude that L-band brightness temperatures indeed carry information about the sea ice thickness. The data suggest that the empirical relation is even valid up to about 2 m thickness. This fact warrants further physical explanation.

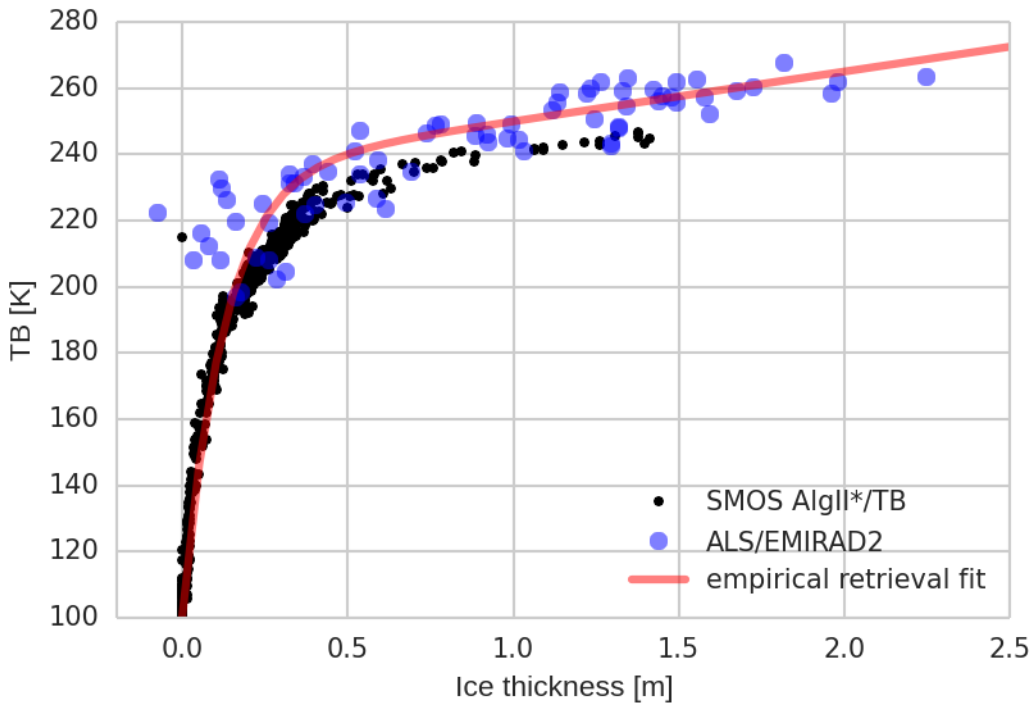


Figure 41: Relation of brightness temperature and sea ice thickness. The blue dots represent the ALS thickness and EMIRAD TBs as shown in the Figures before. The values for the black dots are taken from the UH sea ice thickness product.

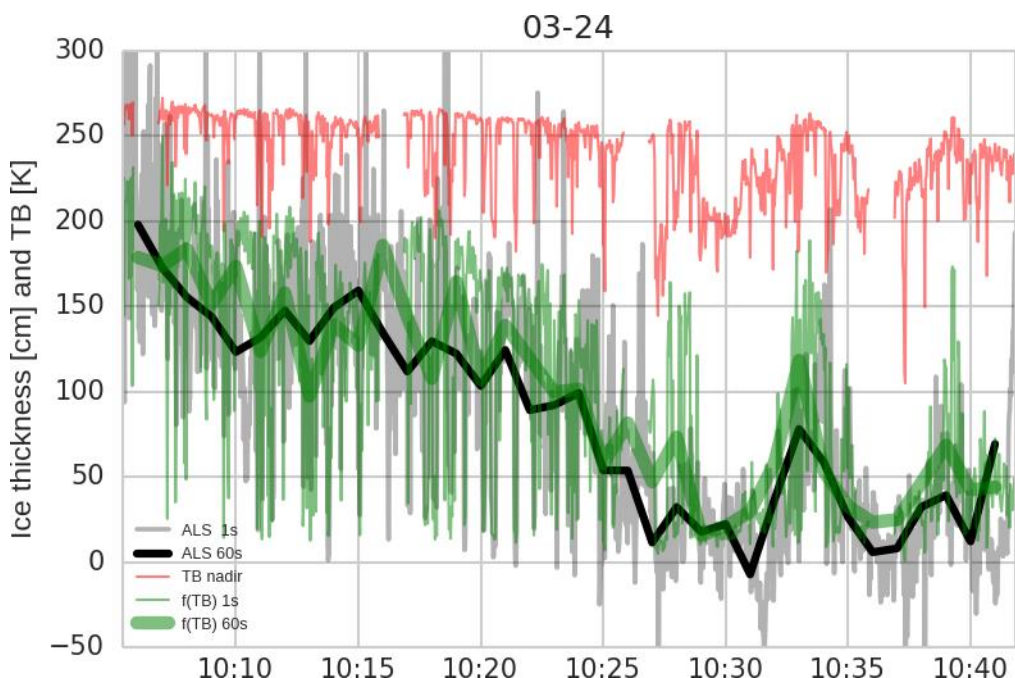


Figure 42: Thickness derived from ALS and EMIRAD brightness temperatures. The thin lines indicate one second averages while the thick lines are averaged over one minute. The EMIRAD brightness temperature used for the calculation is shown in red.

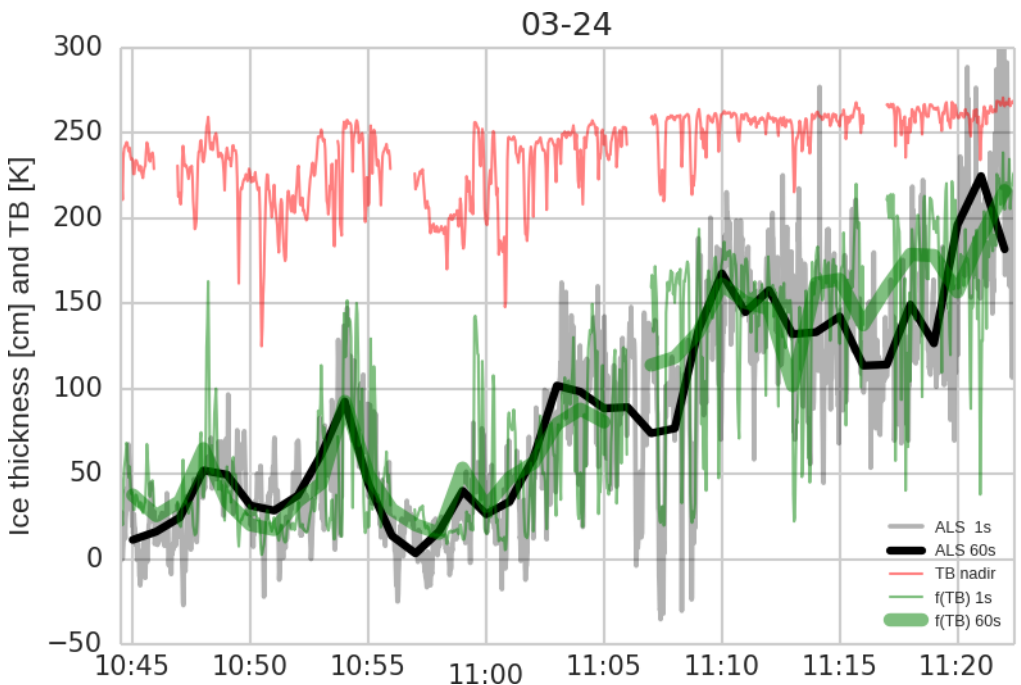


Figure 43: Description same as Figure 42.

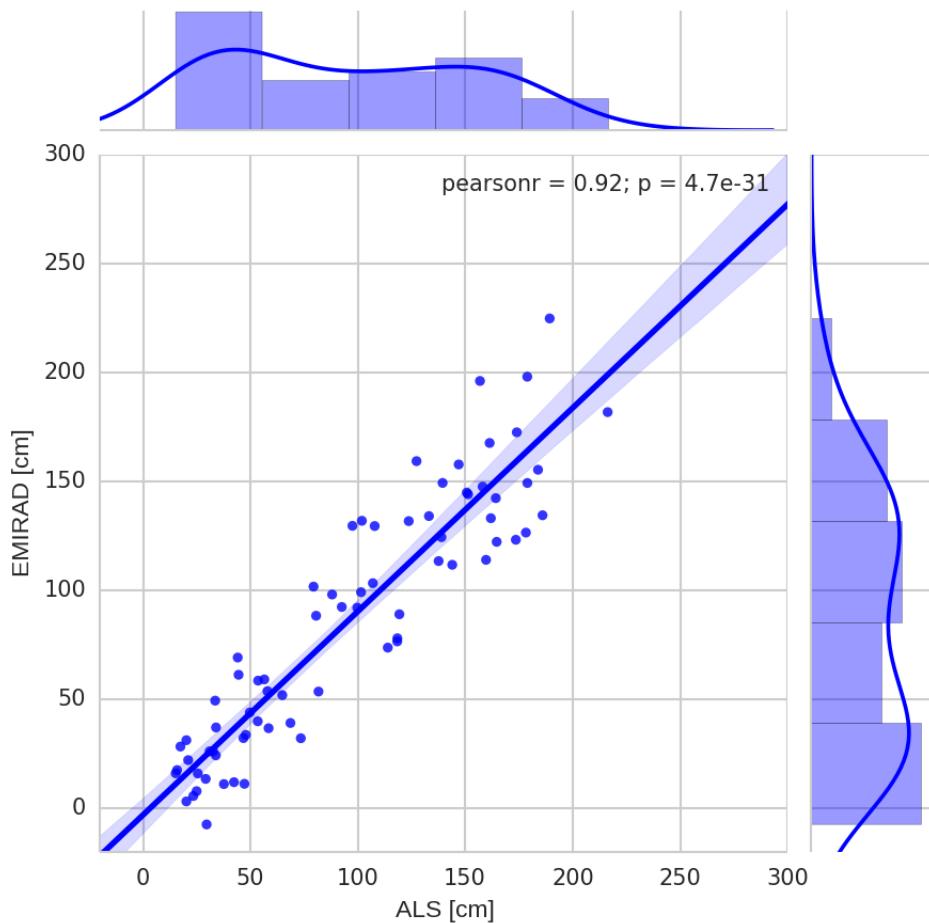


Figure 44: Scatterplot of ALS and EMIRAD thickness (one minute averages) for the tracks shown in Figure 42 and Figure 43.

4.3 EMIRAD and SMOS brightness temperatures

Finally we compare the EMIRAD TBs with SMOS. Here we use the UH TB product which is an average of all intensities (first stokes) over the incidence angle range between 0 and 40 degrees. Figure 45 shows TB profiles obtained from EMIRAD and SMOS for the tracks shown in the map (Figure 39). Data from both antennas (nadir and side looking) are used for the comparison. There is an obvious bias between SMOS and EMIRAD while the overall pattern agrees well. SMOS consistently shows 15-10 K smaller TBs as compared to EMIRAD. The difference is greater for nadir than for the side-looking horn.

An explanation for this difference may be the coarse resolution of SMOS and the spot-like pattern of thick ice surrounded by thinner ice and open water. Comparisons for other tracks show indeed smaller differences (not shown). However, further work is necessary to explain the bias.

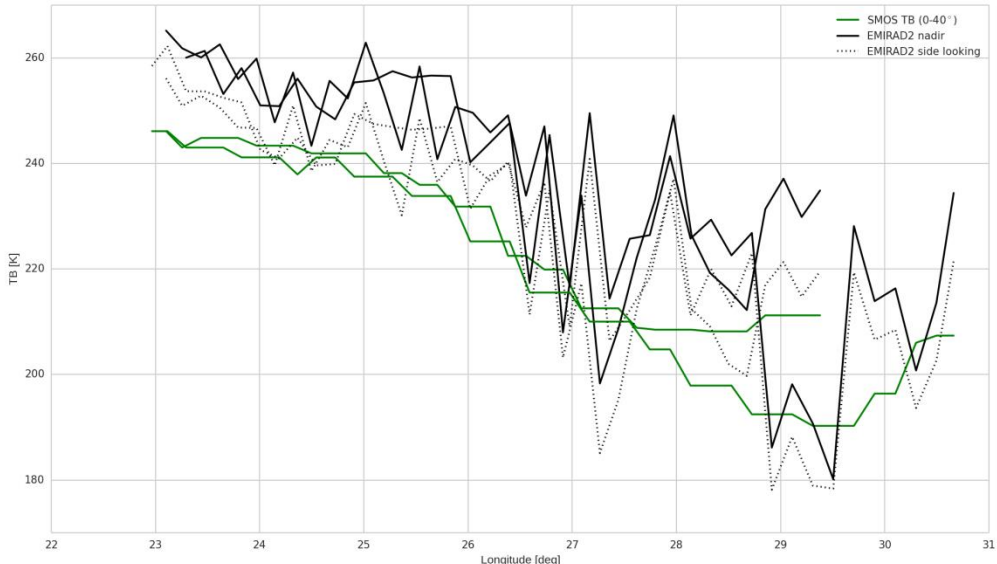


Figure 45: Brightness temperature from EMIRAD and SMOS for the tracks shown in Figure 39.

5 Summary

Preliminary analysis of the data acquired from the SMOSice2014 field campaign proved the worthiness of the region for SMOS cal/val studies and highlighted directions for further investigations. The key findings can be summarized as follows:

1. A bias of 15-10 K has been identified between the L-Band brightness temperatures of SMOS and the validation measurements by EMIRAD
2. Comparisons of the L-Band brightness temperatures of EMIRAD and collocated sea-ice thickness estimates from airborne laser scanner data give strong empirical evidence that brightness temperatures can be used to estimate sea ice thickness on a significant thickness range.
3. All data sources, SMOS, EMIRAD, ALS and EM-Bird show the same geographical patterns of sea-ice thickness, however with different magnitudes due to the characteristics of the retrieval methods.
4. The comparison of direct sea-ice thickness measurements by the EM-Bird to the aircraft validation data requires a more detailed analysis due to differences in the spatio-temporal scales and sea ice drift between the data acquisitions.
5. Not intended, but the freeboard swath data of the laser scanner may be used to study wave propagation into the ice cover.
6. The quality of data from the AWI snow radar did not meet the expectations and subsequently a geophysical data product from the snow radar with sufficient quality cannot be provided at the time of project closure.

6 Acknowledgements

We thank the pilots Kirk Allen and John Gilmore of Ken Borek Air Ltd. for their professional support on day with and without flying conditions. Aircraft surveys as for this project crucially depend on logistical support (Heinz Finkenzeller, FinkCAS) and the technical assistance by the science-support team (M. Sellmann [AWI] and Dr. J. Kässbohrer [Fielax]).

7 References

Helm, V. , Hendricks, S. , Göbell, S. , Rack, W. , Haas, C. , Nixdorf, U. and Boebel, T. (2006): CryoVEx 2004 and 2005 (BoB) data acquisition and final report , Alfred Wegener Institute, Bremerhaven, Germany. hdl:[10013/epic.34417.d001](http://hdl.handle.net/10013/epic.34417.d001)

Haas, C.; Lobach, J.; Hendricks, S.; Rabenstein, L. & Pfaffling, A. Helicopter-borne measurements of sea ice thickness, using a small and lightweight, digital EM bird Journal of Applied Geophysics, 2009, 67, 234-241

Hendricks, S. , Steinhage, D. , Helm, V. , Birnbaum, G. , Skou, N. , Kristensen, S. S. , Søbjærg, S. S. , Gerland, S. , Spreen, G. , Bratrein, M. and King, J. (2014), SMOSice 2014: Data Acquisition Report, hdl:10013/epic.45054 <<http://hdl.handle.net/10013/epic.45054>>

N. Skou, S. S. Søbjærg, J. Balling, and S. S. Kristensen: "A Second Generation L-band Digital Radiometer for Sea Salinity Campaigns", Proceedings of IGARSS'06, 4p., July 2006.

N. Skou, S. S. Søbjærg, J. Balling, S. S. Kristensen, and A. Kusk: "EMIRAD-2 and its use in the SMOS Cal/Val Campaign", DTU Space, AR 502, pp. 1-59, June 2010.

N. Skou, S. Misra, J. E. Balling, S. S. Kristensen and S. S. Søbjærg: "L-band RFI as Experienced during Airborne Campaigns in Preparations for SMOS", IEEE Trans. on Geoscience and Remote Sensing, Vol. 48, No 3, March 2010, pp1398-1407.

Appendix

8 Data Inventory

8.1 Data Structure

The data files are organized in a folder structure sorted by instrument with an overview given in Table 12.

Table 12: Folder structure of data delivery

Sensor	Folder Name	Subfolders	Comments
Laserscanner	als	Folder each Polar-5 survey with subfolders L1B: WGS84 elevation swath files L2: Freeboard swath files and ssh tie points L3: Resampled freeboard data	several profiles per survey
EM-Bird	em_bird	None	One file per flight
EMIRAD	emirad	Sub-folders for different processing steps: 1) With offset correction a) 1 second data i) No RFI correction ii) With RFI corrections b) 100 msec data i) No RFI correction ii) With RFI corrections 2) Without offset correction a) 1 second data i) No RFI correction ii) With RFI corrections b) 100 msec data i) No RFI correction ii) With RFI corrections	
KT19	kt19	Folder each Polar-5 survey	
Nadir Images	photocamera_downwards	Folder each Polar-5 survey with raw images Subfolder: jpeg	
Pyrgeometer	pyrgeometer	Folder each Polar-5 survey	

8.2 EMIRAD

Section 11 provides a list of the data files constituting the processed output of the EMIRAD-2 radiometer from the SMOSice Campaign March 2014. There are separate files for the nadir (e61) and side looking antennas (e62). All files contain both radiometer and navigation data.

All data files are provided in a total of eight versions, representing 100 ms and 1 s integration times, and with/without correction for antenna frame rotation and CW type RFI, respectively. Data file names are identical for the eight cases, while folder names characterize the actual processing setup. Top folder names are “Delivered data – without offset correction” and “Delivered data – with offset correction”, referring to the original data set and the data set, which has been adjusted in order to correct for the CW type of RFI, according to section 4.8. Inside each folder, four subfolders are found. Table 13 outlines the combinations.

Table 13: SMOSice campaign EMIRAD-2 data processing versions

Folder name	Integration time	Correction for antenna frame rotation
Svalbard data - 1 s	1 s	Yes
Svalbard data - 100 ms	100 ms	Yes
Svalbard data - 1 s - no corrections	1 s	No
Svalbard data - 100 ms - no corrections	100 ms	No

Data format

Data is provided as ASCII files with 14 columns each. All data files follow the naming convention “xxxhhmm0.zzz” where

xxx = day of year

hh = Hour at start of measurement (UTC)

mm = Minute at start of measurement (UTC)

zzz = File type, which can be one of the following:

e61 : Calibrated data from nadir antenna

e62 : Calibrated data from side-looking antenna

The content of each column is given in Table 14.

Table 14: Contents of each column for file types e61 and e62.

Column	Definition
1	Measurement time, UTC [UNIX time, seconds] (http://en.wikipedia.org/wiki/Unix_time)
2	Vertical TB [Kelvin]
3	Horizontal TB [Kelvin]
4	3rd Stokes parameter [Kelvin]
5	4th Stokes parameter [Kelvin]
6	Aircraft position latitude [degrees]
7	Aircraft position longitude [degrees]
8	Aircraft altitude [m]
9	Aircraft roll [degrees, positive numbers correspond to right turn]
10	Aircraft pitch [degrees, positive numbers correspond to nose up]
11	Aircraft true heading, relative to Earth North [degrees, positive numbers = east, negative numbers = west]
12	Antenna incidence angle, antenna boresight in relation to nadir [degrees]
13	Antenna pointing angle, antenna boresight in relation to north [degrees, positive numbers = east, negative numbers = west]
14	Antenna rotation, antenna reference frame in relation to Earth reference frame [degrees]

8.3 Laser Scanner

Swath files

The filename of the laser scanner data contains the data level (LLL = L1b or L2) as well as start and stop time of the data file in UTC.

```
Date      Start   Stop
ALS_LLL_YYYYMMDDTHHMMSS_HHMMSS
```

The laser scanner data is stored in big-endian binary format, containing a section for

- a) File header
- b) Time stamp of each scan line
- c) Data containing for each line (\times number of lines)
 - a. Timestamp
 - b. Latitude
 - c. Longitude
 - d. Elevation (L1B) | Freeboard (L2)
 - e. Amplitude
 - f. Reflectance

The data is organized in scan lines and number of shots per scan line. The number of scan lines and data points per line is stored in the header.

Table 15: Description of ALS file header information

Field	Description	Unit	Size (Bytes)	Type
1	Header size	Byte	2	Byte
2	Nr of scan lines (Nsl)		4	Unsigned int32
3	Nr of shots per scan (Ns)		2	Unsigned int16
4	Bytes per scan line	Byte	2	Unsigned int16
5	Bytes timestamp information	Byte	8	Unsigned int64
6	Year (Start Time)		2	Unsigned int16
7	Month (Start Time)		1	Byte
8	Day (Start Time)		1	Byte
9	Start Time	Seconds of day	4	Unsigned int32
10	Stop Time	Seconds of day	5	Unsigned int32
11	Device Name (Scanner ID)		8	Char*8

The header is followed by the time stamp information of each side-ward scan line. This information is given as a convenience to select subsections of the data, without the need to read the entire data file first

Table 16: Description of ALS file timestamp information

Fields	Description	Unit	Size (Bytes)	Type
Nsl	Timestamp	Seconds of day	$2 \times Nsl$	Unsigned int16

Last part of the ALS file is the data section. The data structure is stored for each scan and the scan records are repeated for the number of line scans.

Table 17: Description of ALS file data record (for each scan, repeated by number of scans)

Fields	Description	Unit	Size (Bytes)	Type
Ns	Timestamp	Seconds of day	$8 \times Ns$	Float64
Ns	Latitude	Degree	$8 \times Ns$	Float64
Ns	Longitude	Degree	$8 \times Ns$	Float64
Ns	Elevation Freeboard	Meter	$8 \times Ns$	Float64
Ns	Amplitude		$8 \times Ns$	Float64
Ns	Reflectance		$8 \times Ns$	Float64

Software

Software routines in python for parsing, gridding and plotting ALS data are available on github: <https://github.com/shendric/pyals>

Resampled data

The temporally resampled laser scanner freeboard is stored in a standard ASCII file, containing the time stamp, the number of averaged samples, the geographical position as

well as mean freeboard with standard deviation. As quick view plot of the resampled and center beam data is also given in the folder of the ALS level-3 data products.

Table 18 : Content of resampled ALS freeboard files

Column	Description	Type
1	Timestamp	UTC time string YYYY-MM-DDTHH:MM:SS.SSS
2	Number of Samples	
3	Longitude	Decimal degrees
4	Latitude	Decimal degrees
5	Freeboard	Meter
6	Freeboard Std. Dev.	Meter

8.4 KT19

The KT19 data is delivered in standard netCDF (Version 4) binary data format. The data files are self-descriptive and can be read with netCDF libraries available for all major programming languages and software tools.

More information: <http://www.unidata.ucar.edu/software/netcdf/>

The KT19 netcdf files contain the following datasets:

Timestamp	Seconds since Jan 01, 1970 00:00 UTC
Surface Temperature	Degree Celsius

8.5 Radiometer

The radiometer data is delivered in standard netCDF (Version 4) binary data format. The data files are self-descriptive and can be read with netCDF libraries available for all major programming languages and software tools.

More information: <http://www.unidata.ucar.edu/software/netcdf/>

The radiometer netcdf files contain the following datasets:

Timestamp	Seconds since Jan 01, 1970 00:00 UTC
Downwelling Radiation	W/m ²
Upwelling Radiation	W/m ²
Downwelling Radiation	W/m ²
20 sec moving average	
Upwelling Radiation	W/m ²
20 sec moving average	

8.6 EM-Bird

The EM-Bird data is delivered in tabulator separated ASCII columnar files with one file for each profile.

Table 19 : Description of EM-Bird data files

Column	Description	Unit
1	Year	
2	Month	
3	Day	
4	Second of the day	
5	Record number	
6	Latitude	Decimal degree
7	Longitude	Decimal degree
8	Distance	Meter
9	Total Thickness	Meter
10	Laser Range	Meter

8.7 Aerial Nadir Images

The nadir images are available as Canon raw format (*.raw) and converted jpeg files. The jpeg files are corrected for image distortion and vignetting caused by the lens. In addition a minor contrast enhancement filter was applied.

Timestamp and geographical location of the image is given in the EXIF tag. An example is given below

Please note that the timestamp of the image is only given as integer seconds due to limitation of the camera body.

GPS information:	
GPSVersionID	2.2.0.0
GPSLatitudeRef	N
GPSLatitude	78 10.36 0 (78.172667)
GPSLongitudeRef	E
GPSLongitude	19 39.66 0 (19.661000)
GPSAltitudeRef	Sea level
GPSAltitude	286.80 m
GPSTimeStamp	15 19 40.00
GPSImgDirectionRef	True direction
GPSImgDirection	0.00/0.00
GPSDateStamp	2014:03:26

9 EMIRAD Instrument validation flights

Table 20 shows the flight legs for the validation flight, carried out from Bremerhaven (BRV) February 19, 2014.

Table 20: Instrument validation flight, Bremerhaven, EMIRAD-2 data.

Date	Time (UTC)	Route	Special circumstances	Notes
20140219	15:25-15:53	BRV-Ocean	Transit	
20140219	15:55-15:59	Ocean nose and wing wags	Instrument validation manoeuvres	
20140219	16:00-16:38	Ocean-BRV	VNA measurements of antenna parameters	

Figure 46 provides an overview of the Bremerhaven validation flight. Yellow sections are transits, while the red section illustrates the wing wags and nose wags, used for EMIRAD-2 validation.

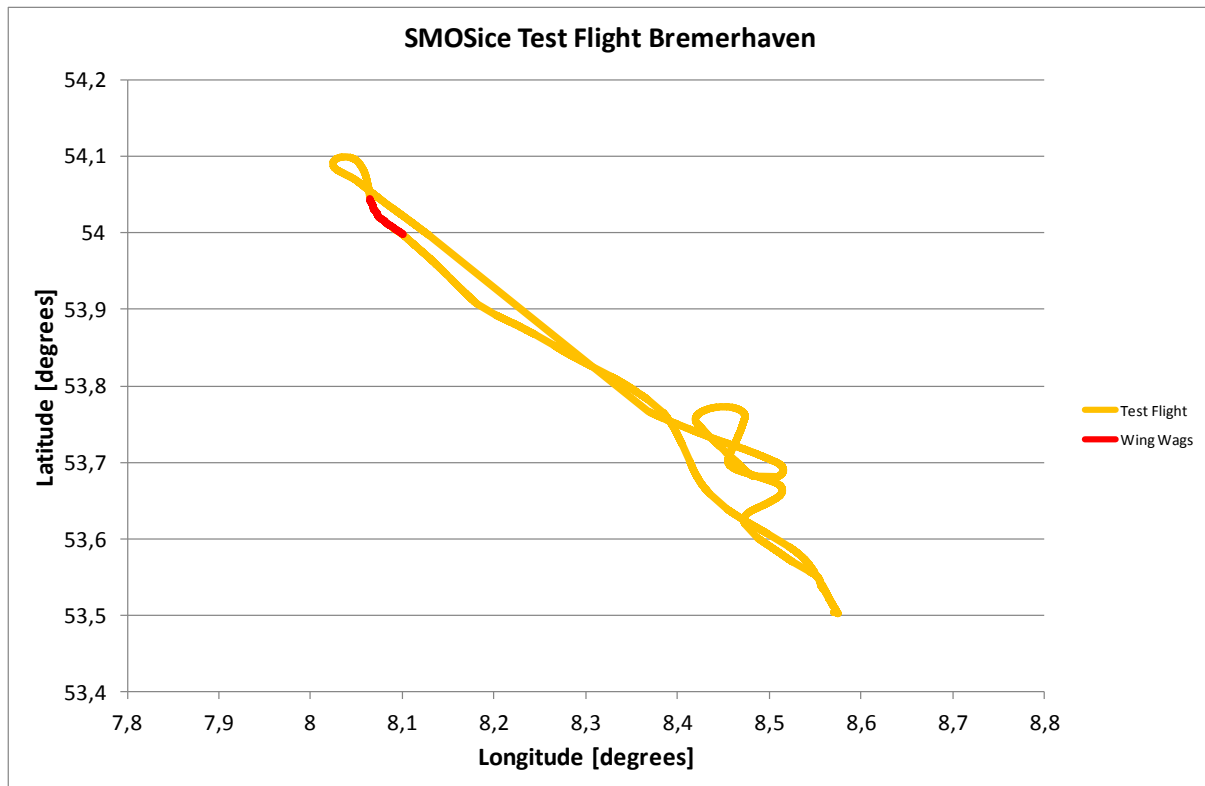


Figure 46: Bremerhaven validation flight (EMIRAD-2 over opean ocean).

9.1 Instrument validation flight, Svalbard

Table 21 shows the flight legs for the validation flight, carried out from Longyearbyen (LYR) March 23, 2014.

Table 21: Instrument validation flight, Longyearbyen, EMIRAD-2 data

Date	Time (UTC)	Route	Special circumstances	Notes
20140323	12:27-12:46	LYR-Ocean	Transit	a)
20140323	12:48-12:53	Ocean nose and wing wags	Instrument validation manoeuvres	a)
20140323	12:55-14:20	Ocean-LYR	Transit, including other on-board instruments	a)

Table notes:

- a) RFI detected in nadir horn, horizontal channel.
- b) RFI source identified and switched off.

Svalbard validation flight (EMIRAD-2 over open ocean) provides an overview of the Svalbard validation flight. Yellow sections are transits, while the red section illustrates the wing wags and nose wags, used for EMIRAD-2 validation. The periods without data before and after the red section are long calibration events, introduced in order to guarantee high accuracy for the instrument validation manoeuvres.

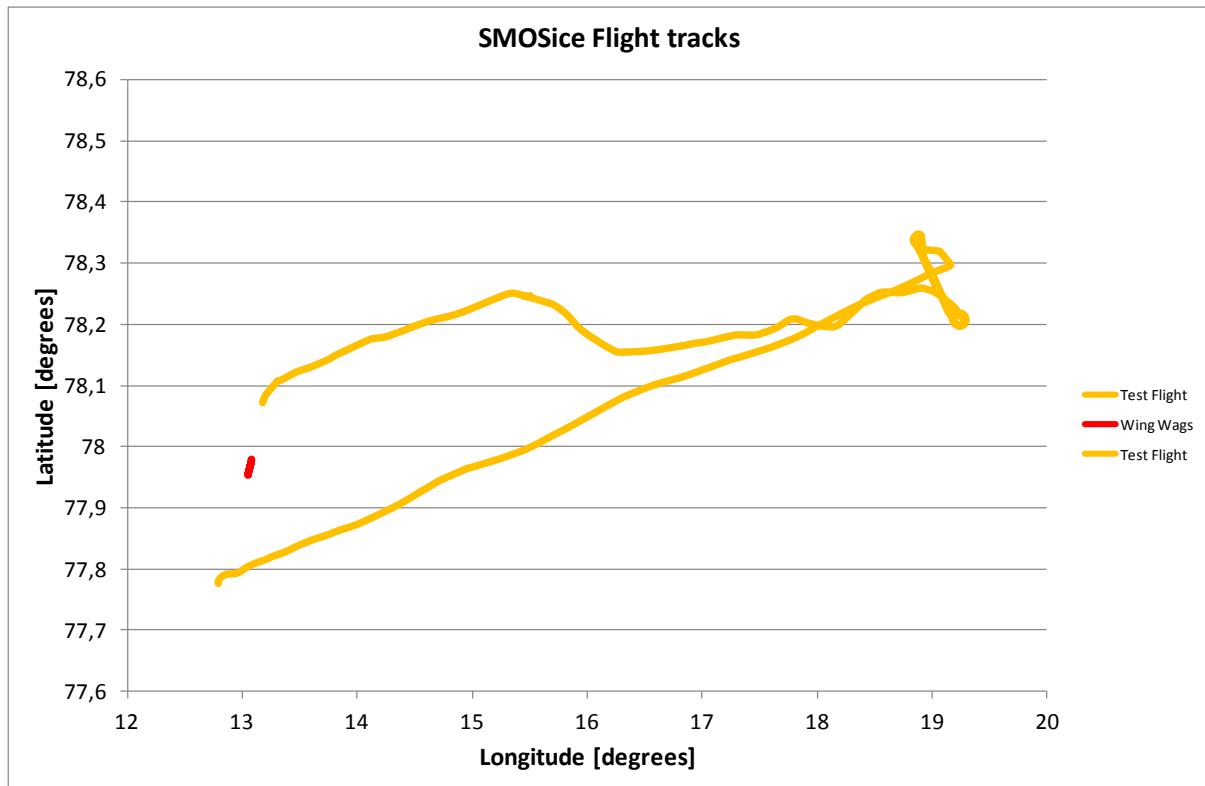


Figure 47: Svalbard validation flight (EMIRAD-2 over open ocean)

9.2 Navigation data

EMIRAD-2 navigation data recorded from all flights provides a list of the navigation data recorded during all flights. Navigation data include UTC time stamp, position latitude/longitude, altitude, and attitude. Attitude parameters for the Honeywell H-764 unit are guaranteed to an accuracy of 0.05 degrees, and information for aircraft roll, pitch, and true heading is stored in the data set.

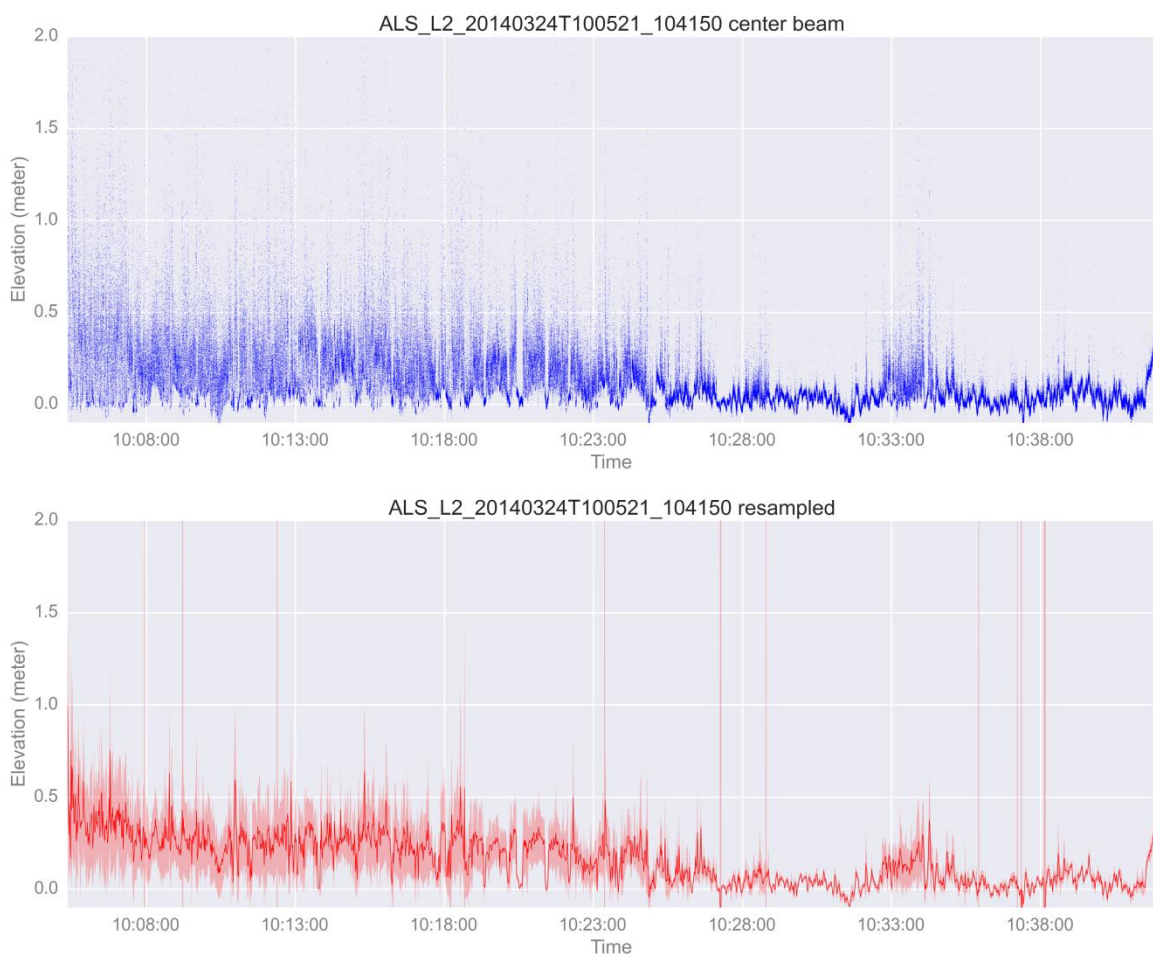
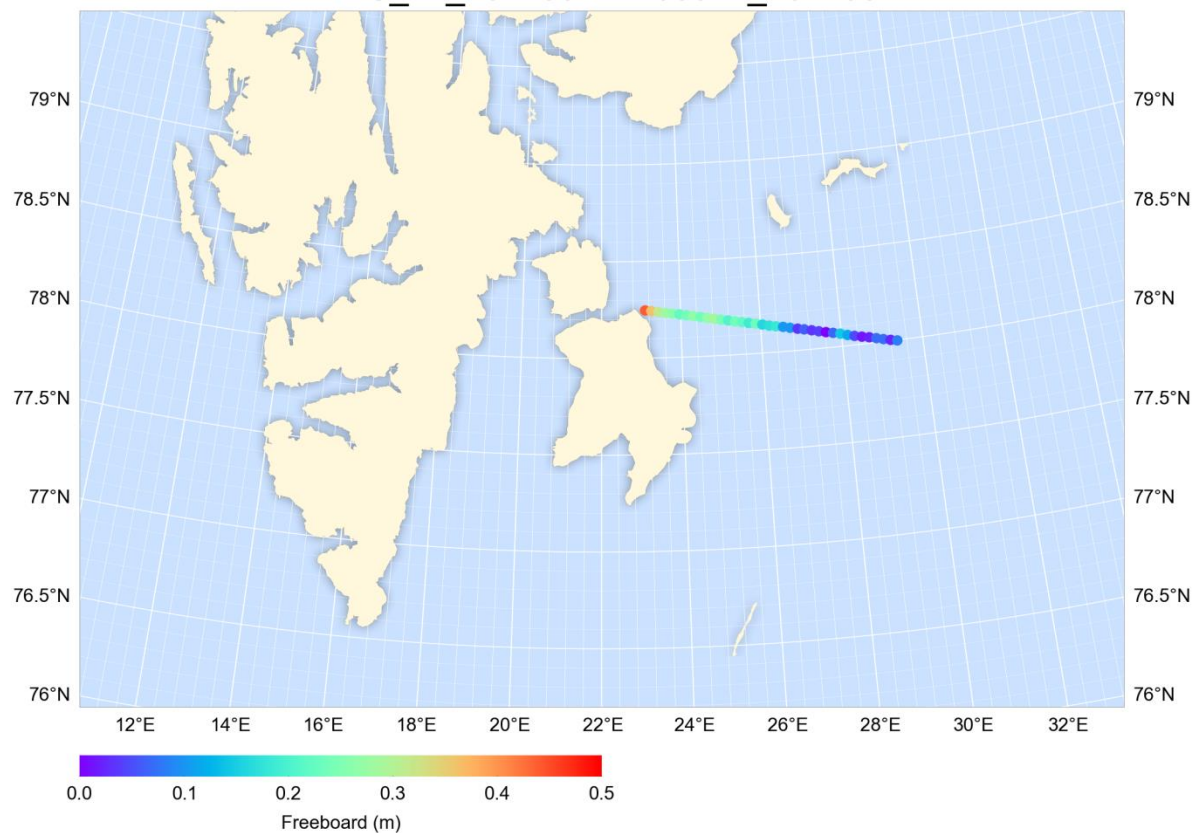
Table 22: EMIRAD-2 navigation data recorded from all flights.

Date	When (UTC)	Route	Special circumstances	Notes
20140323	12:27-12:46	LYR-Ocean		
20140323	12:48-12:53	Ocean nose and wing wags		
20140323	12:55-14:20	Ocean-LYR		

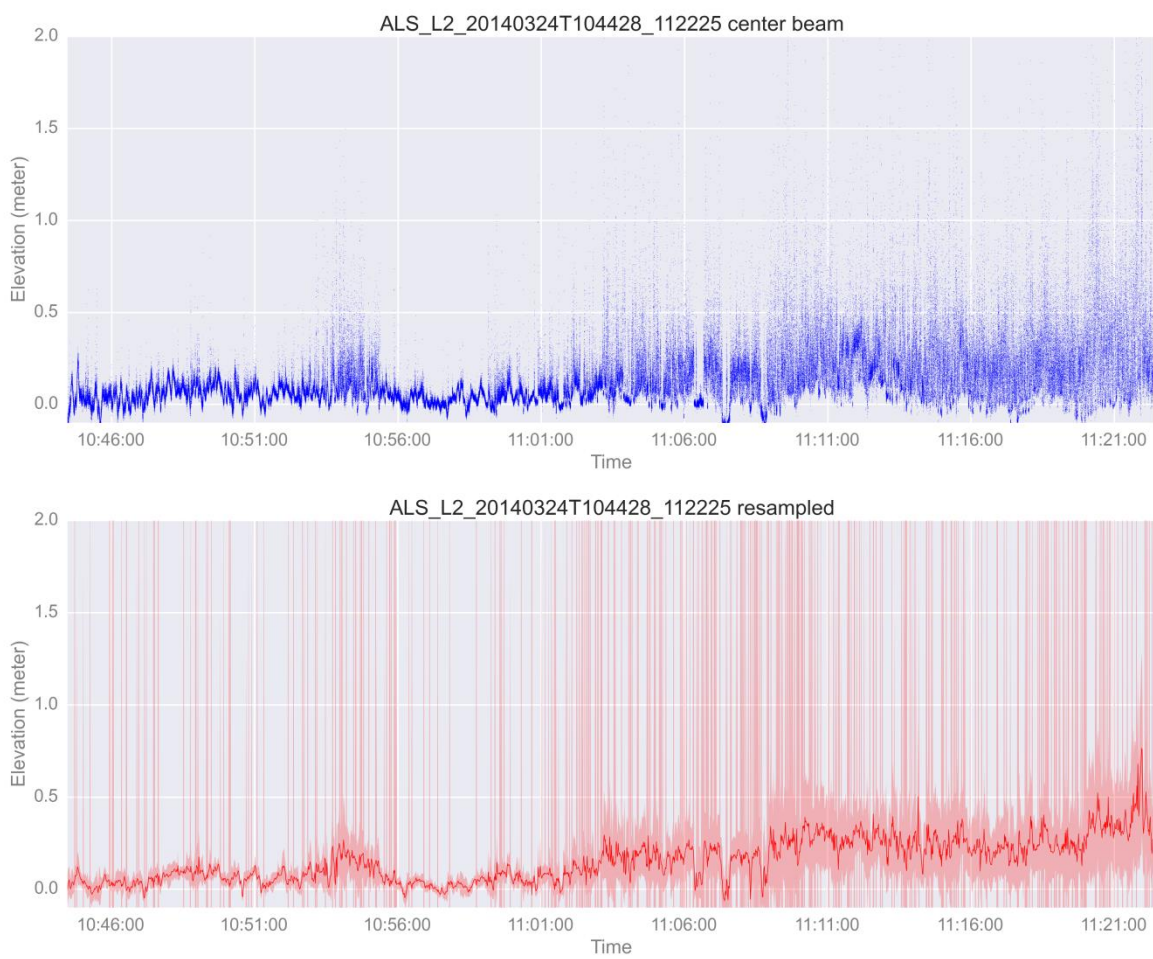
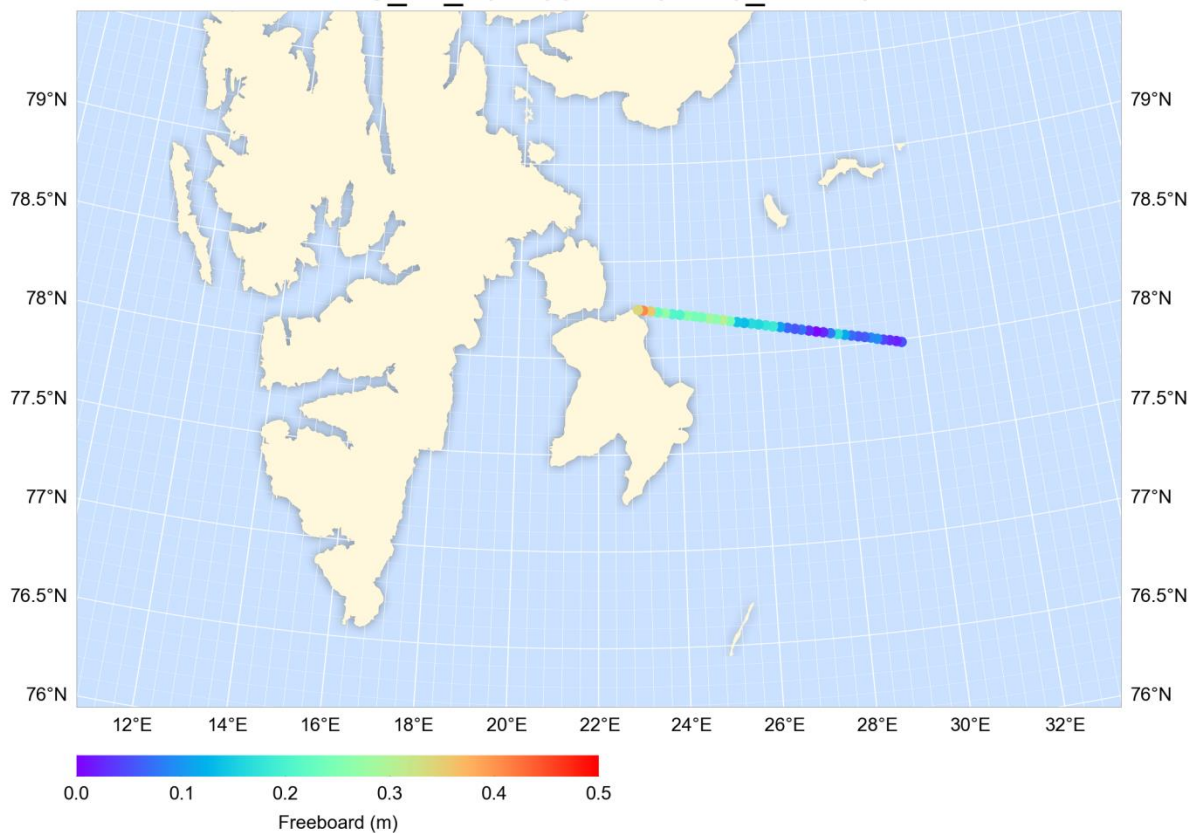
10 ALS Freeboard Profiles

This section contains overview maps and plots of the freeboard profiles of the airborne laserscanner with location and track plots of the resampled and center beam data.

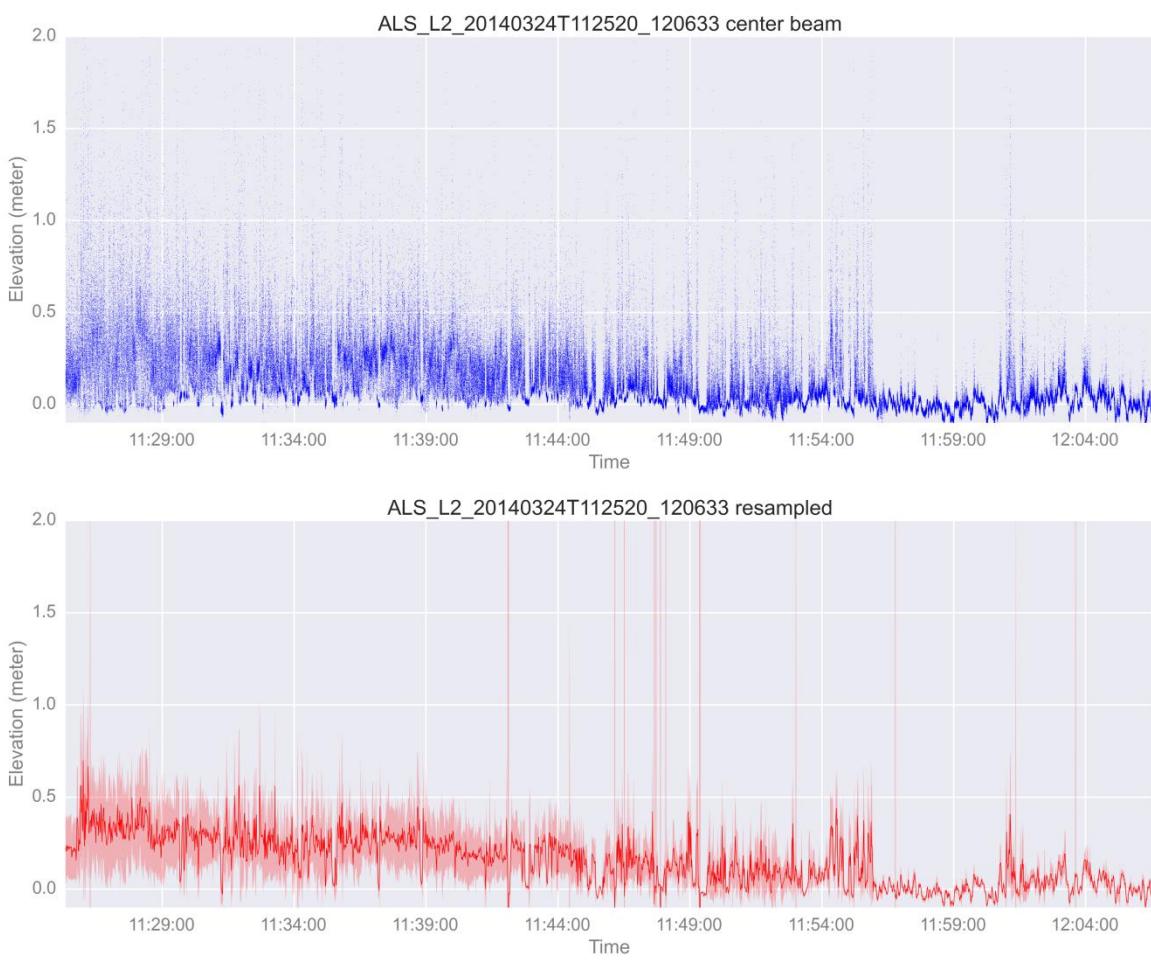
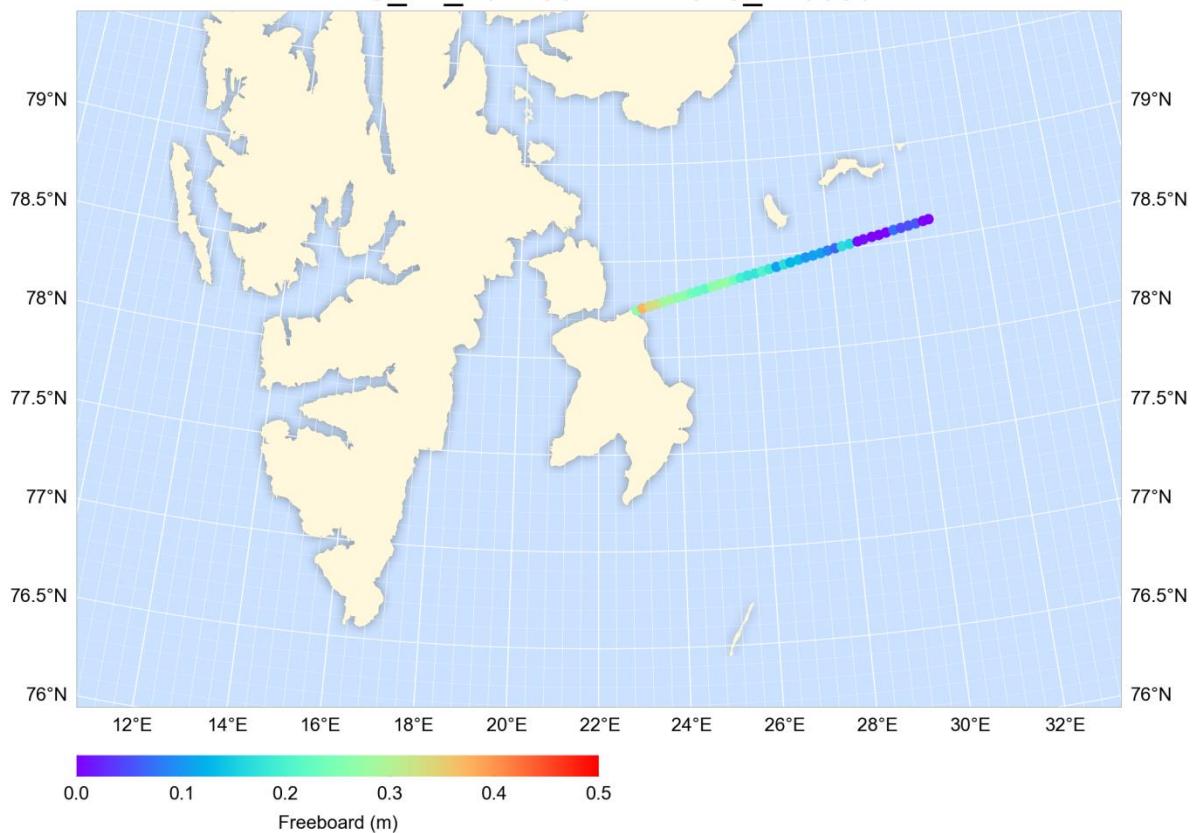
ALS_L2_20140324T100521_104150

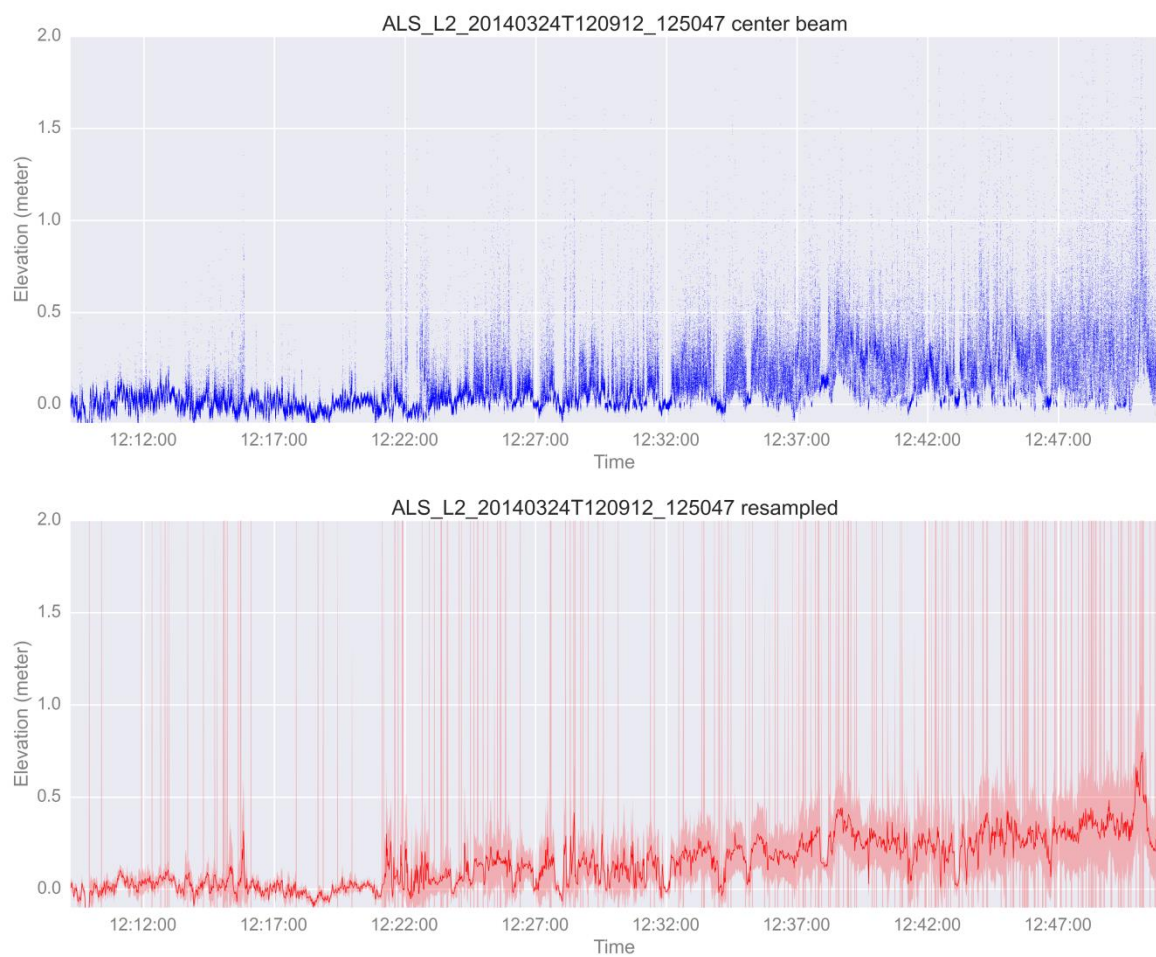
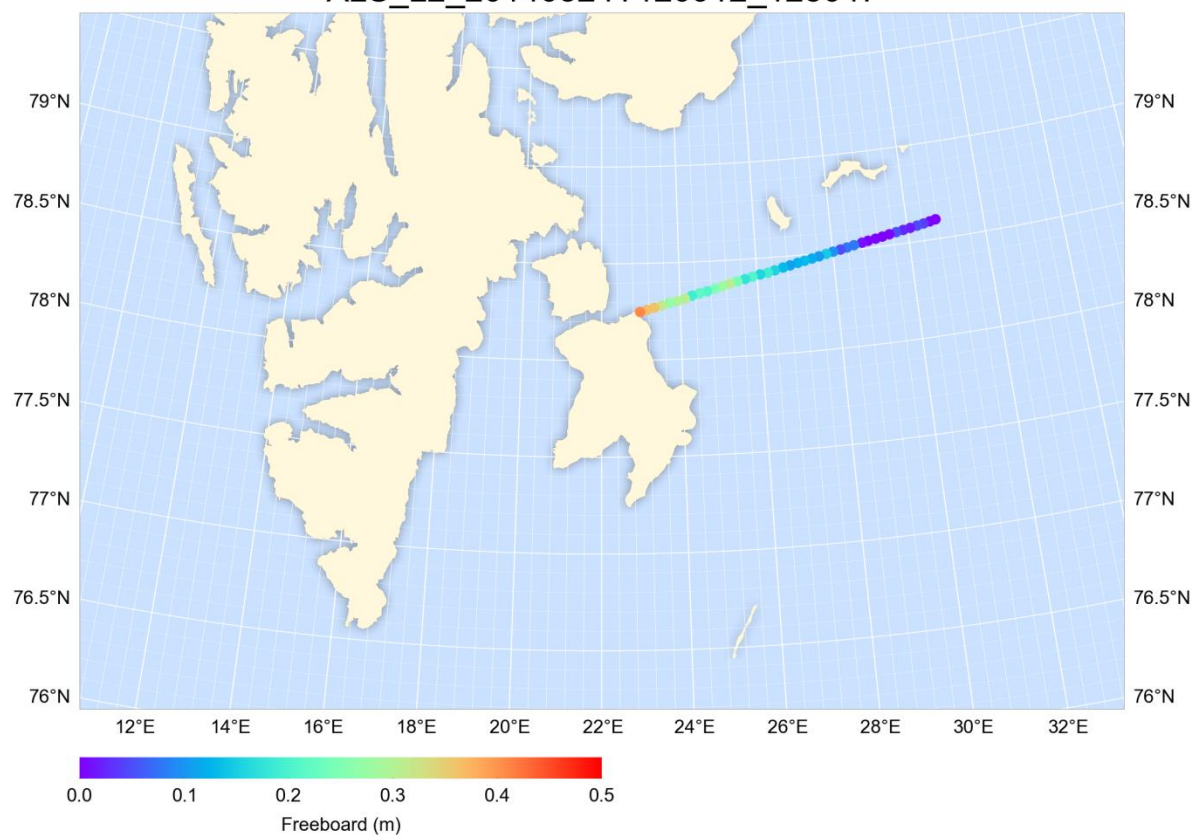


ALS_L2_20140324T104428_112225

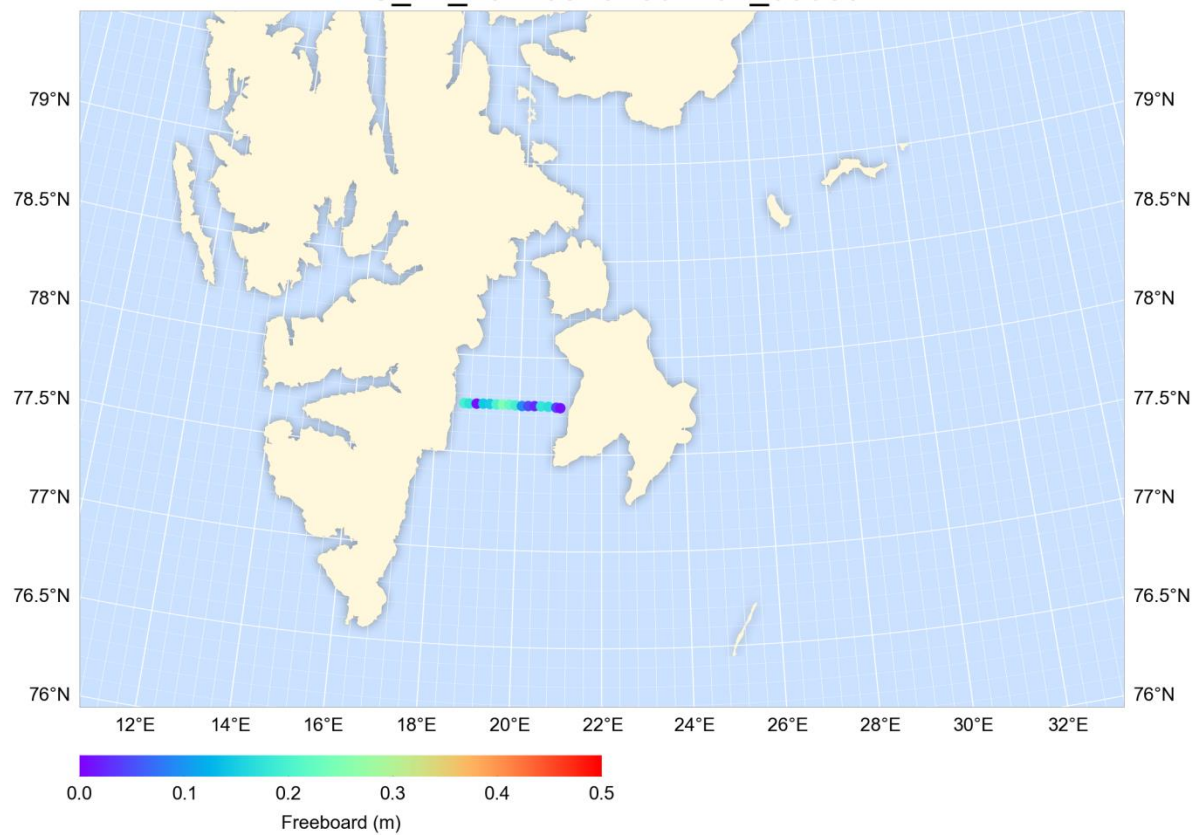


ALS_L2_20140324T112520_120633

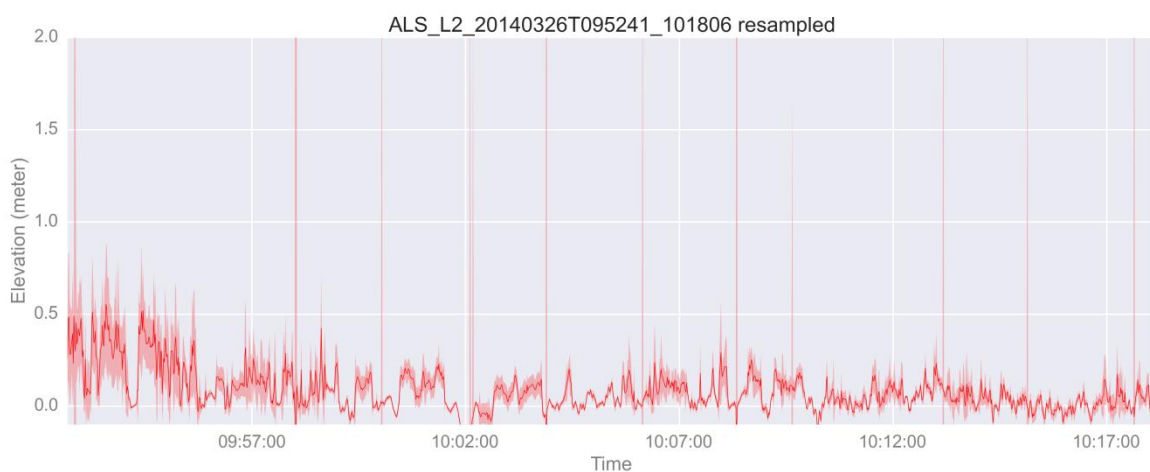
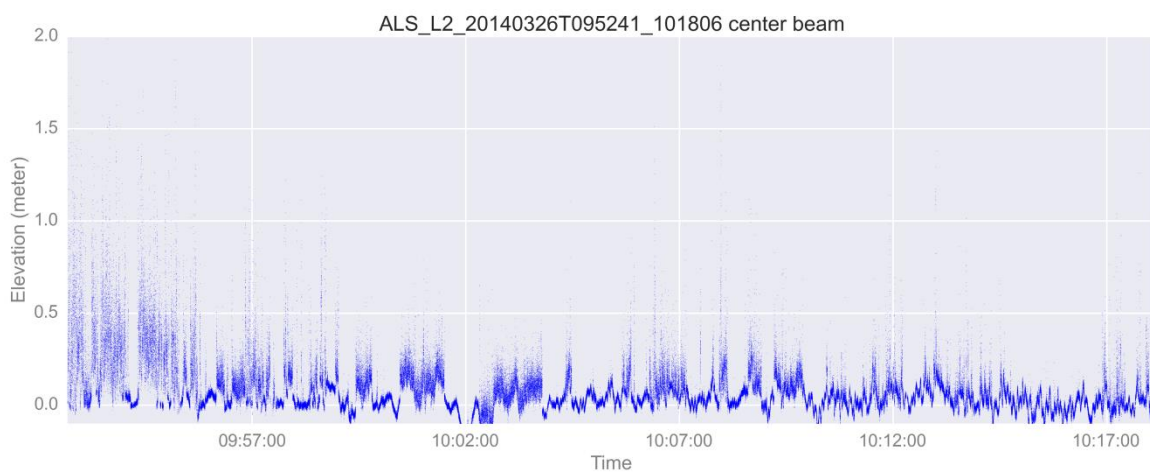
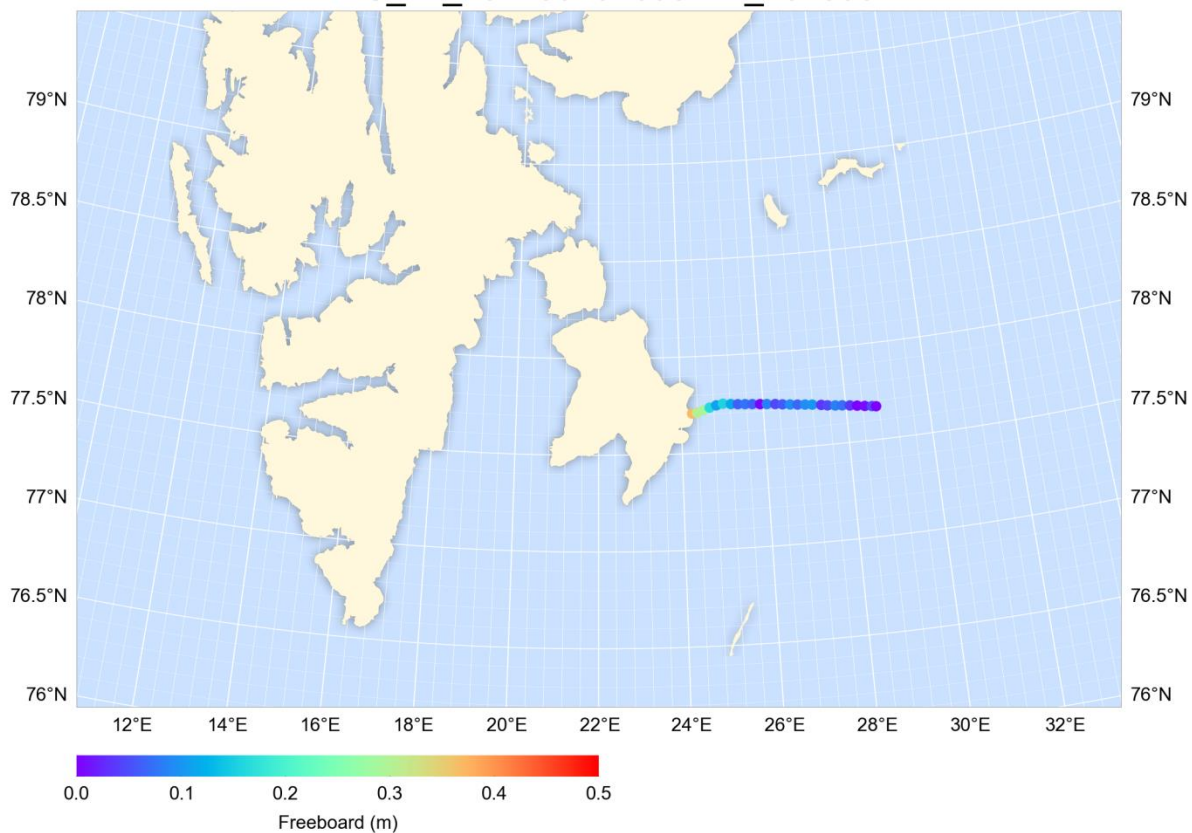


ALS_L2_20140324T120912_125047


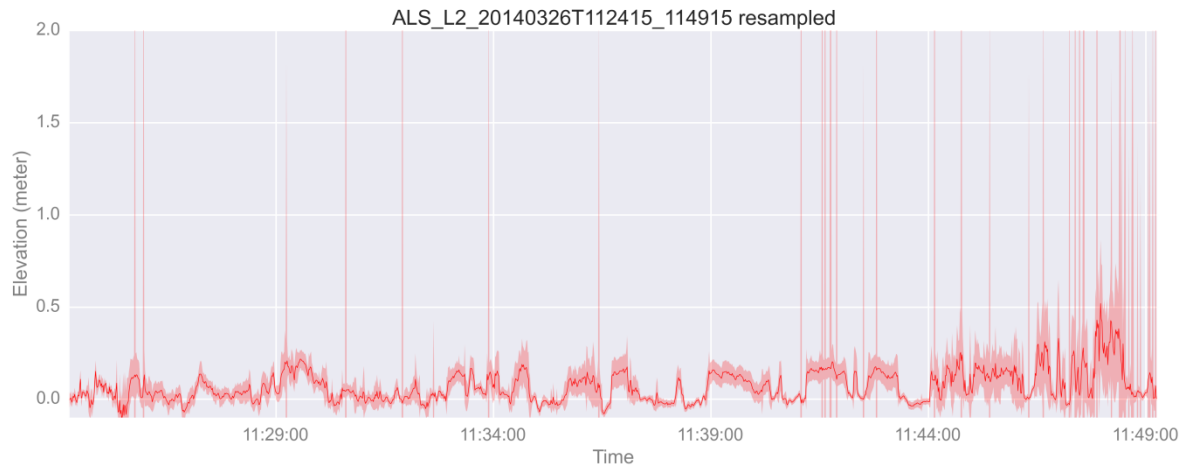
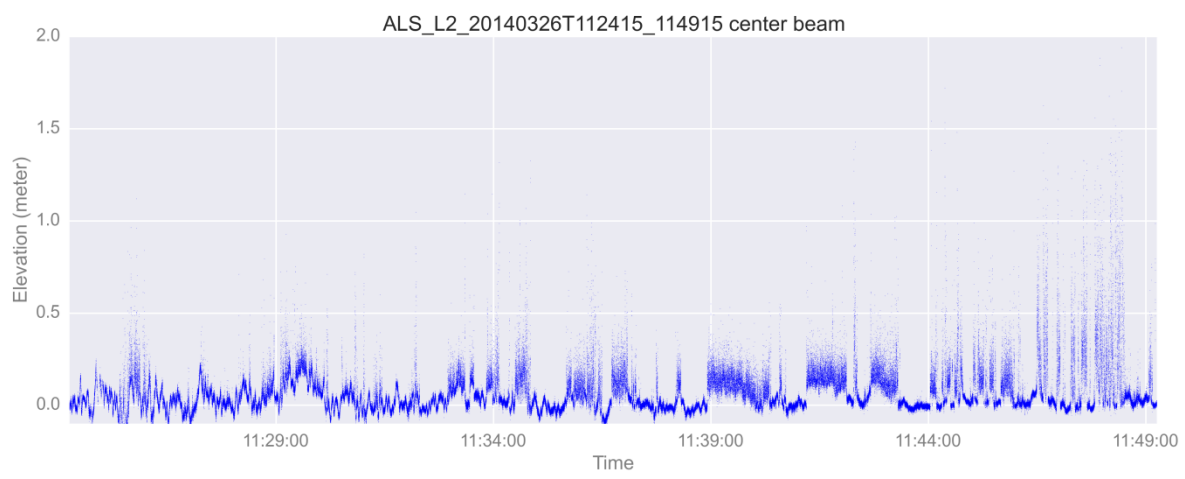
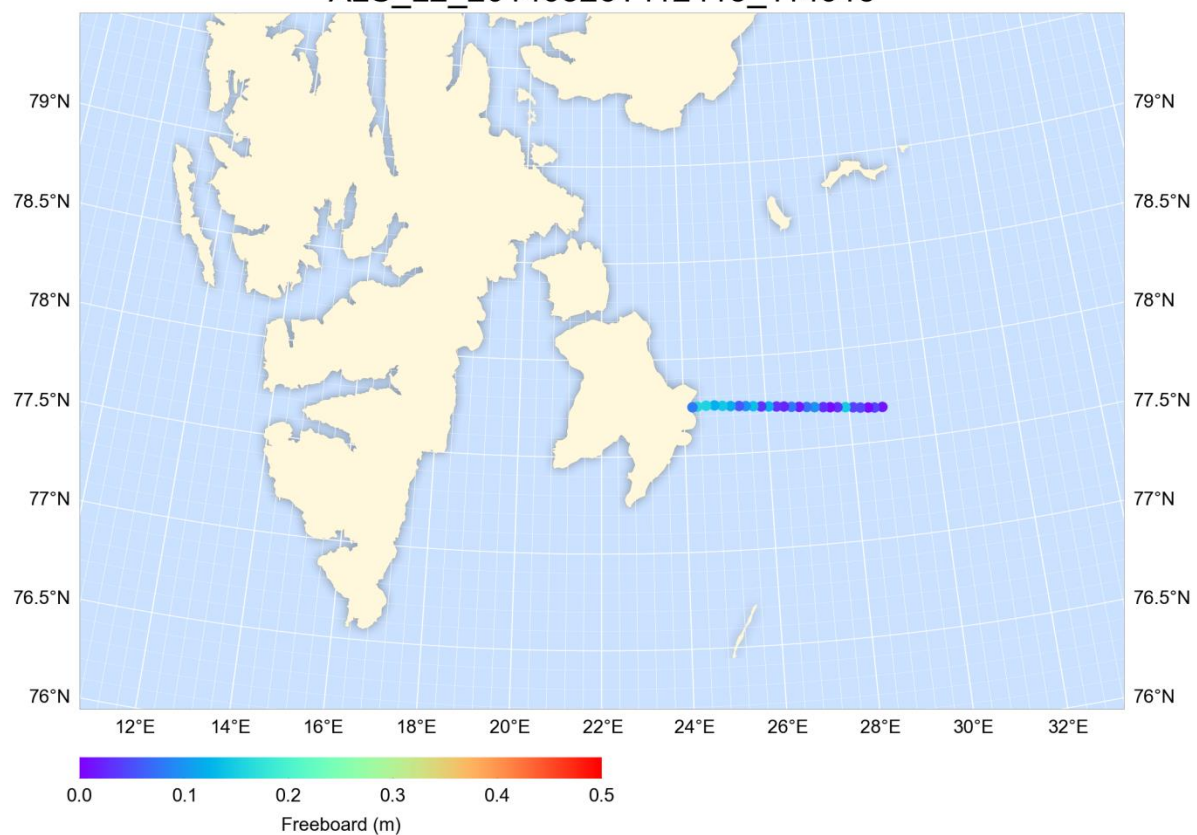
ALS_L2_20140326T092131_093601

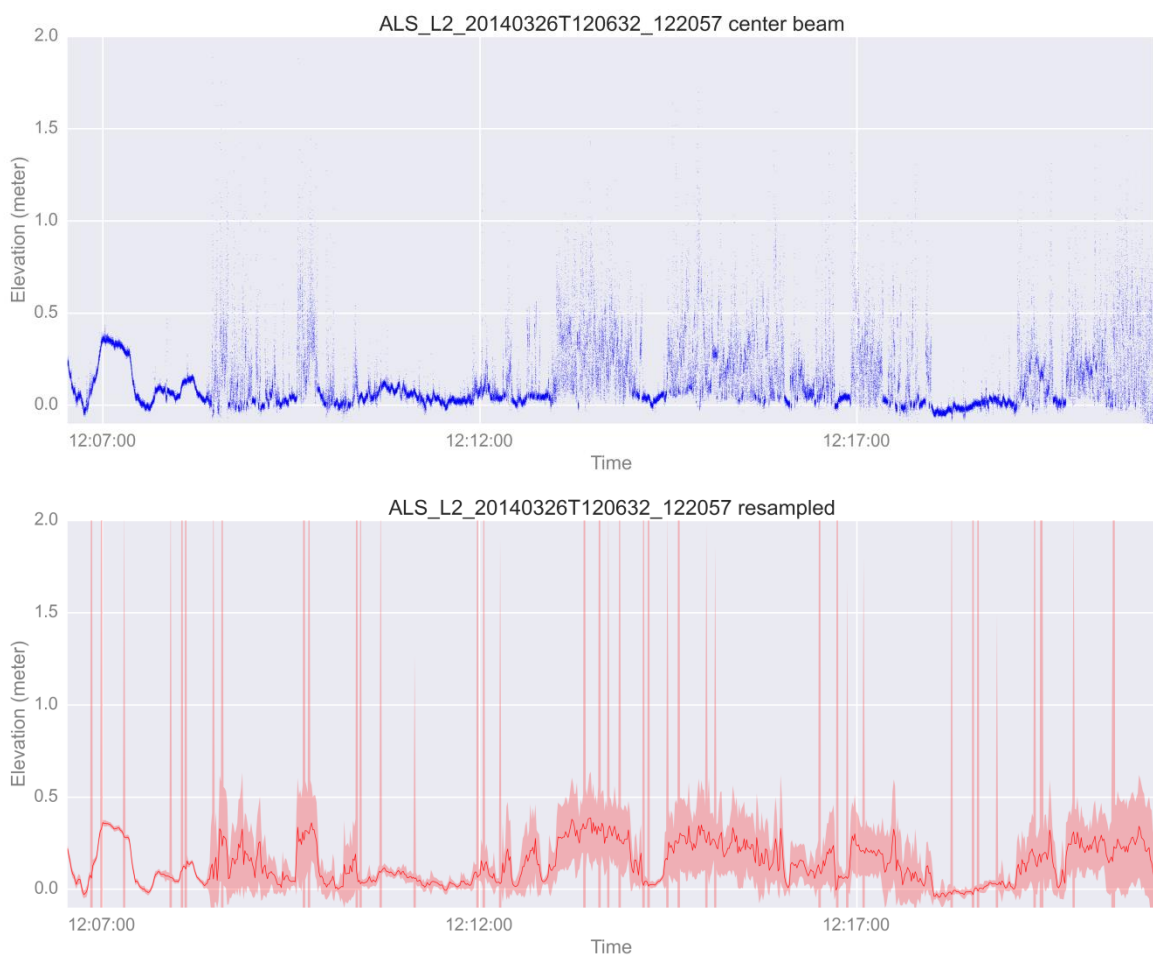
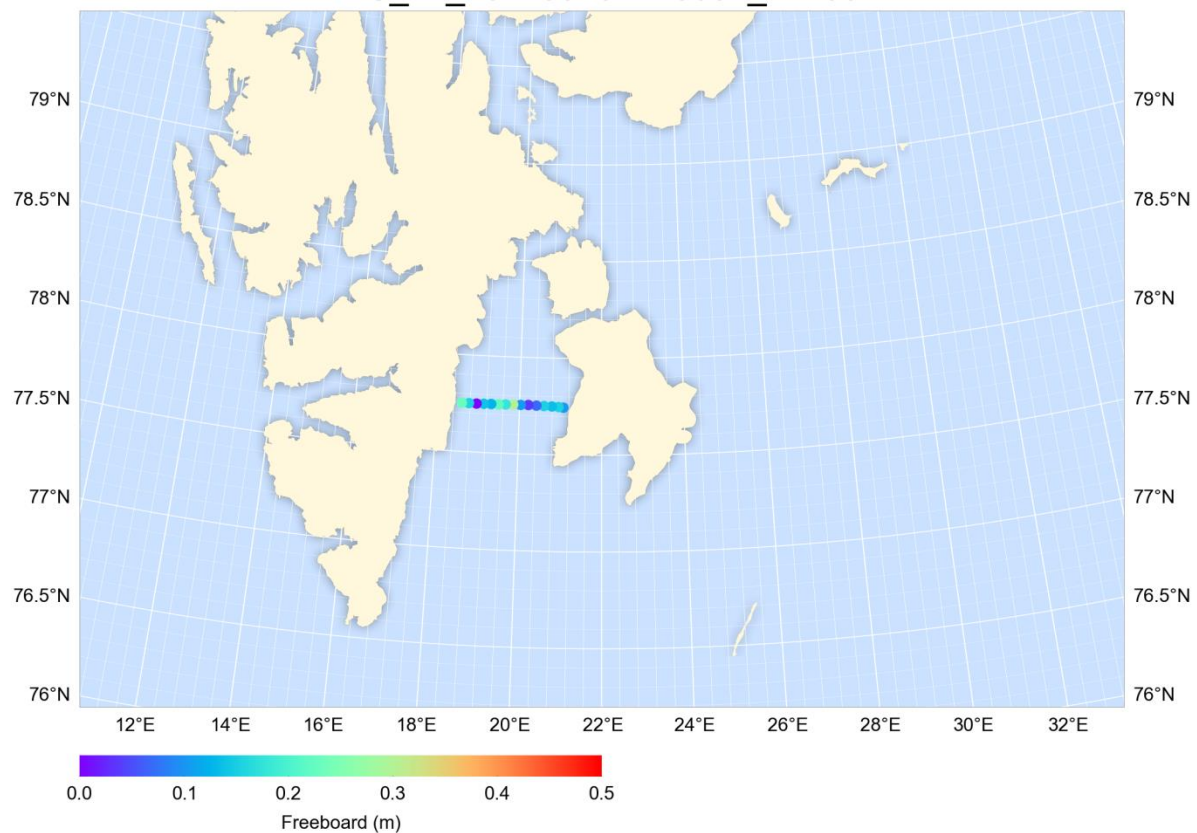


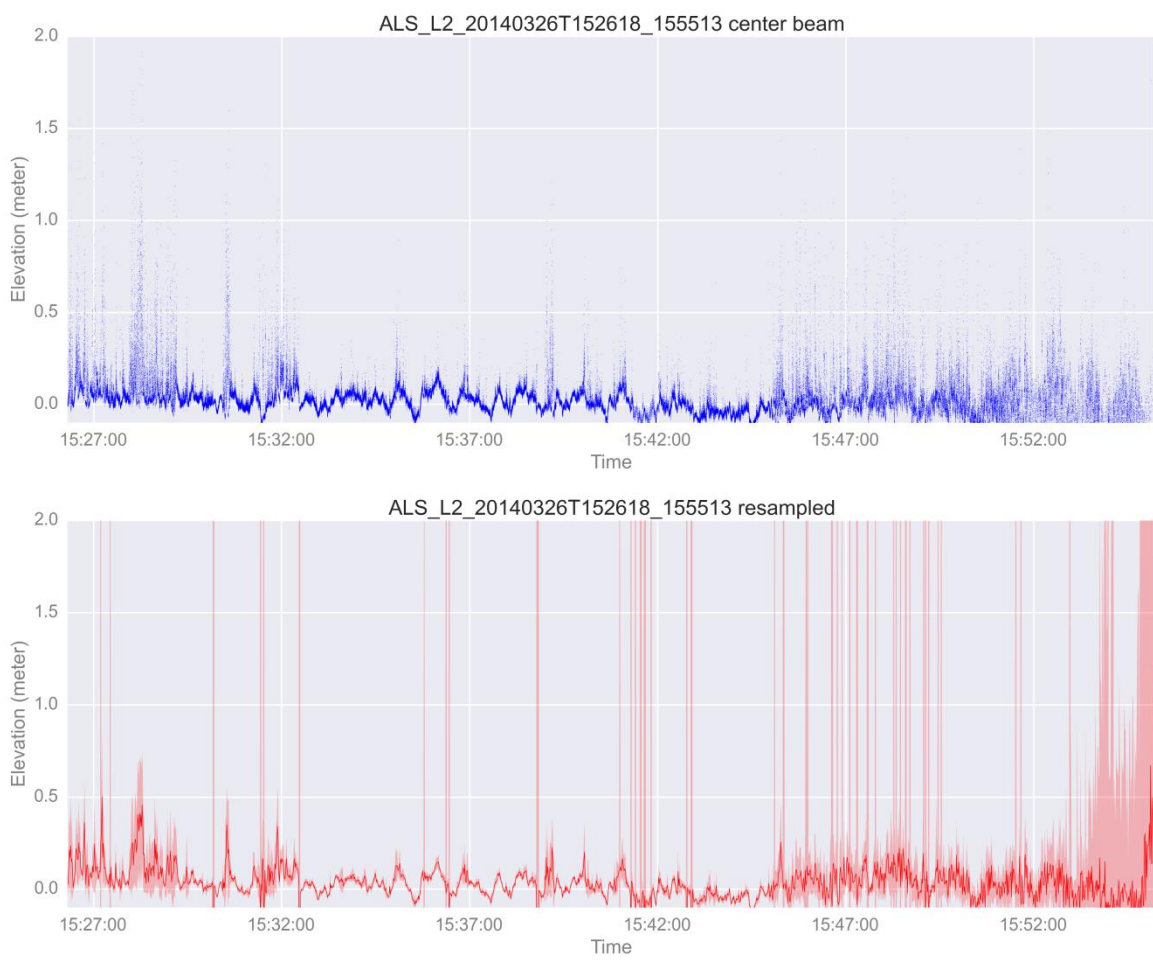
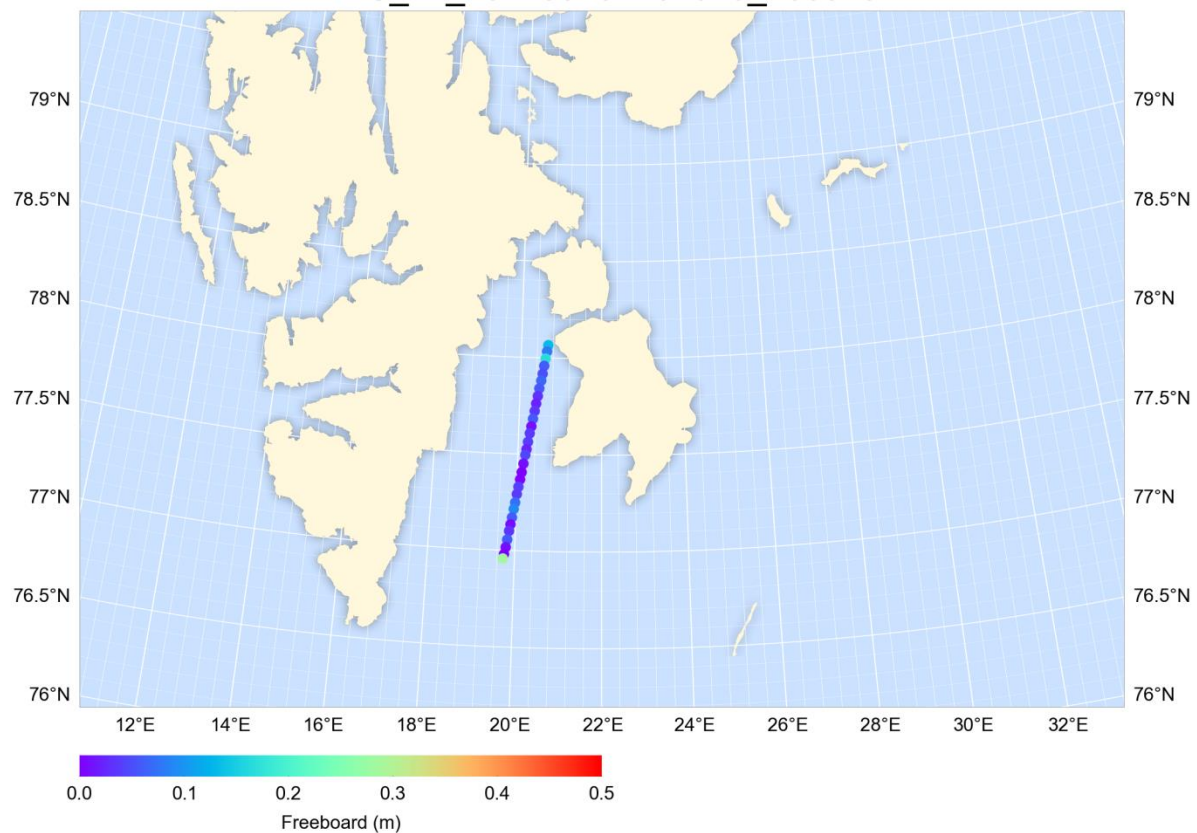
ALS_L2_20140326T095241_101806



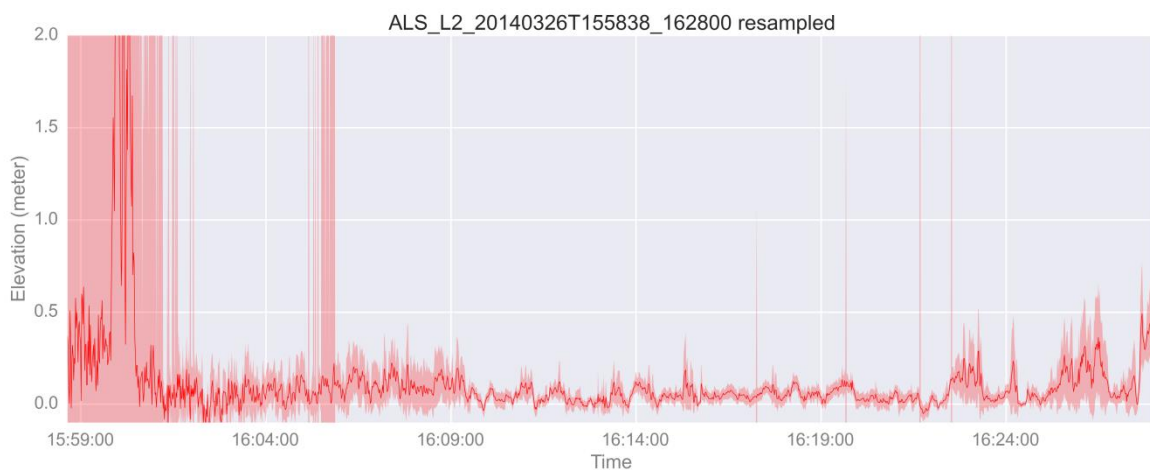
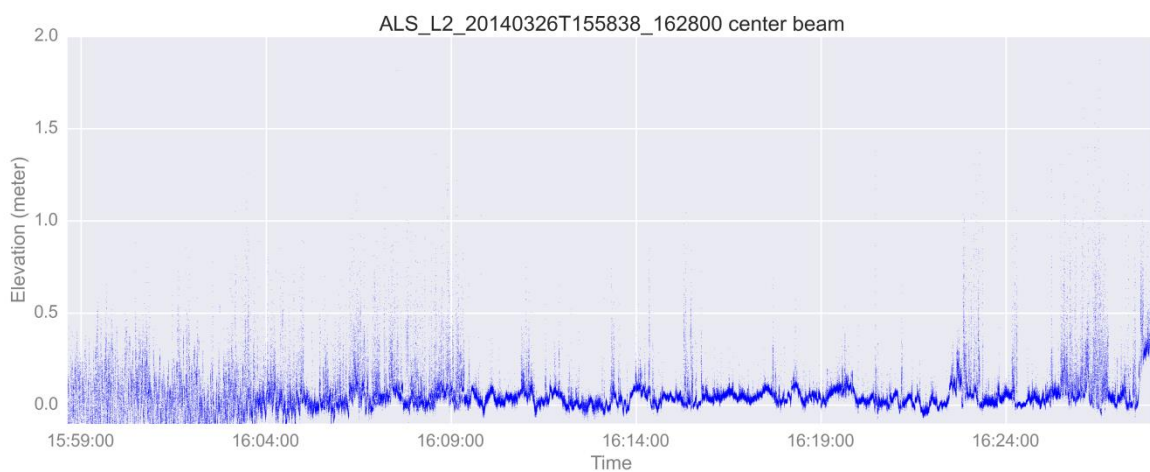
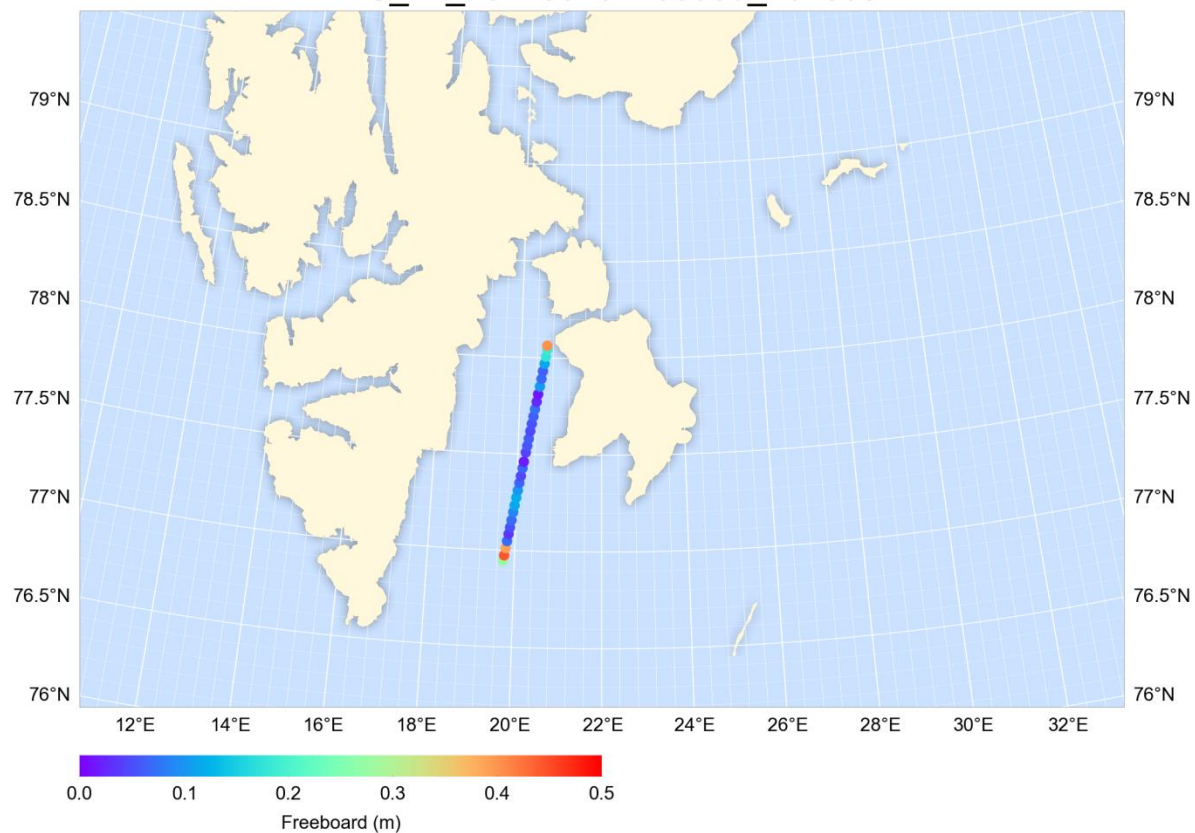
ALS_L2_20140326T112415_114915



ALS_L2_20140326T120632_122057


ALS_L2_20140326T152618_155513


ALS_L2_20140326T155838_162800



11 File Inventory

The following sections list all data files for each Polar-5 survey flight, their start and stop times and provide comments of the instrument operators.

11.1 Flight ID 20140323_01

EMIRAD	Start	Stop	Comment
08212260.e61	2014-03-23 12:37:55	2014-03-23 12:48:15	LYR-Ocean
08212260.e62	2014-03-23 12:27:56	2014-03-23 12:48:16	LYR-Ocean
08212480.e61	2014-03-23 12:50:38	2014-03-23 12:51:20	Ocean nose and wing wags
08212480.e62	2014-03-23 12:50:39	2014-03-23 12:51:21	Ocean nose and wing wags
08212550.e61	2014-03-23 12:56:54	2014-03-23 14:19:55	Ocean-LYR
08212550.e62	2014-03-23 12:56:55	2014-03-23 14:20:08	Ocean-LYR

ALS L1b	Start	Stop	Comment
ALS_L1B_20140323T132435_135136	2014-03-23 13:24:35	2014-03-23 13:51:36	

11.2 Flight ID 20140324_01

EMIRAD	Start	Stop	Comment
08309150.e61	2014-03-24 09:27:28	2014-03-24 12:52:56	Primary data set
08309150.e62	2014-03-24 09:15:42	2014-03-24 12:52:57	Primary data set
08312510.e61	2014-03-24 12:51:46	2014-03-24 12:52:56	Wing wags over ice
08312510.e62	2014-03-24 12:51:27	2014-03-24 12:52:57	Wing wags over ice
08312590.e61	2014-03-24 13:01:14	2014-03-24 13:10:46	Transit
08312590.e62	2014-03-24 13:00:17	2014-03-24 13:37:19	Transit
ALS	Start	Stop	Comment
ALS_L1B_20140324T095739_100301	2014-03-24 09:57:39	2014-03-24 10:03:01	
ALS_L1B_20140324T100300_100523	2014-03-24 10:03:00	2014-03-24 10:05:23	
ALS_L1B_20140324T100521_104150	2014-03-24 10:05:21	2014-03-24 10:41:50	
ALS_L1B_20140324T104148_104429	2014-03-24 10:41:48	2014-03-24 10:44:29	
ALS_L1B_20140324T104428_112225	2014-03-24 10:44:28	2014-03-24 11:22:25	
ALS_L1B_20140324T112223_120647	2014-03-24 11:22:23	2014-03-24 12:06:47	
ALS_L1B_20140324T112520_120633	2014-03-24 11:25:20	2014-03-24 12:06:33	
ALS_L1B_20140324T120645_120913	2014-03-24 12:06:45	2014-03-24 12:09:13	
ALS_L1B_20140324T120912_125047	2014-03-24 12:09:12	2014-03-24 12:50:47	
ALS L2	Start	Stop	Comment
ALS_L2_20140324T100521_104150	2014-03-24 10:05:21	2014-03-24 10:41:50	
ALS_L2_20140324T104428_112225	2014-03-24 10:44:28	2014-03-24 11:22:25	
ALS_L2_20140324T112520_120633	2014-03-24 11:25:20	2014-03-24 12:06:33	
ALS_L2_20140324T120912_125047	2014-03-24 12:09:12	2014-03-24 12:50:48	
ALS L2 resampled	Start	Stop	Comment
ALS_L2_20140324T100521_104150_resampled.dat	2014-03-24 10:05:21	2014-03-24 10:41:50	
ALS_L2_20140324T104428_112225_resampled.dat	2014-03-24 10:44:28	2014-03-24 11:22:25	
ALS_L2_20140324T112520_120633_resampled.dat	2014-03-24 11:25:20	2014-03-24 12:06:33	
ALS_L2_20140324T120912_125047_resampled.dat	2014-03-24 12:09:12	2014-03-24 12:50:47	
KT19	Start	Stop	Comment
2014032402_KT19_surface-temperature.nc	2014-03-24 10:05:00	2014-03-24 12:52:59	
Pyrgrometer	Start	Stop	Comment
2014032402_pyrgrometer_longwave-irradiance.nc	2014-03-24 10:05:00	2014-03-24 12:52:59	

11.3 Flight ID 20140326_01

EMIRAD	Start	Stop	Comment
08508460.e61	2014-03-26 09:01:24	2014-03-26 12:22:58	Primary data set
08508460.e62	2014-03-26 08:47:16	2014-03-26 12:22:58	Primary data set
08512260.e61	2014-03-26 12:27:49	2014-03-26 12:29:47	Transit
08512260.e62	2014-03-26 12:27:50	2014-03-26 13:01:05	Transit

ALS	Start	Stop	Comment
ALS_L1B_20140326T092131_093601	2014-03-26 09:21:31	2014-03-26 09:36:01	
ALS_L1B_20140326T095241_101806	2014-03-26 09:52:41	2014-03-26 10:18:06	
ALS_L1B_20140326T102117_104749	2014-03-26 10:21:17	2014-03-26 10:47:49	
ALS_L1B_20140326T105129_112151	2014-03-26 10:51:29	2014-03-26 11:21:51	
ALS_L1B_20140326T112415_115116	2014-03-26 11:24:15	2014-03-26 11:51:16	
ALS_L1B_20140326T120632_122057	2014-03-26 12:06:32	2014-03-26 12:20:57	
ALS_L1B_20140326T123840_124038	2014-03-26 12:38:40	2014-03-26 12:40:38	Runway Calibration
ALS_L1B_20140326T124037_124207	2014-03-26 12:40:37	2014-03-26 12:42:07	Runway Calibration
ALS_L1B_20140326T124205_124452	2014-03-26 12:42:05	2014-03-26 12:44:52	Runway Calibration
ALS_L1B_20140326T124451_124716	2014-03-26 12:44:51	2014-03-26 12:47:16	Runway Calibration
ALS_L1B_20140326T124715_124834	2014-03-26 12:47:15	2014-03-26 12:48:34	Runway Calibration

ALS L2	Start	Stop	Comment
ALS_L2_20140326T092131_093601	2014-03-26 09:21:31	2014-03-26 09:36:01	
ALS_L2_20140326T095241_101806	2014-03-26 09:52:41	2014-03-26 10:18:07	
ALS_L2_20140326T112415_114915	2014-03-26 11:24:15	2014-03-26 11:49:15	
ALS_L2_20140326T120632_122057	2014-03-26 12:06:32	2014-03-26 12:20:57	

ALS L2 resampled	Start	Stop	Comment
ALS_L2_20140326T092131_093601_resampled.dat	2014-03-26 09:21:31	2014-03-26 09:36:01	
ALS_L2_20140326T095241_101806_resampled.dat	2014-03-26 09:52:41	2014-03-26 10:18:06	
ALS_L2_20140326T112415_114915_resampled.dat	2014-03-26 11:24:15	2014-03-26 11:49:15	
ALS_L2_20140326T120632_122057_resampled.dat	2014-03-26 12:06:32	2014-03-26 12:20:57	

KT19	Start	Stop	Comment
2014032603_KT19_surface-temperature.nc	2014-03-26 09:22:00	2014-03-26 12:20:59	

Pyrgeometer	Start	Stop	Comment
2014032603_pyrgeometer_longwave-irradiance.nc	2014-03-26 09:22:00	2014-03-26 12:20:59	

11.4 Flight ID 20140326_02

EMIRAD	Start	Stop	Comment
08514260.e61	2014-03-26 14:38:12	2014-03-26 16:27:08	Primary data set
08514260.e62	2014-03-26 14:27:56	2014-03-26 16:27:07	Primary data set
08516280.e61	2014-03-26 16:28:42	2014-03-26 16:29:46	Wing wags over ice
08516280.e62	2014-03-26 16:28:41	2014-03-26 16:29:46	Wing wags over ice
08516320.e61	2014-03-26 16:33:03	2014-03-26 16:39:54	Transit
08516320.e62	2014-03-26 16:33:04	2014-03-26 16:59:57	Transit

ALS	Start	Stop	Comment
ALS_L1B_20140326T152618_155513	2014-03-26 15:26:18	2014-03-26 15:55:13	
ALS_L1B_20140326T155838_162800	2014-03-26 15:58:38	2014-03-26 16:28:00	

ALS L2	Start	Stop	Comment
ALS_L2_20140326T152618_155513	2014-03-26 15:26:18	2014-03-26 15:55:13	
ALS_L2_20140326T155838_162800	2014-03-26 15:58:38	2014-03-26 16:28:01	

ALS L2 resampled	Start	Stop	Comment
ALS_L2_20140326T152618_155513_resampled.dat	2014-03-26 15:26:18	2014-03-26 15:55:13	
ALS_L2_20140326T155838_162800_resampled.dat	2014-03-26 15:58:38	2014-03-26 16:28:00	

KT19	Start	Stop	Comment
2014032604_KT19_surface-temperature.nc	2014-03-26 15:27:00	2014-03-26 16:26:59	

Pyrgeometer	Start	Stop	Comment
2014032604_pyrgeometer_longwave-irradiance.nc	2014-03-26 15:27:00	2014-03-26 16:26:59	

This page is intentionally left blank